Discrete Mechanical Metamaterials

by

Benjamin Eric Jenett

B.A. Architecture, UC Berkeley (2007)
M.S. Civil Engineering, Massachusetts Institute of Technology (2015)

Submitted to the Program in Media Arts and Sciences
in partial fulfillment of the requirements for the degree of

Doctor of Philosophy

at the

MASSACHUSETTS INSTITUTE OF TECHNOLOGY

September 2020

Author . . . .
Program in Media Arts and Sciences
August 17, 2020

Certified by. . . . .
Neil Gershenfeld
Director, MIT Center for Bits and Atoms
Thesis Supervisor

Accepted by . . . .
Tod Machover
Academic Head,
Program in Media Arts and Sciences

Discrete Mechanical Metamaterials

by

Benjamin Eric Jenett

Submitted to the Program in Media Arts and Sciences
on August 17, 2020, in partial fulfillment of the
requirements for the degree of
Doctor of Philosophy

Abstract

Digital fabrication enables complex designs to be realized with improved speed, precision, and cost compared to manual techniques. Additive manufacturing, for example, is one of the leading methods for rapid prototyping and near net shape part production. Extension to full scale structures and systems, however, remains a challenge, as cost, speed and performance present orthogonal objectives that are inherently coupled to limited material options, stochastic process errors, and machine-based constraints. To address these issues, this thesis introduces new materials that physically embody attributes of digital systems, scalable methods for automating their assembly, and a portfolio of use cases with novel, full-scale structural and robotic platforms.

First, I build on the topic of discrete materials, which showed a finite set of modular parts can be incrementally and reversibly assembled into larger functional structures. I introduce a new range of attainable properties, such as rigidity, compliance, chirality, and auxetic behavior, all within a consistent manufacturing and assembly framework. These discretely assembled mechanical metamaterials show global continuum properties based on local cellular architectures, resulting in a system with scalability, versatility, and reliability similar to digital communication and computation.

Next, I present a new kind of material-robot system to enable methods of assembly automation. Rather than relying on global motion control systems for precision, mobile robots are designed to operate relative to their discrete material environment. By leveraging the embedded metrology of discrete materials, these relative robots have reduced complexity without sacrificing extensibility, enabling the robots to build structures larger and more precise than themselves. Multi-robot assembly is compared to stationary platforms to show system benefits for cost and throughput at larger scales.

Finally, I show a range of discretely assembled systems that blur the boundary between structure and robotics. Full-scale demonstrations include statically reconfigurable bridges, supermileage racecars, and morphing aero and hydrodynamic vehicles. Performance scaling is projected to new regimes, using case studies of turbine blades, airships, and space structures. These discrete systems demonstrate new, disruptive capabilities not possible within the limits of traditional manufacturing.

Thesis Supervisor: Neil Gershenfeld
Title: Director, MIT Center for Bits and Atoms

Discrete Mechanical Metamaterials
by
Benjamin Eric Jenett

This dissertation has been reviewed and approved by the following committee member:

Dr. Kenneth Cheung . . . .
Research Scientist
NASA Ames Research Center

Discrete Mechanical Metamaterials
by
Benjamin Eric Jenett

This dissertation has been reviewed and approved by the following committee member:

Dr. Kirstin Petersen . . . .

Assistant Professor

Department of Electrical and Computer Engineering, Cornell University

Acknowledgments

Thanks to Neil, for teaching the controversy, for live demoing, and for helping me become the quixotic researcher I am today. CBA is a singular place, and you are a singular Neil, and you've helped me literally make the most of my time at MIT.

CBA is an amazing and unique research lab, and it runs as well as it does thanks to all the people involved from shops to offices: Joe, Jamie, Kara, James, Ryan, Tom, John, and Lass. Thank you for keeping my spirits afloat, my shelves stocked, and my labs safe.

I've been fortunate to overlap with several generations of CBA students, so thanks to the old school, including Nadya, Amanda, Will, Prashant, Sam, Sara, and Matt. I look forward to working with all of you in the not too distant future, in fact, that sounds like a pretty sweet startup. . .

I'm leaving CBA in the capable hands of many new grads and postdocs but wanted to thank those who helped me with getting a lot of this work done. So, to Filippos, Chris, Amira, Alfonso, and Dixia (unofficial CBA), thank you.

I've also enjoyed spending the past 6 or so summers at NASA Ames, driving my Miata and working late in the CSL hangar. Thanks to Sean Swei, Nick Cramer, Daniel Cellucci, Greenfield Trinh, Olivia Formoso, countless number of interns, the inimitable Dr. Christine Gregg, and of course, one Kenneth Cheung. Kenny of course is the reason I got involved with CBA in the first place, and he still inspires me to work harder and think more creatively every day (wwkd?).

Thanks to Kirstin for being my final committee member. Her work has inspired me from day one, and I look forward to continuing to build simple robots for making complex things.

Thanks to my parents, both Jenetts and Chavez, and to my family near and far for their love and support.

Who did I forget? Ah yes, last but not least, thanks to my wife, Angelica, who has supported me through all the late nights and early mornings, who has assembled itchy carbon fiber voxels in the middle of the wilderness, who has done market research in her spare time on lightweight electric vehicles, who spent literally the snowiest and then the coldest winters in Boston history with me, followed by some toasty summers in the Bay area, to be followed by wherever life takes us next. When I do end up saving the planet, it'll only be because I have the support of the best wife in the world. Thank you for everything you do.

Oh, and also Yoko, she's the #1 puppa.

Contents

Chapter 1

Introduction

Engineering structures and systems today—from bridges to cars to airplanes– are informed and limited by the materials of which they are made and the processes used to shape, join, and configure these materials into end products. Scale, cost, and performance are inevitably drivers for the types of structures that exist– the implication being large, high performance structures are difficult and expensive to build. Turbine blades are relatively cheap, but quickly run into issues at lengths over 50m. Aircraft are more expensive and require dedicated infrastructure such as airplanes bigger than airplanes to transport the airplanes. And finally, space structures like the ISS take decades to install and cost billions of dollars, yet ultimately are limited by the material and shaping processes used to make any other given structures on earth. Humans are highly skilled makers, but that doesn't change the fact that making big things is hard.

And yet, perhaps dating back to Robert Hooke's observation of cork's internal cellular structure in 1665 [1], scientists and engineers have been fascinated with replicating the unique dynamic range demonstrated in natural systems. The microstructure of bone reveals sophisticated architectures to improve stiffness to weight that we could only mimic when designing the trusses of the Eiffel tower (Figure 1-1). In 1959, the physicist Richard Feynman inspired today's nanotechnology field by famously stating "There's Plenty of Room at the Bottom" [2], describing the fascinating potential of moving from meso to micro to nano scale. Now we are beginning to unlock some of this potential through rational design of material, structures, and systems across many length scales.

This thesis seeks to answer the question—is there also plenty of room at the top? More specifically, can the benefits of cellular construction seen in natural systems be extended to engineering systems at the meso and macro scale? To answer these questions, in this thesis I will draw not only from bio-inspired principles, but also from engineering principles that have proven to be scalable, versatile, and reliable. Specifically, these are principles seen in digital communication and computation.
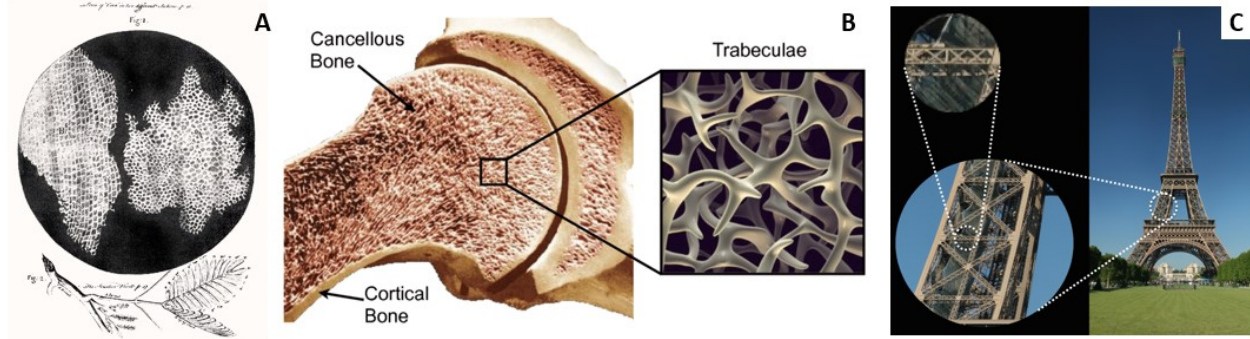
Figure 1-1: Natural and engineering systems with cellular hierarchy. A) Cork as observed by Hooke [1], B) Cortical bone [17], C) Eiffel tower (based on [19])

1.1 Digitizing material

In 1948 Claude Shannon invented the modern notion of "digital" when he showed that an analog signal could be converted to a digital representation (bits), and that it could then be communicated reliably in the presence of noise [3], thanks to error correction performed against a threshold function (Figure 1-2A). Von Neumann applied this principle to computation, showing you could compute reliably with unreliable components [4]. Today, the internet, supercomputing, and black hole imaging exist thanks to these discoveries. Digital fabrication also emerged with the first numerically controlled (NC) mill in the 1950s [5], which has led to the ubiquity of 3D printers, CNC cutters, and robotic manipulators throughout manufacturing today. And yet, when an object is made with a 3D printer, the design and motion control are digital, but the material is analog. Extruded thermoplastic is still susceptible to stochastic errors, and anisotropy and delamination result in flaws distributed randomly and inconsistently from part to part—two Eiffel towers 3D printed on the same machine might come out slightly different. What's missing is the benefits of digital in the material itself. From this insight came the notion of digitizing material, which can be thought of as something like Lego for engineering.

This is the approach taken in digital materials. Using modular building blocks, larger functional structures can be assembled. Parts have specific positions and orientations, meaning global precision comes from local metrology. Parts are reversibly joined, so they can be unjoined, recycled, and reconfigured. Dissimilar materials can be joined for heterogeneous assemblies. And crucially, as you build incrementally, you can detect and correct errors. Here the parts have information built into them, meaning child A and child B can both build the same tower with the same precision without needing to be precise builders themselves—the reliability, scalability, and versatility comes from the discretization of the material.

Together, this presents a new way of considering material as a controllable, designable system, and in particular, one which allows the benefits seen in digital systems to manifest in the physical world. Critical for achieving this, however, is a scalable assembly approach, which can benefit greatly from decades of advances in automation.
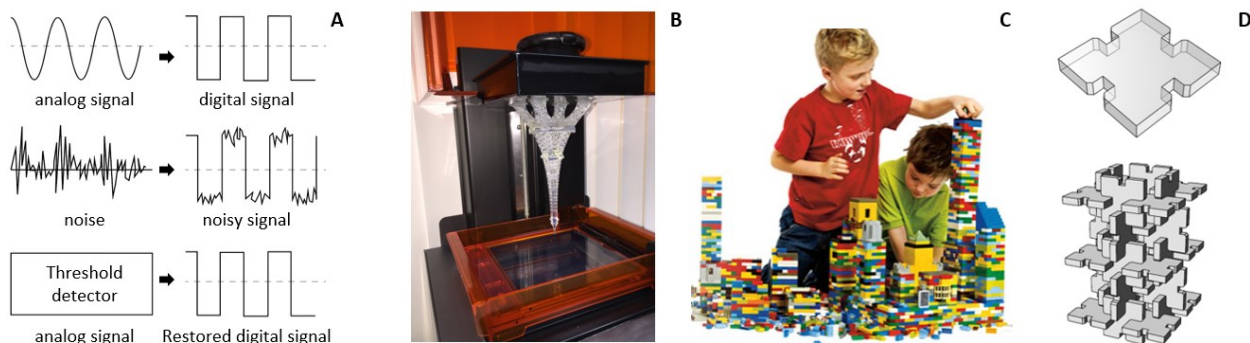
Figure 1-2: Digitizing information and material. A) Shannon's threshold theorem in action, B) Digital motion control to deposit analog material (image credit: formlabs), C) Error correction comes from information in the LEGO bricks rather than the child [160], D) GIK parts, the first proof of concept for digital material [48]

1.2 Automating assembly

Machines capable of processing tens of thousands of units per hour [6] and robots capable of dexterous manipulation [7] and agile coordination [8] represent just a few of the many examples of the large role automation plays in modern manufacturing. Some of the highest throughputs are seen at sub-mm scales, with parallelized lithographic processes for wafer fabrication [9], and metamaterial printing [10]. While digital fabrication processes, both additive and subtractive, can scale down to the sub-micron level, scaling processes up beyond several meters tends to encounter a range of issues related to performance, cost, and speed.

For example, consider a commercially available two-photon polymerization machine, which has resolution on the order of 1 micrometer (10^{-6}m), build size on the order of 100mm (10^{-1}m) and costs on the order of 10^6 USD/machine [11]. Macro-scale FDM machines, essentially industrial gantries with extruding end-effectors, boast build sizes of 10^1m [12], but are unlikely to have sub-mm (10^{-3}m) resolution, in addition to suffering from the aforementioned issues with layer-based deposition processes. Thus, roughly the same dynamic range (proportion of build scale to feature resolution) is offered, but with costs approaching 10^7 USD/machine, there is a possible super-linear cost-based scaling of achievable dynamic range. This is because building large, precise machines is expensive, and due to the inherent coupling of machine performance, size, and cost, there are significant challenges for realizing macro-scale (>1m) digital fabrication platforms with high quality and low cost. Today, you can 3D print a car [13], a bridge [14], a boat [15], or a shelter [16], but issues with cost of the machines and quality of the objects they produce illustrate the inherent challenge of scalability.

For inspiration on how to address this, we can look at one of the oldest known methods of fabrication with unparalleled range and diversity, and which also happens to be based on incremental assembly —biological growth. As a fabrication process, growth is incredibly efficient and undeniably scalable. Ribosomes assemble amino acids to long chains to form the basis of protein synthesis. This occurs at the nanometer (10^{-9}m) scale, resulting in organisms

with length scales ranging from bacteria (10^{-6}m) to humans (1m) to trees (10^2m), all unified with the same construction process [17]. One reason a ribosome can make something up to 10 orders of magnitude larger than itself is because the construction information is encoded in the material. The other reason is that while a single ribosome assembles amino acids at a humble speed (1 Hz), ribosomes can make ribosomes, allowing massive parallelization, which has been suggested as a strong incentive for making assemblers that can assemble assemblers from the parts they're assembling [18]. In this thesis, I remove complexity from the builder and put it into the material– think back to the LEGO analogy: a child can successfully make a tower because there is information embedded in the parts.
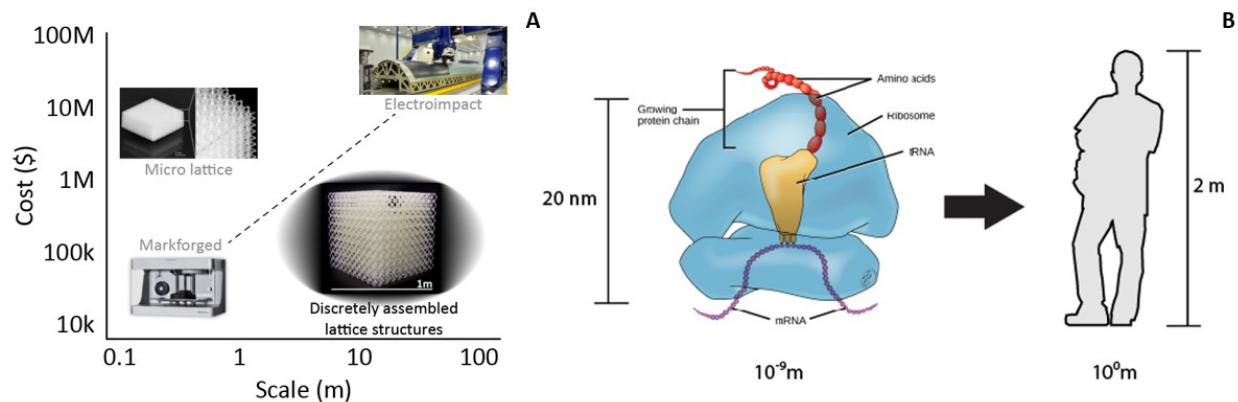
Figure 1-3: Scaling of digital fabrication and biological growth. A) Cost increases super-linearly with scale for human-made platforms, B) Yet the humble ribosome spans 9 orders of magnitude (based on [17]).

1.3   Scaling systems

Our many ages of civilization have been defined by materials: stone (100,000 BC), copper (10,000 BC), bronze (1,000 BC), iron (1,000 AD), steel (1900 AD), polymer (1950 AD), and now, arguably, silicon age (1980-present). But as technology progressed, ages also became defined by processes: the industrial age (1760), the machine age (1880), the space age (1957), and now, the information age. Overlaying the two, we begin to see how engineering structures and systems are informed, and also limited, by the materials of which they are made and the processes used to shape, join, and configure these materials into end products.

But what's missing from the materials and processes is the ability to design and engineer structures. In particular, we've gotten better at making structures which are more efficient. Typically, this means they use less of a finite resource to accomplish an objective—think of a solid stone arch bridge compared to a steel truss bridge. Owing not only to a better material, and processes to cut, shape, weld, and rivet that material, the steel bridge is superior because it was engineered for high performance while using as little material (which costs money) as possible without failing (which costs more money).

Millennia ago, 2.3 million stone bricks were carved, transported, and stacked to make the pyramid, reaching 150m in height and 5.2 billion kg in weight. Just over a century ago, the Eiffel tower was constructed from 18,000 cast iron bars, joined with rivets, to form a latticework reaching 300m and weighing one thousand times less (9 million kg). Today, roughly 2.6 million parts are assembled from supply chains that span the globe into high performance aerostructures measuring nearly 100m in wingspan and weighing hundreds of thousands of kilograms, yet are also capable of safely and reliable transporting people at speeds of almost 1000 km/h at altitudes of over 10 km. Today, advanced materials, processes, and system designs enable efficiency and performance not possible centuries or even decades ago.
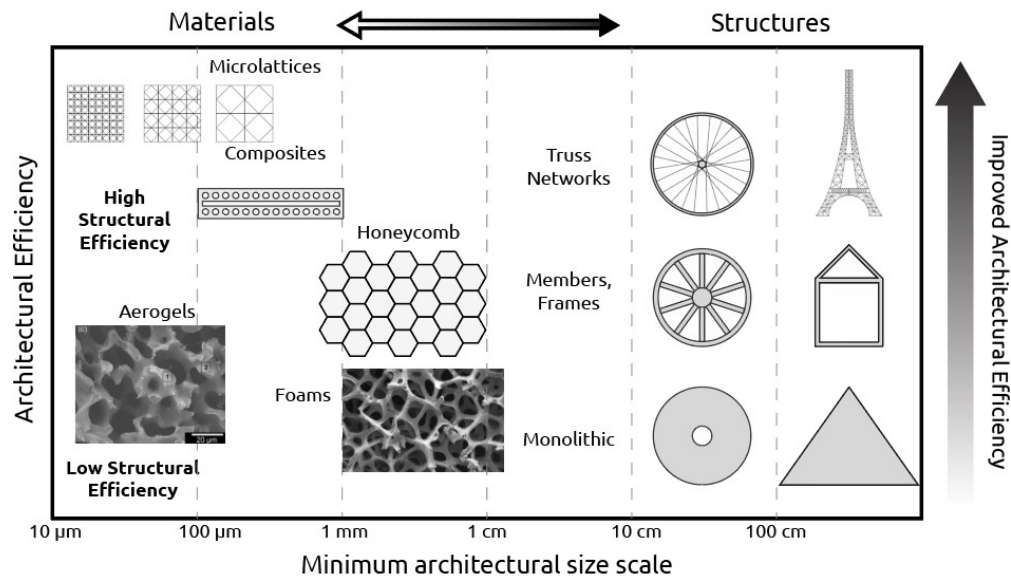
Figure 1-4: Material-structure systems across scales and levels of hierarchy, based on [19].

In our case, we're interested in the design of structures with architecture—geometric organization of internal members such that a desired outcome is achieved through this in addition to the shape of the members and the materials they're made from. The history of this particular vein of structural mechanics begins with material science, when Robert Hooke proposed a linear stress-strain relationship for bulk material in 1678. Moving up in hierarchy and forward in time, to around 1750, when Leonhard Euler and Daniel Bernoulli described material and geometry in the form of structural members such as beams, and calculated their governing beam equations for deflection, stress, and other structural responses. Next, around 1864, James Clerk Maxwell theorized networks of beams and linear members connected in 2D and 3D to make frames with calculable static equilibrium and stiffness [20]. This has brought us now from monolithic blocks of material to shapes with improved performance owing to 2D and 3D geometric properties, to spatially complex, yet predictable, systems. Now we are taking these principles and moving them back down into smaller scales, which enables us to invent new architected materials which are just as predictable as a truss bridge.

This level of recursion probably quickly the capacity or patience of the human brain,

so luckily we have computational design tools with hierarchical representation, multiphysics simulation, and numerical optimization, so now we can discover new designs we could never have imagined ourselves. So, if we have new materials, new processes, and new design tools, what are we going to make?

In Figure 1-5 I show concept art of a future aircraft factory. We can see completely new types of aircraft being made by a team of distributed robots, which are building a modular, cellular material. In my thesis, I'm looking to answer the question: how can we do this?
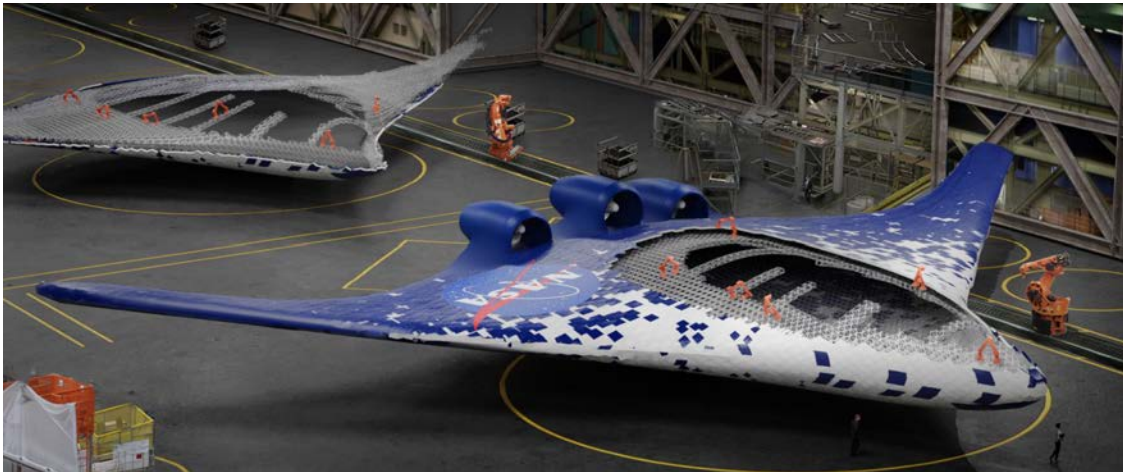
Figure 1-5: Concept art of a future aircraft factory, based on [21]. Expensive tooling and large monolithic parts have been replaced with discrete materials, assembled by relative robots into larger, on-demand discrete systems. (Image credit: Eli Gershenfeld, NASA ARC).

1.4 Contributions

To answer this question, I'm proposing new types of materials, with versatility and extensibility beyond standard engineering materials. I'm proposing new forms of automation, where a material-robot system offers simplification while enabling scalable construction. And I'm proposing new classes of systems, with disruptive capabilities not possible within the limits of traditional manufacturing.

First, I build on the topic of digital materials, which shows a finite set of modular parts can be incrementally and reversibly assembled into larger functional structures. I introduce a new range of attainable properties, such as rigidity, compliance, chirality, and auxetic behavior, all within a consistent manufacturing and assembly framework. These discrete mechanical metamaterials show global continuum properties based on local cellular architectures, resulting in a system with scalability, versatility, and reliability similar to digital communication and computation.

Next, I present a new kind of material-robot system to enable assembly automation. Rather than relying on global motion control systems for precision, mobile robots are designed to operate relative to their discrete material environment. By leveraging the embedded

metrology of discrete materials, these relative robots have reduced complexity without sacrificing extensibility, enabling the robots to build structures larger and more precise than themselves. Multi-robot assembly is compared to stationary platforms to show system benefits for cost and throughput at larger scales.

Finally, I show a range of discretely assembled systems which blur the boundary between structure and robotics. Full-scale demonstrations include statically reconfigurable infrastructure, supermileage racecars, and morphing aero and hydrodynamic vehicles. Performance is projected to larger scales and performance regimes, using a case studies of turbine blades for large scale wind energy capture. These discrete systems demonstrate new, disruptive capabilities not possible within the limits of traditional manufacturing.

Chapter 2

Discrete Materials

2.1 Background

Cellular Materials

The physical world is filled with cellular structures – both artificial, like truss bridges, and natural, like porous bone tissue. These entities, along with many other examples, from micro to meso to macro scale, are demonstrations of material and structural response being optimized through internal architecture rather than only by chemical composition. When designing structures, we can draw much inspiration from natural materials and systems. Wood and bone, for example, have beneficial stiffness-to-weight ratios as a result of their internal architecture, where porous, or cellular, structure provides sparsity without sacrificing the ability to sufficiently transfer loads and not fail. Due to their internal structure, these materials do more with less.

The research of cellular architecture mechanics (Figure 2-1) can be traced back to observation of hierarchy in natural systems [22], and more recently to investigations of stochastic polymeric foams, whose cellular structures were studied and manipulated by Lakes to create the first negative Poisson ratio material [23]. Seminal work by Gibson and Ashby was published around the same time [24][25], describing analytically the behavior of cellular solids as a network of plates or beams, whose geometry and connectivity can be controlled to tailor macroscopic behavior, thus enabling design of architected materials [26] such as periodic structures with improved stiffness over foams associated with higher degrees of geometric connectivity [27]. However, it took until the introduction of additive manufacturing decades later for these complex geometries to become realizable in physical form [28]. Prior to this, in an adjacent field, the notion of artificially controlling local cell properties to design macroscopic behavior was already being explored, tested, and proven.

Metamaterials

While the function of the materials described above is primarily mechanical, it was from a somewhat non-structural field that the first notion emerged of an artificial material with novel properties controlled by local, cellular design. Electromagnetic metamaterials possess synthetic properties that allows them to interact with EM waves in ways that naturally

occurring materials cannot. In particular, when interacting with visible wavelength of the EM spectrum, a material's refractive index n describes how light travels through the material and is very important for how we perceive our visual world, in addition to the invisible parts of the spectrum. Two parameters, the electric permittivity and magnetic permeability , can be used to define a material's refractive index of electromagnetic radiation $n = \sqrt{\epsilon_r * \mu_r}$, where r denotes that property relative to vacuum. Generally in the observable world of optics and electromagnetics, all naturally occurring materials appear to a positive refractive index. In 1967, Victor Veselago theorized of an engineered isotropic material with controllable values of electric permittivity (ϵ) and magnetic permeability (μ) [29], making it possible to have a negative refractive index (NRI), which can be used to make then-impossible objects such as near-perfect lenses that focus beyond the diffraction limit.

It wasn't until 33 later that a series of experiments by John Pendry [161], David Smith [162], and Richard Shelby [163] proved this theory to be correct. One critical insight was that the cell unit size had to be smaller than the wavelength, ie: for microwaves with γ = 10-100mm, unit cells have to be on the order of 1-10mm. This way, at the wavelength scale, the collective properties of the cells govern interaction, as opposed to individual cell features (Figure 2-2). This is a critical insight that helped reduce metamaterials to practice, and combined with modeling methods such as effective medium theory [30], allowed for the design and implementation of a range of metamaterials across several length scales, ranging from optical wavelengths with nanometer scale features [31] to micro and radio wavelength with up to centimeter scale features [32].

Mechanical Metamaterials

Returning now to mechanics, we are interested in controlling separately the elastic constants of an engineered material (modulus of elasticity E, bulk modulus K, shear modulus G, and Poisson's ratio v) to design new exotic behaviors. With the introduction of additive manufacturing, it was finally possible to materialize these proposed artificial lattice structures. Seminal work demonstrated stiff, ultralight lattice materials [28], and has since been improved, resulting in mechanical metamaterials with superior stiffness and strength at ultralight densities [33] with multiscale hierarchy [34] (Figure 2-3). Benefits of nanoscale features further expand the exotic property parameter space [35] and architectures featuring closed-cell plates have shown potential for approaching the theoretical limit for elastic material performance [36]. Across all of these, the metamaterial approach is consistent: local cell architectures are designed specifically to produce novel global properties.

Other designs seek to utilize compliance, which can be attained through internal geometric mechanisms [37], or through base materials capable of large strain [38]. Internal architectures can be designed to transmit or respond to load in other non-standard ways. Auxetic metamaterials exhibit zero or negative Poisson's ratio [39]. Internal, re-entrant architectures produce contraction perpendicular to compressive loading, and expansion perpendicular to tensile loading, counter to traditional continuum material behavior [40]. Chiral metamaterials exhibit handedness based on asymmetric unit cell geometry. These designs produce out of plane deformations, such as twist, in response to in plane loading [41].
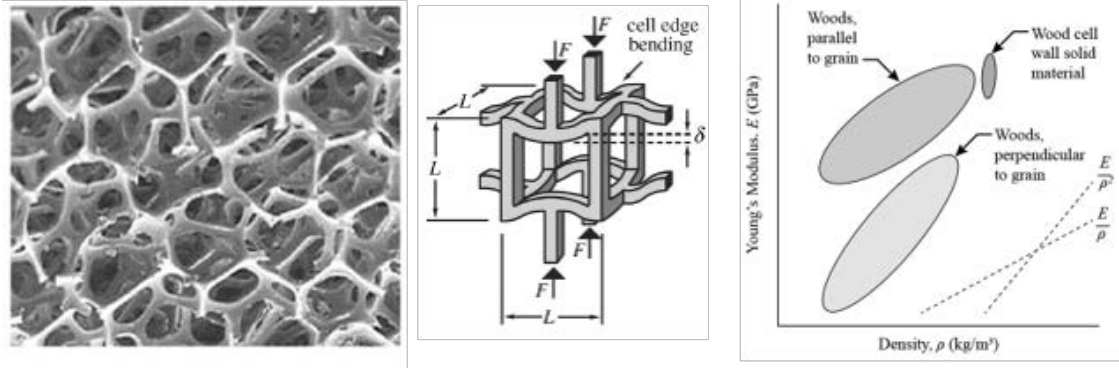
Figure 2-1: Cellular materials (L to R): Closeup of a natural cellular material, diagram of cell beam mechanics under loading, comparison of effective cellular material properties with different internal architectures made from the same base material, from [22] and [25].
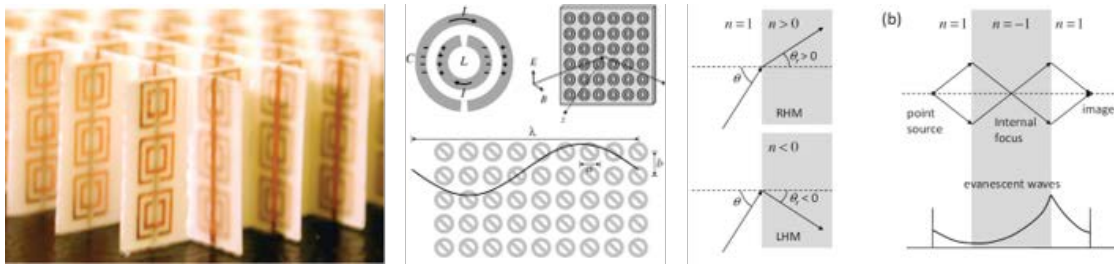
Figure 2-2: Electromagnetic metamaterials (L to R): seminal experimental work by Pendry et al [161], diagram of an individual split ring resonator (SRR) cell whose features and spacing are sub-wavelength to result in an effective material with novel properties, negative refractive index material can be used to make near-perfect lenses with sub-diffraction limited focus, from [47]
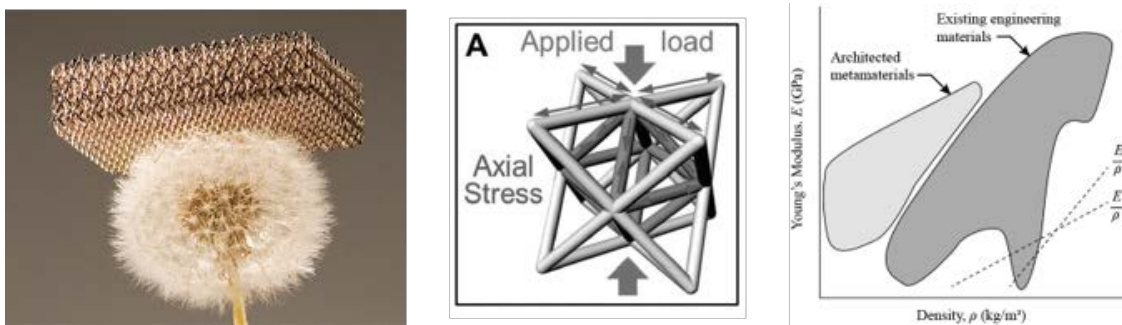
Figure 2-3: Mechanical metamaterials (L to R): example of ultralight density metal microlattice [28], diagram of an rationally designed octet unit cell which results in a stretch-dominated lattice [33], new parts of material property space can be accessed with this approach.

Digital Materials

As mentioned previously, digital materials are effectively assembled metamaterials (Figure 2-4). Here, modular parts with specific geometries and orientations are reversibly assembled to form larger, functional materials and structures. Initial proofs of concept demonstrated a generalized part geometry for press-fit construction of planar elements [48] and a separate approach used spherical voxels joined with a binder to produce user defined geometries [49]. This was further developed into functional electronic materials using two materials types to make heterogeneous assemblies [50]. This led to a discrete robotic construction kit, consisting of rigid, flexural, and actuation (magnetic core and voice coil) building blocks, which was used to produce small crawling robots and stepping motors [51]. All of the above digital materials use press-fit connections between parts. This simplifies construction, and suffices structurally for the given applications, but for more demanding applications, additional capacity at the joint is required. Here, we see reversible fasteners employed to complete the structural load bearing profile of the joint.
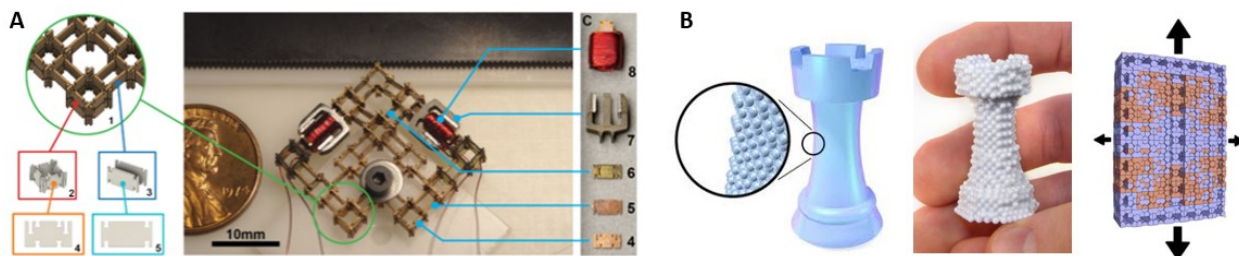
Figure 2-4: Digital materials. A) Rigid, flexure, and actuated building block parts comprise a discrete robotic construction kit [51], B) spherical voxels with binder can be rapidly assembled by a machine, and interlocking parts can be composed into larger functional cells and structures [49].

Discrete Lattice Materials

A particular subset of digital materials seeks to build high performance lattice structures based on cellular solid theory. I term these discrete lattice materials. Here, artificial cellular structures are decomposed into discrete, modular parts which are reversibly assembled to form space-filling lattice structures with tunable, exotic mechanical properties (Figure 2-5).

The notion of discrete lattice materials was first explored by Cheung and Gershenfeld [52]. Here, a Cuboctahedron lattice is decomposed into modular, cruciform parts. The vertices of these parts interconnect and are locked with a metal shear clip to make a rigid, space-filling lattice. Parts are manufactured in batches using a custom tool for winding carbon fiber filament, impregnating with resin, and curing. This monolithic prism is then sliced into thin sections, which are the discrete lattice elements. Due to the fiber alignment resulting from the winding process, any loading transferred axially through struts is aligned with the fiber orientation, thus resulting in a 3D quasi-isotropic carbon fiber reinforced polymer (CFRP) composite. This was the first published ultralight material with linear specific modulus scaling, and the resulting effective modulus was an order of magnitude higher than then-reported metal microlattices [28].

The aforementioned CFRP lattice part production method was slightly laborious, making it difficult to produce lots of part quickly. The work presented by Gregg et al [53] showed that parts can be mass-produced, resulting in economic production at scale. Here, a full octahedra is injection molded as a single, monolithic part from glass fiber reinforced polymer (GFRP) (Figure 2-5). It was shown that noticeable chopped fiber alignment resulted from strategic flow gate locations, though knit lines were unavoidable and thus sometimes resulted in suboptimal, strength-based, failure modes. Voxels have a 76.1mm (3in) pitch, and they are joined to neighboring voxels using 0-80 nuts and bolts. This material system used to build a 4m span ultralight lattice aerostructure consisting of over 4,000 voxels. This was enabled by the cost efficient and high throughput manufacturing process. Additionally, experiments were performed where 4x4x4 specimens were tested to initial failure, then that damaged voxel was replaced, and the post-repair specimen showed nearly 100% structural recovery.
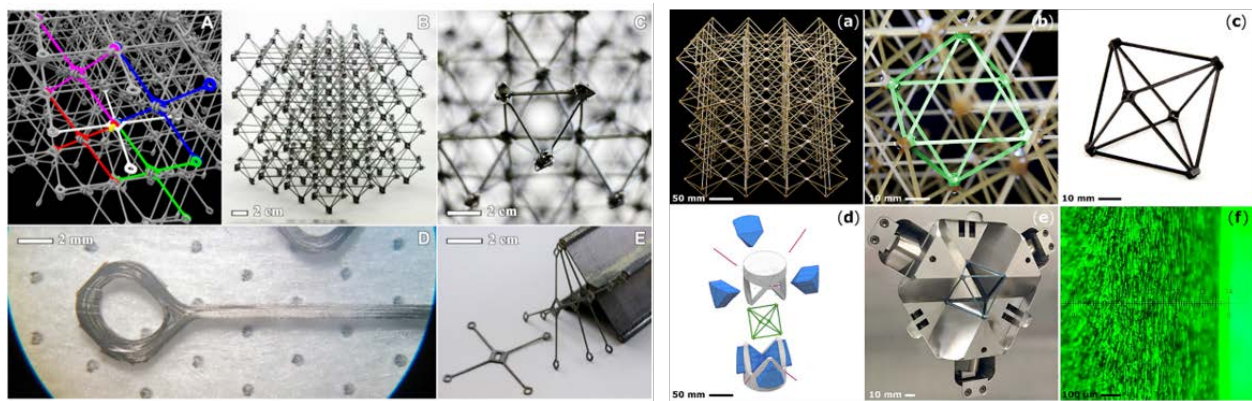
Figure 2-5: Discrete lattice materials. (L) Wound, cured, and sliced CFRP lattice components by Cheung and Gershenfeld [52], (R) Injection molded GFRP octahedra voxels by Gregg and Cheung [53].

Observations

Given this as background, there are several key themes to keep in mind as I introduce my new material system:

Performance vs scale: natural cellular materials show multiple levels of hierarchy, and through this internal architecture, improved mechanical performance for eg: stiff tree limbs. Engineering systems can achieve this too, but to be scalable, there must be reliability as shown in digital systems, else premature and unpredictable failure modes may occur.

Cost vs complexity: nature achieves its fantastic biodiversity of its millions of species all from 20 amino acids. It is through their spatial programming that function emerges. While digital fabrication processes show promise to achieve arbitrary levels of complexity, achieving this at scale comes with great cost. Modularity seen in biological growth can be emulated in artificial processes.

Constructability: this thesis is focused on building useful structures and systems; the practical aspects of construction must be considered from the beginning. Simple, repeatable processes (automated or not) should work in a way that allows hundreds or thousands of repetitions, and be able to quickly identify and fix inherent process flaws.

2.2   Discretely Assembled Mechanical Metamaterials

In this section, I present a construction system for mechanical metamaterials based on discrete assembly of a finite set of modular, mass produced parts. I demonstrate experimentally the desired metamaterial property for each part type, and combined with numerical modeling results, display other novel, unexpected properties. A modular construction scheme enables a range of mechanical metamaterial properties to be achieved, including rigid, compliant, auxetic and chiral, all of which are assembled with a consistent process across part types, thereby expanding the functionality and accessibility of this approach. The incremental nature of discrete assembly enables mechanical metamaterials to be produced efficiently and at low cost, beyond the scale of the 3D printer.

2.2.1   Effective Lattice Properties

In Figure 2-6, I show a log-log plot of density vs Young's Modulus for existing engineering materials. I am adding to this the blue area to the left labelled "Architected Cellular Solids", which exist in a previously unoccupied part of parameter space. Using cellular solid theory (Figure 2-7), we can project into this space and predict the behavior of a lattice design (labelled d) based on a) the *material* it's made from (say, carbon fiber, or aluminum), b) the *topology*, which refers to the particular lattice geometry, and c) the relative *density*, which is a function of cell size and beam thickness. Next I will walk through these steps in detail.
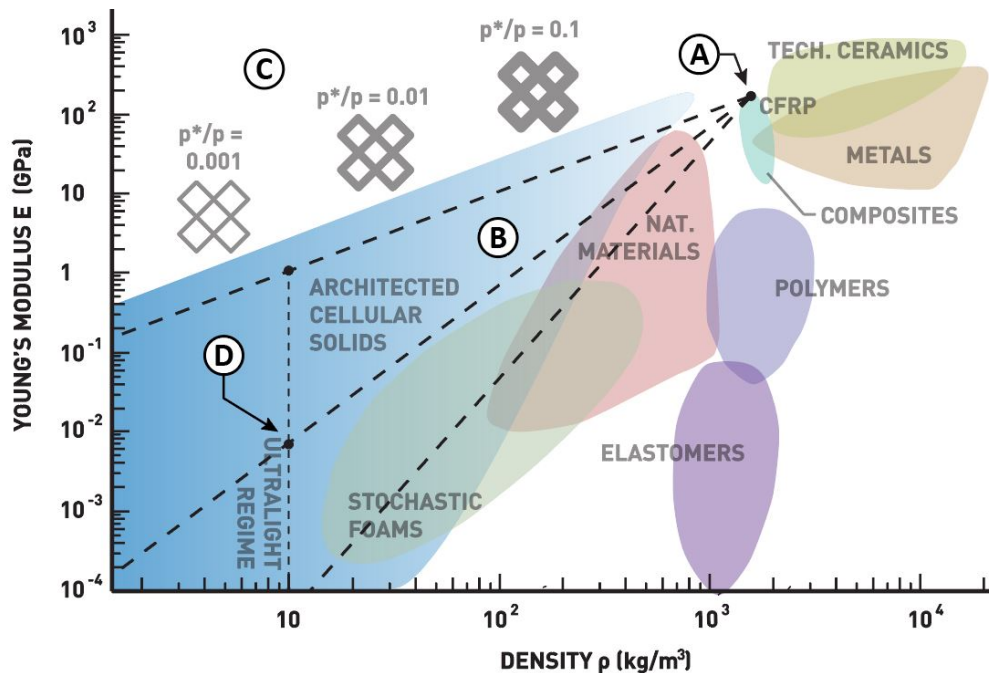
Figure 2-6: Ashby style log-log plot of density vs Young's modulus for engineering materials, based on [34]. Beginning with a base material (A), then the lattice geometry (B) that provides the scaling value/slope, we project to a certain relative density (C) that should give us a good estimate of lattice performance at (D).

26
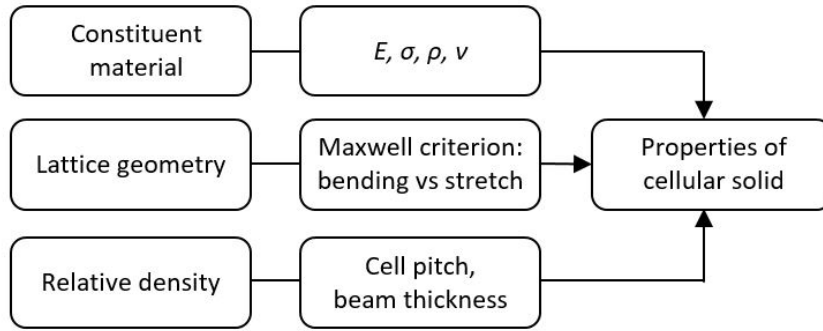
Figure 2-7: Lattice design parameters used to produce new cellular solids, from [26].

Material

While choosing a base material may seem trivial, it has significant consequences in terms of both structural mechanics and fabrication. The yield strain of a material is the proportion of strength to stiffness (σ/E) and describes how a material responds to deflection to the point of plastic deformation. For materials with low yield strains such as ceramics (10^{-4}), yielding will occur before buckling, whereas materials with high yield strain like elastomers (10^0) buckle before yielding. This will play a significant role in designing our lattice in the following sections. In terms of fabrication, not all materials are compatible with certain processes. Limits exist for molding, milling, cutting, pressing, folding—picking a material requires knowledge of how it can be processed into parts.

Geometry

Lattice geometry can be stochastic or periodic, we focus on the latter. Space filling polyhedra help describe a regular set of possible designs, noting that in our case we'll want to use shapes that satisfy constraints of being statically determinate known as Maxwell criteria. Looking at the joints of these lattices, we can also describe them based on their connectivity, or the number of members terminating into a joint to create a continuous, load bearing beam network. Connectivity relates to how loads are resolved internally—low connectivity results in bending dominated lattices, which have low stiffness to weight, compared to high connectivity, which results in stretch dominated lattices, meaning internally, members are sufficiently triangulated in 3D space to produce a network of beams operating solely in axial tension or compression, which results in a higher stiffness to weight ratio, which is what we're after. We want to balance performance with practicality, and prior art had shown that vertex connected octahedra have a lower connectivity than some of the higher geometries, but still have good scaling values.
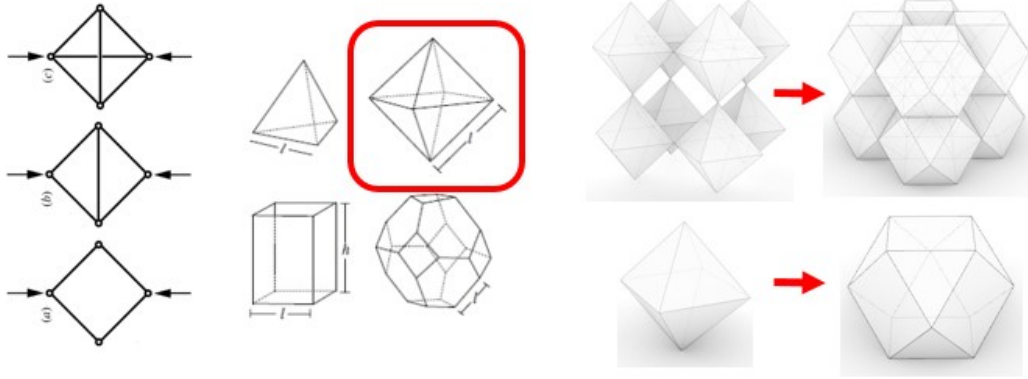
Figure 2-8: Lattice geometry. (L to R) 2D connectivity of over, exact, and under constrained frames, polyhedra which satisfy Maxwell's criteria extended to 3D with octahedra highlighted, vertex connceted octahedra vs. face connected cuboctahedra. From [26].

Density

A key characteristic of a cellular solid is its relative density, which can relate many macroscopic properties of the lattice such as stiffness and strength to the properties of the material that constitutes the lattice. Combined with the previously mentioned material and geometry properties, this relationship takes the form of a power law, where for example the ratio of macroscopic stiffness E^* and constituent material stiffness E are related to the ratio of cellular solid density ρ^* and constituent material density ρ [26]: $E^*/E = k(\rho^*/\rho)^a$.

Here, a depends on the geometry of the lattice selected, and k depends on the direction of the applied load for given geometry. Relative density also relates to beam failure mechanics, which will be explained in Section 2.2.3.

By varying the relative density, the macroscopic behaviors of a cellular solid can be tuned to precisely the desired compliance and mass. In particular, below a density of 10 kg/m^3, cellular solids are considered to be "ultralight" [33]. Lattices composed of high-performance materials like alumina or CFRP approach the stiffness of elastomers, but with many orders of magnitude lower mass density. For example, we regularly produce materials with an effective stiffness similar to that of a solid block of rubber, which, if of sufficient cross section, can actually appear to be quite stiff. However, that stiffness comes at a price of mass. We can produce a volume of material with the same stiffness but at a density over 200 times lighter.

Combined, these parameters are used to define a novel cellular solid. Now I will describe how we go from the material, geometry, and density to a discrete set of parts for mass production and assembly.

2.2.2 Discrete Lattice System

Having selected the cuboctahedra lattice, I created a new geometric decomposition. The cuboctahedra lattice gets decomposed into face connected cuboctahedra voxels, which then get decomposed into flat, square-shaped face parts (Figure 2-9). These should be simple to manufacture, and have a straightforward path to assembly, but before I discuss that, I want to show how we actually engineer this particular lattice to behave properly

For proper lattice behavior, the assembled structure should act as a network of beams. Specifically, both the macroscopic stiffness and strength criteria should be governed by local beam properties, and not by the joints. To ensure this, we must design the joints to have higher stiffness and strength values than the beams, that way, from a structural point of view, the joints disappear, and we're left with the network of beams that we wanted originally, as if they were made monolithically.
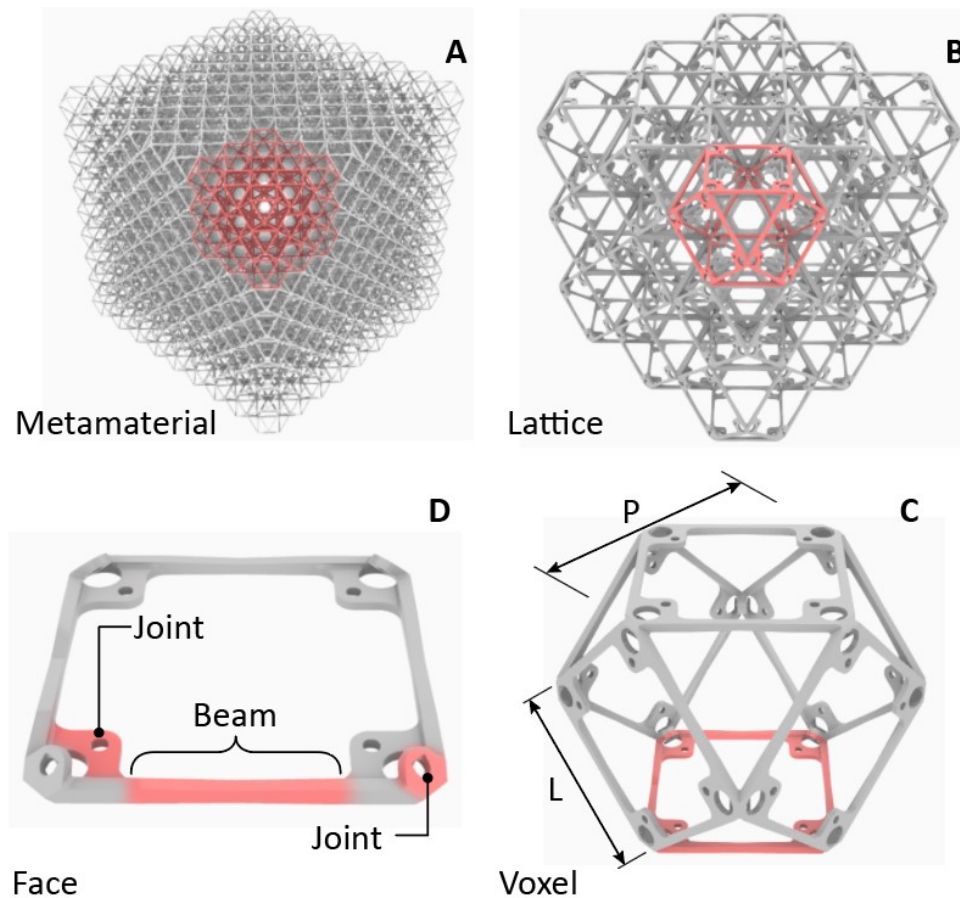
Figure 2-9: Discrete assembly system. A) 3x3x3 lattice consists of 27 individual voxels, B) Voxels consist of six individual faces, C) Faces consist of beams and joints

A lattice, or a mechanical metamaterial consisting of a periodic network of interconnected beams, can be described, and its performance predicted, analytically. I can describe lattices as stretch- or bending-dominated, based on how they resolve external forces as a function of their internal beam connectivity, which corresponds to Maxwell's frame rigidity criteria

extended to 3D (5). Stretch-dominated lattices, such as the octet, have higher connectivity (Z = 12) and higher stiffness to weight than bending-dominated lattices, such as the kelvin, which have lower connectivity (Z = 4) (7).

In this work we use the cuboctahedra lattice (referred to as Cuboct) geometry, which is uniquely positioned between low and high connectivity (Z = 8) yet has been shown to have stretch-dominated behavior, in both microlattice implementation (28) and as discretely assembled vertex connected octahedra.

In Figure 2-9, I show a new decomposition using face-connected cuboctahedra voxels which produces the same lattice geometry but has additional benefits to be discussed herein. Voxels are discretized into faces, which consist of beams and joints. There are two types of joints: inner-voxel joints are the points at which 6 separate faces are joined to form a voxel, and inter-voxel joints provide the vertex to vertex connections between neighboring voxels at along a single face. A joint consists of nodes, which are the geometric features on the part providing the fastening area, and the fasteners, which are mechanical connectors. Based on the material and geometric properties of each subsystem, local properties can be controlled to ensure proper global, continuum behavior. In this case, our lattice should behave as an interconnected network of beams. Therefore, we wish to design joints to possess significantly higher effective stiffness and strength than the beams they connect. In this way, the global effective stiffness and strength of the lattice are governed by those subsystems with the lowest relative value.

2.2.3   Structural load paths

To better understand the inner workings of the lattice system, the rigid cuboct is taken as the "base" unit, which is used for describing system architecture such as critical dimensions and relative structural performance metrics. Figure 2-10A shows a 2x2x2 cube loaded in tension in the positive Z direction. In-plane beams parallel to the loading direction (XY and YZ planes) go into tension, which results in the out of plane members (XY plane) go into compression. Assuming periodic boundary conditions, a single representative voxel is shown in Figure 2-10B, where external loading and reaction forces at outward facing nodes are shown. XY plane nodes logically go into tension on the top and bottom faces of the voxel. XZ and YZ faces have combined tension and compression reaction forces at the nodes, while all beams are in tension. Due to the construction employed, in-plane face loads are transferred through adjacent nodes to the outward face, which is normal to the load path direction, as shown in Figure 2-10C. At the junction of four, in-plane voxels, there are 3 possible load paths: all compression, all tension, or mixed tension and compression (Figure 2-10 G-I). All compression is resolved through contact pressure of the node area, which helps in reducing the resulting pressure magnitude. All tension loads transfer from in plane beams, through inner-voxel joints, then through rivets which are parallel to the load path but fixtured to faces which are normal to the load path. Combined loads have overlapping, orthogonal load paths. Having determined the unique load paths that occur, we can determine stiffness and strength of each of the subsystems, from the fasteners, to the joints, to the beams, and ultimately, to proper continuum lattice behavior.

30
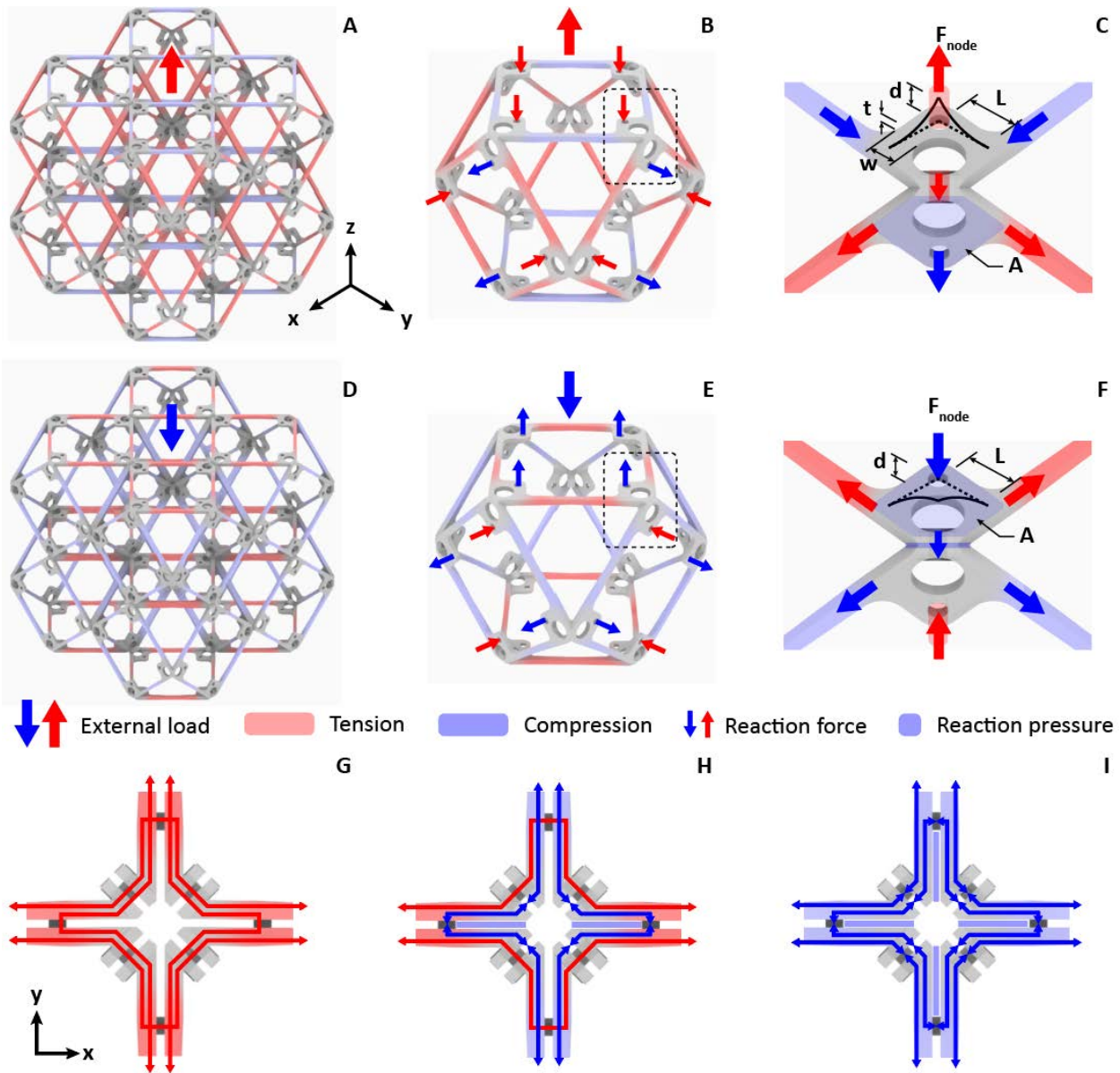
Figure 2-10: Load paths in rigid Cuboct lattice. A) 2x2x2 cube under uniaxial tension in Z direction, B) sample voxel under tension in Z direction, C) detail of corner joint showing internal load transfer, D) 2x2x2 cube under uniaxial compression in Z direction, E) sample voxel under compression in Z direction, F) detail of corner joint showing internal load transfer, G) illustration of cross-axis load transfer at joints, showing XZ and YZ planes in uniform tension, H) mixed compression and tension, and I) uniform compression.

The fasteners are 3/32" diameter aluminum domed head blind rivets, with a listed tensile strength of 578 N (130 lbf), thus the rivet component of a voxel-to-voxel joint has a tensile strength of 2,312 N (520 lbf). This is verified experimentally, as shown in Figure 1. The rivets yield strength is 2,125 N, or 531 N per rivet (92% of the listed capacity), and a combined axial stiffness k = 1,575 N/mm. When tensile forces are transferred across a joint, the load

path goes from the rivet to the inter-voxel node, which consists of a rivet mounting location and a pair of armatures that extend from the mounting location to the node, coincident with the termination of the two beams into said node.

To avoid stress concentrations, fillets are used at the intersection of the armature and the beam, and this is validated in FEA. Critical stress σ_{crit}=110 MPa results from a tip load F_{tip}=90N, for a node load F_{node}=180N, which is roughly one third the tensile capacity of the rivet. An entire face consists of four of these joints, giving an overall capacity of 720 N. The FEA model also provides the linear-elastic bending stiffness of the node, which is 138 N/mm, and an entire voxel-to-voxel node stiffness of 552 N/mm, which is roughly one third the stiffness of the rivets. As seen in Figure 2-10, these armatures have a length L, a thickness t, and a width w. They can be treated as cantilever beams, each one taking a tip load of $F_{node}/2$. This will result in a deflection $d = FL^3/3EI$, where $I = wt^3/12$. Using our material's elastic modulus E = 2 GPa, and length l = 5mm. I expect failure of this armature at the root, where the largest moment and shear forces are. The critical stress of a cantilever beam is σ_{crit}=My/I, which can be rearranged to determine the critical load $F_{crit}= \sigma I/ly$, where y=t/2. Plugging in our as-molded parameters (t = 1.5mm, w = 4mm, and σ = 110 MPa), I get F_{crit}= 234N, which provides a reasonable factor of safety for this feature.

2.2.4   Beam Behavior

Here we discuss yield strength as the point at which initial beam failure occurs. The mechanism for this failure is important for understanding how the discrete lattice system behaves as a continuum lattice. As shown in Figure 2-10, external loads are resolved internally as beam tension and compression. Beam tensile failure is determined by constituent material and beam cross sectional area, with the critical force $F_{crit}= \sigma * A$.

Beams in compression fail in different ways depending on their slenderness ratio, defined as effective length over radius of gyration, $(l/k) = L_{ef}\sqrt{A/I}$. This is used to describe three compression member types in terms of their failure modes: short, intermediate, and long. As cellular solid theory is only applicable at relative densities under 30% , we limit our analysis to beams with slenderness ratios above 4:1 (see Figure 2-11). For sparse Euler buckling is the elastic stability limit, and is applicable to long members, but as slenderness ratio goes to zero, Euler buckling predictions go to infinity. Therefore, the Johnson parabola curve considers material yield strain (σ/E), the strain at which the material ceases to be linearly elastic [30], in calculating the inelastic stability limit. The transition between long and intermediate occurs at the critical slenderness ratio, which can be calculated using material and beam geometric properties (40).

Our material is a GFRP with an elastic modulus E = 2 GPa and yield strength σ = 107 MPa, and we can calculate critical slenderness using $(l/k)_{cr} = \sqrt{2\pi^2 E/\sigma} = 19.21$. Based on our part geometry, we find our beam slenderness to be 29.5. Therefore, our beams should fail based on Euler buckling at a critical load $F_{cr} = 70$N. Using the yield strength values from our material, we can determine the experimental value for critical beam load by dividing the global peak load (7.8 kN) by the cross sectional voxel count (16), resulting in 487.5 N/voxel, 121.9 N/node, which is carried by two beams at 45 degree angles, giving a beam load of 86N.
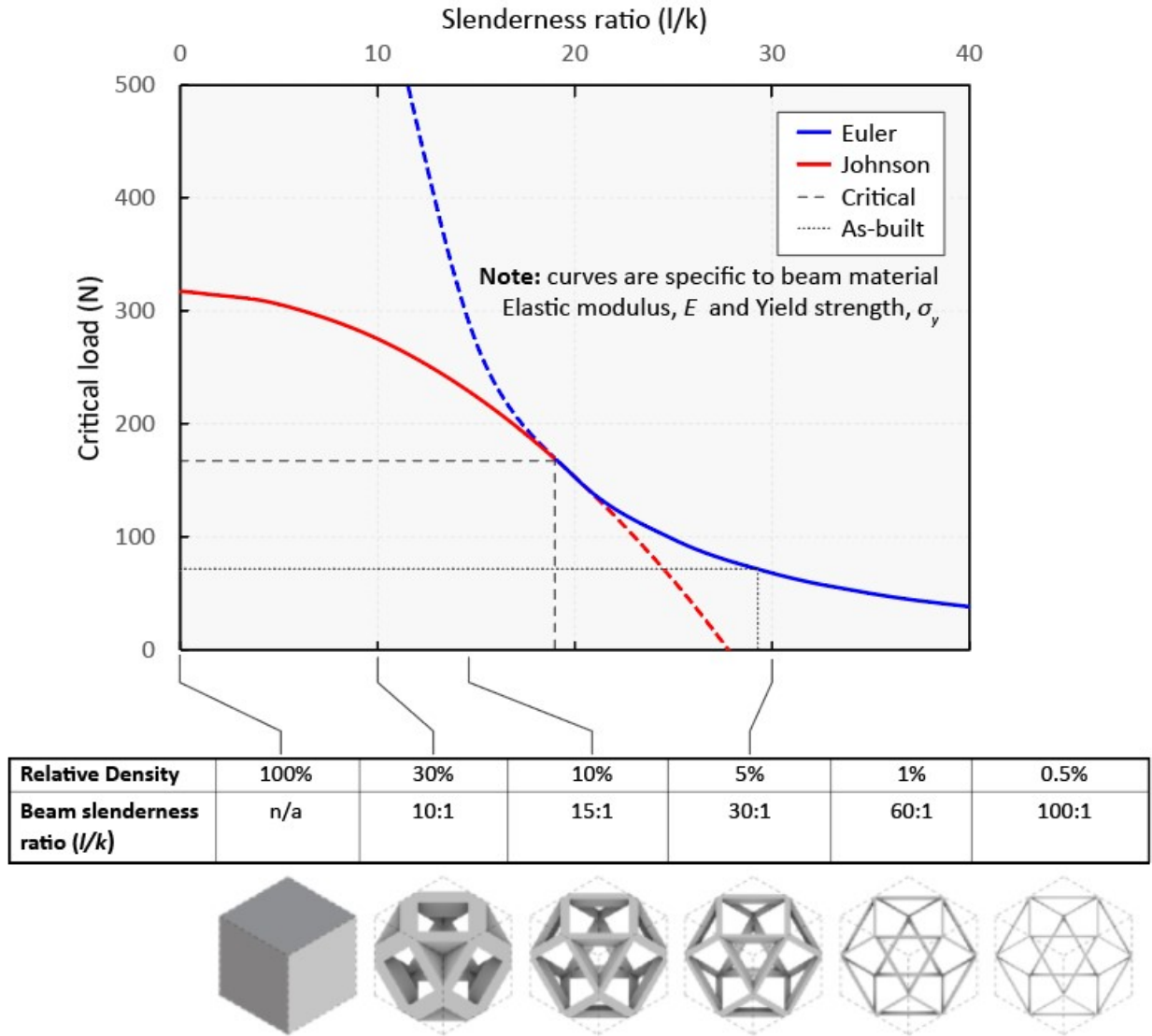
Figure 2-11: Beam behavior showing relationship between compression member slenderness ratio, failure mode, and resulting lattice relative density. Beams above the critical slenderness ratio (l/k = 29.5) fail by elastic buckling, beams below fail by plastic buckling. Relative densities above 30% are invalid for cellular theory to apply.

2.2.5   Modeling

Lattices are designed as network of beams, and as such, their modeling can be drastically simplified through the use of sparse matrix solvers for well-established beam models such as Euler or Timoshenko. This allows a beam to be described in as few terms as possible: their endpoints in the cell coordinates, cross-sectional area, density, second area moments of inertia, and elastic moduli (tensile E, shear G, and torsional J). Assuming global stability (ie: properly constrained, no mechanisms), a load/displacement relationship can easily be calculated by summing all the beam contributions at each node in the lattice and solving, at least in the linear-elastic case, which is usually where we are interested, at least initially. For a single cuboct voxel with 24 beams joined at 12 nodes, there are 72 degrees of freedom to solve for (3 translation and 3 rotation at each node). Fully meshed FEA models are used only when needed to inspect local stress concentrations in a solid-based model, which have much larger computational requirements. Comparion between these two approaches are shown in Figure 2-12 and 2-13.

2.2.6   Production

The results of characterizing the as-molded properties of the GFRP material are shown in Figure 2-15, where the elastic modulus and yield strength vary based on the location of the gate and resulting knit lines. For injection molded FRP, fiber concentration reduces with distance from the gate. The highest concentration is around the gate, resulting in relatively high stiffness, but residual thermal and mechanical stress from the injection process cause a relatively lower yield strength. At the end of the flow, knit lines can result in around 50% yield strength reduction (27), in addition to reduced elastic modulus owing to distance from the gate. Therefore, controlling the location of these features is important. I want to avoid having the gate or knit line occur near the middle of the beam, where stress will be magnified during beam buckling induced strain. I also want to avoid having the end knit line occur on the inter- or inner-voxel nodes. Aside from operational stresses, during the voxel construction the outward force of the rivet expanding from actuation causes circumferential stress in the node area which can result in rupture along knit lines.

The resulting gate and knit line locations are shown for the rigid part type in Figure 2-15A, with contours indicating the flow location at increasing time steps. To characterize the range of as-molded material properties, specimens from each beam group were extracted from the faces and tested in uniaxial tension until failure, and the resulting elastic modulus and yield strength were calculated, as shown in Figure 2-15B. These findings confirm several key aspects of part production. Beam group 1, which is closest to the gate, has high fiber content, thus a high elastic modulus, but has lower yield strength due to residual stress caused by gate proximity. Beam groups 2 and 3 have flows that move continuously from one end to the other, which promotes axial fiber alignment, giving a higher elastic modulus and yield strength. The last beam group has the lowest modulus, due to being at the end of the flow front, and the lowest strength, due to knit line proximity.

	A	B	C
Nodes:	83,357	156	12
Elements:	44,500	192	24
DoF:	277,788	936	72
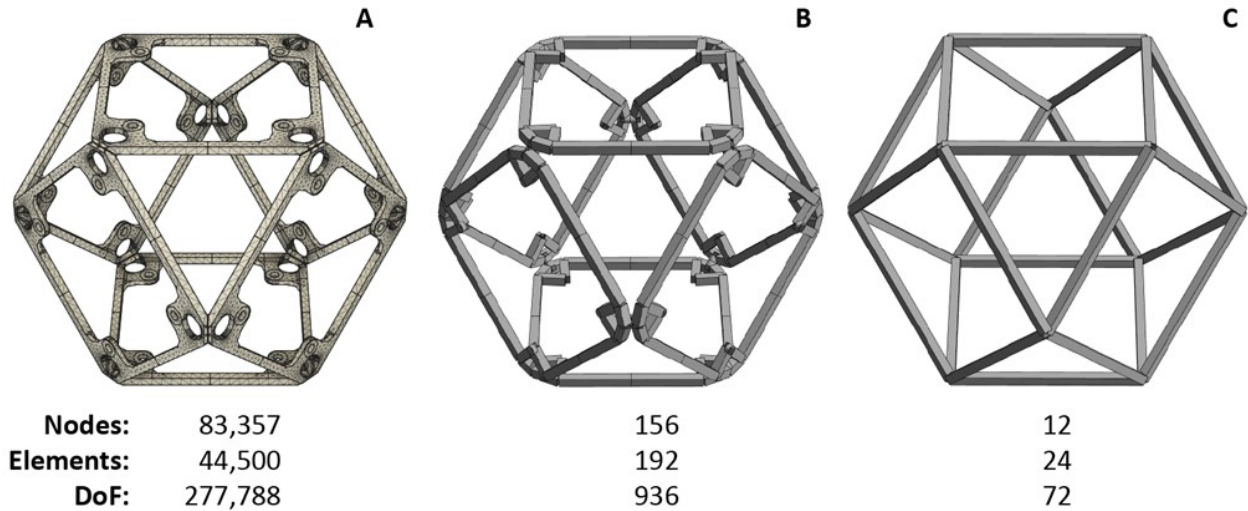
Figure 2-12: Comparison of numerical models for a single rigid cuboct voxel. A) NASTRAN (built in FEA for commercial CAD/CAE software, Autodesk Fusion), B) Beam model with additional model detail of joints, C) Theoretical beam model.
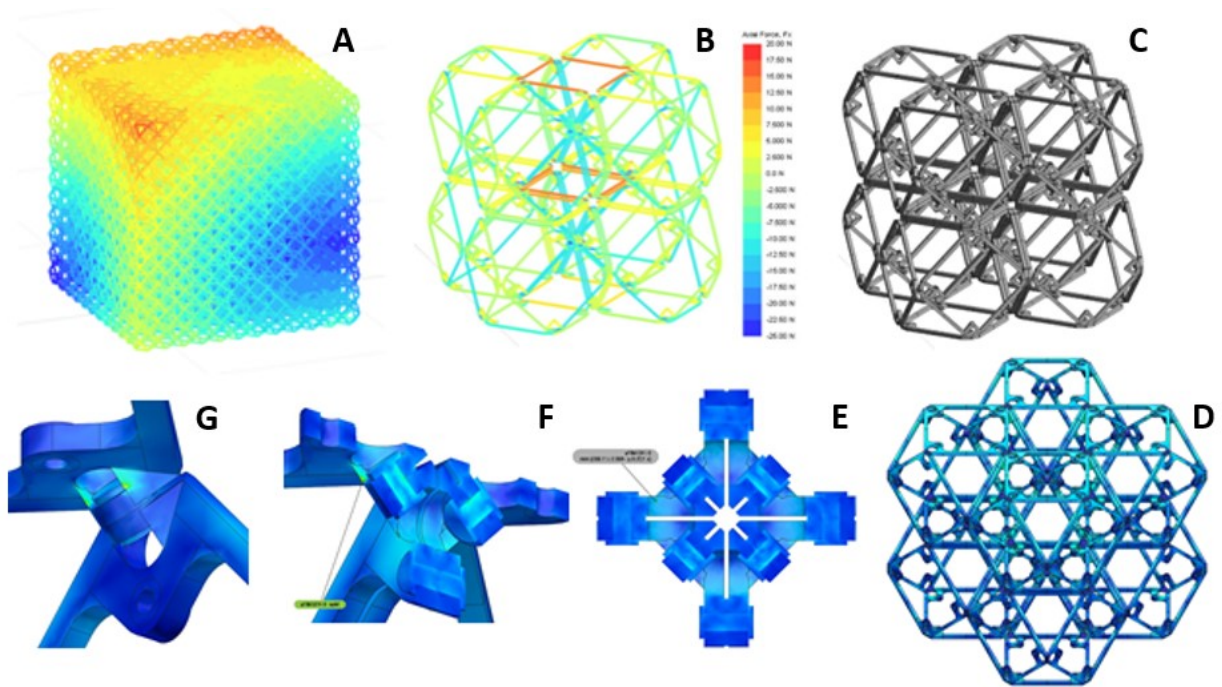
Figure 2-13: Numerical modeling at various scales. A) 10x10x10 analytical beam model, B) 2x2x2 detail beam model with axial stresses shown, C) unloaded model, D) 2x2x2 detail mesh FEA model, E) Section view of joint, F) Section and closeup view of voxel to voxel joint, G) stress concentrations visible at non-filleted edges.
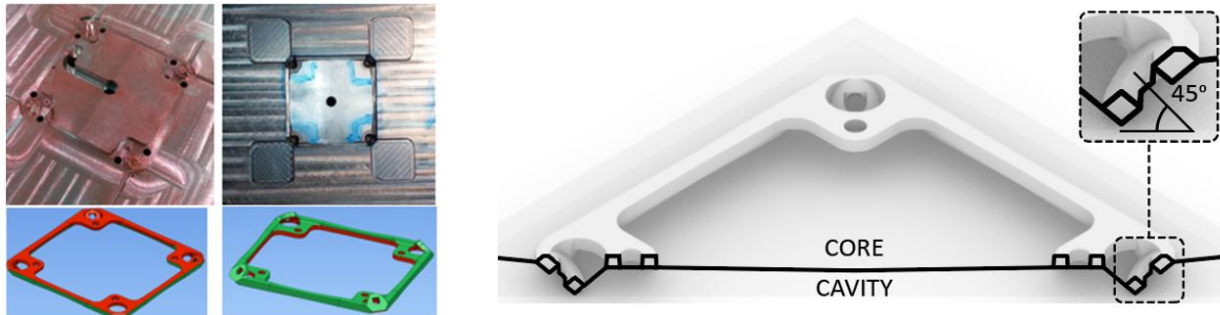
Figure 2-14: Injection molding details. Two part mold, with cavity below and core above, and a detailed view of the 45 degree angle hole, which is achieved by splitting the feature between core and cavity
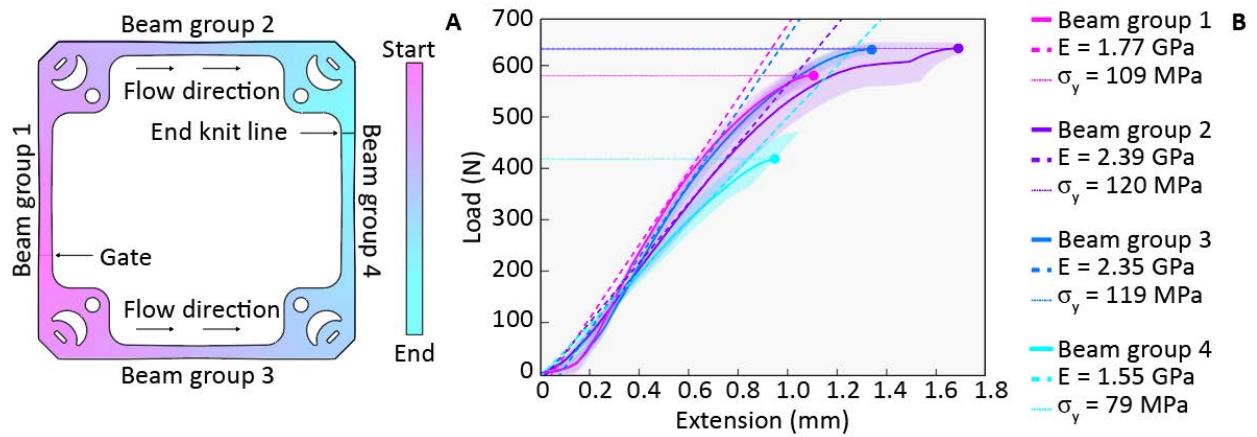
Figure 2-15: Molding parameters and resulting part properties. A) Injection molding gate layout and resulting material flow and knit line location, B) Characterization of different beam groups based on relative locations on part.

Fasteners

Given a huge variety of fasteners, here i'm showing some we've used including nuts and bolts, flexural clips, rivets, and custom made androgynous interlocking parts being developed at NASA. As long as they meet the stiffness and strength criteria as determined earlier, they should work. It's just a question of a) mass, and b) installation. Nuts and bolts are very mass efficient, but very fussy to install. Clips can be installed with just a translational degree of freedom. Andogynous fasteners can be customized to interface with robots For this work I'm using a 3/32" diameter aluminum blind rivets. They're installed with a variety of riveting tools, my current favorite is a pneumatic rivet gun. There are several benefits to using rivets: they're cheap, they're efficient, they're one sided, and there's a whole industry that supplies rivet installation tools for aerospace.
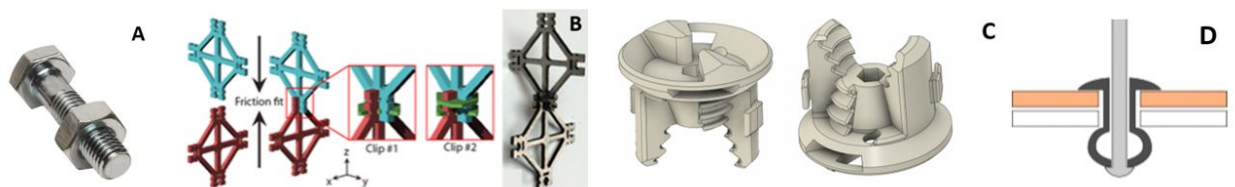
Figure 2-16: Mechanical fasteners for voxel assembly. A) Steel nut and bolt [53], B) Press fit and shear clip [57], C) Custom androgynous interlocking fastener for robotic assembly [58], D) Blind aluminum pop rivet, used in this work.

Assembly

Face parts are jointed at their corners with 3/32" diameter aluminum blind pop rivets. They are assembled one at a time, to form a cuboct voxel, as shown in Figure 2-17A. Voxels are then joined to neighboring voxels at their face-connection locations, using the same fasteners. To access this, a long-reach pop rivet gun is inserted through the opposite face as shown in Figure 2-17B. The face-connection nodes of this opposite face force the gun to come in at a slight angle, but the rivet actuation is successful.

Individual voxels have 12 corner joints, and a single voxel takes approximately 90-120 seconds to assemble. On average, once assembled a given voxel then has four rivets per face, which gives 24 rivets total, half of which are attributed to neighboring voxels. Thus, a single voxel has on average 12 face connections associated with its assembly time. Based on this and timed assembly exercises, I estimate the average voxel assembly time to be 4.5 minutes. Total assembly times are presented in Table 1. Future research will investigate automating these processes.
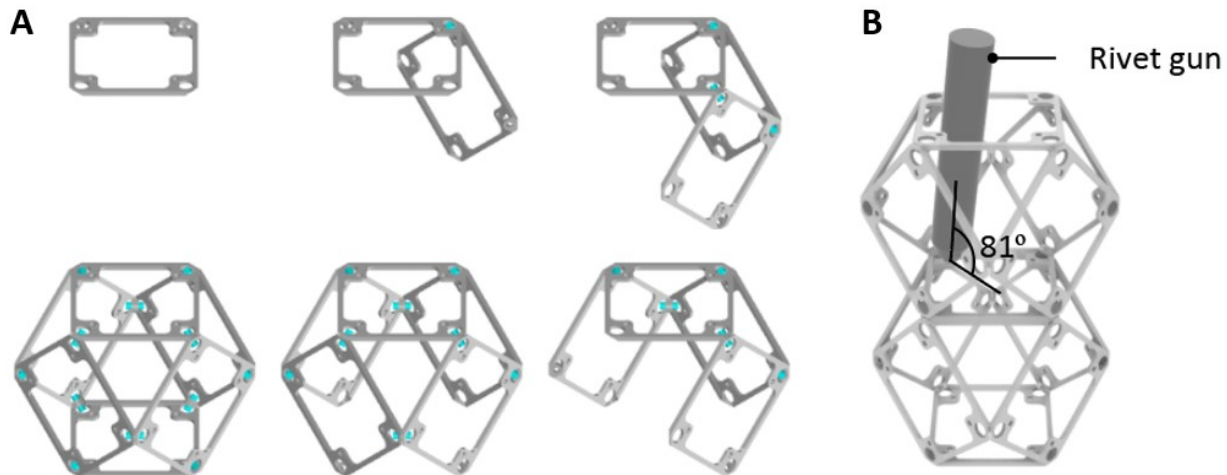
Figure 2-17: Voxel and lattice assembly. A) Voxel assembly sequence. Faces are joined together one at a time, using rivets at the corners. A voxel consists of six faces and twelve rivets. B) Neighboring voxels are joined with the same method, rivet gun shown entering opposite face, at slight angle due to interference with inter-voxel joint node of entering face.

Table 1: Lattice assembly metrics

Specimen cube voxel width n	Total voxels	Total Rivets	Avg rivets/voxel	Time/ voxel (min)	Total time (min)	cm³/hr	g/hr
1	1	12	12	1.5	1.5	16,876	500
2	8	144	18	2.25	18	11,250	333
3	27	540	20	2.5	67.5	10,125	300
4	64	1344	21	2.625	168	9,643	285
5*	125	2700	21.6	2.7	337.5	9,375	277
10*	1000	22800	22.8	2.85	2850	8,882	263
$N*$	N^3	$N^3*12 + [N^2*(3(N-1))]*4$	24	3	$3*N^3$	8,440	250

* = projected (not built), Avg Rivet time = 7.5s, Voxel mass = 12.5g, Voxel vol = 422 cm³

2.2.7 Subsystem characterization

Following as-molded material characterization to calibrate analytical and numerical models, subsystems are then characterized in tests designed to isolate the critical performance aspects for proper system behavior. Rivets, inter-voxel nodes, individual voxels (consisting of beams and inner-voxel joints), and multi-voxel assemblies were tested. The specific goal is to quantify the degree to which voxel and multi-voxel behavior is governed by stiffness and strength properties of the beams, rather than the joints. Experimental results are shown in Figure 2-18, with axial stiffness and critical load values noted.

Since each subsystem effectively acts across the same cross section (a single voxel), we can directly compare their yield strength using their observed failure loads. We see the intervoxel node and fastener yield strengths are roughly two and four times the voxel yield strength, respectively. For axial stiffness, we treat single and multi-voxel tests as effective springs in series. A single voxel then consists of five effective springs in series: top fasteners, top nodes, voxel, bottom nodes, and bottom fasteners. For springs in series, the equivalent axial stiffness is the reciprocal of the sum of the individual spring reciprocals:

$$\frac{1}{k_{eq}} = \sum_{i=1}^{n} \frac{1}{k_i}$$

$$k_1 \ll k_{i>1}$$

$$k_{eq} \approx k_1$$

For large k_i and small k_1, we see that k_{eq} equals k_1, indicating that the governing value is the lower spring stiffness. Using measured values for fasteners, nodes, and voxels, we see the experimental value for the two-voxel assembly agrees with this analytical description, and that both effective stiffness and strength are governed by voxel, and thus beam, properties. This construction system is then used to design a family of part types with a range of mechanical metamaterial properties.
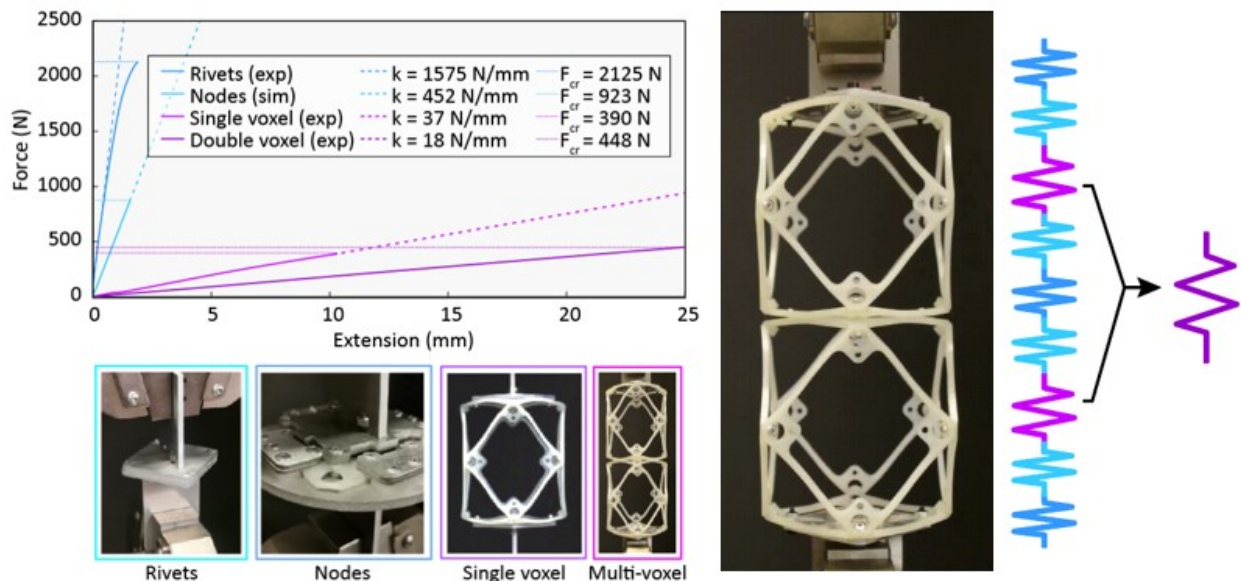
Figure 2-18: Experimental results for subsystem characterization, where we see joints (rivets + nodes) are individually stiffer and stronger than voxels, which are governed by beam properties.

2.3 Mechanical Metamaterial Part Types

Here I present the discretely assembled mechanical metamaterial system consisting of four part types: rigid, compliant, auxetic, and chiral, shown in Figure 2-20. Six face parts (Figure 2-20A) are assembled to form voxels (Figure 2-20B), which are then assembled to form multi-voxel lattices (Figure 2-20C). The four lattice types and their behaviors will be described in further detail in the following subsections.

Rigid voxels resolve external loading through axial beam tension and compression, resulting in elastic, followed by plastic, buckling of struts. Lattice made with these parts shows near-linear density scaling of effective elastic modulus. Prior art includes hierarchical, ultra-light, ultra-stiff lattice [33], composite assembled and epoxied lattice [59], and new lattice topologies for improved isotropy [55].

Compliant voxels are designed with corrugated flexure beams, a motif found in flexural motion systems [60], which resolve axial beam forces through elastic deformation of the planar flexures. Lattice made with these parts show consistent elastomeric behavior at even single voxel resolution and have a near-zero Poisson ratio. Prior art includes lattices made from elastomeric material for extreme strain [38] and rationally designed flexural internal architectures for macroscopic material mechanisms with directional compliance [37].

Auxetic voxels are designed as intersecting planes of re-entrant mechanisms, which expand and contract laterally under uniaxial tension and compression, respectively, producing an effective negative Poisson's ratio. Prior art includes re-entrant foams pioneered by Roderic Lakes [23], 2D programmable auxetic structures [61], and sinusoidal curved-beam networks with auxetic behavior [62]

Chiral voxels are designed with an asymmetric mechanism which responds to in plane loading by producing either clockwise (CW) or counterclockwise (CCW) rotation. When interconnected in three dimensions, this produces out of plane twist in response to uniaxial tension or compression. Prior art includes 3D chiral metamaterials using cells with internal handedness [41] and chiral 2D plates for twisting wing tips [63].
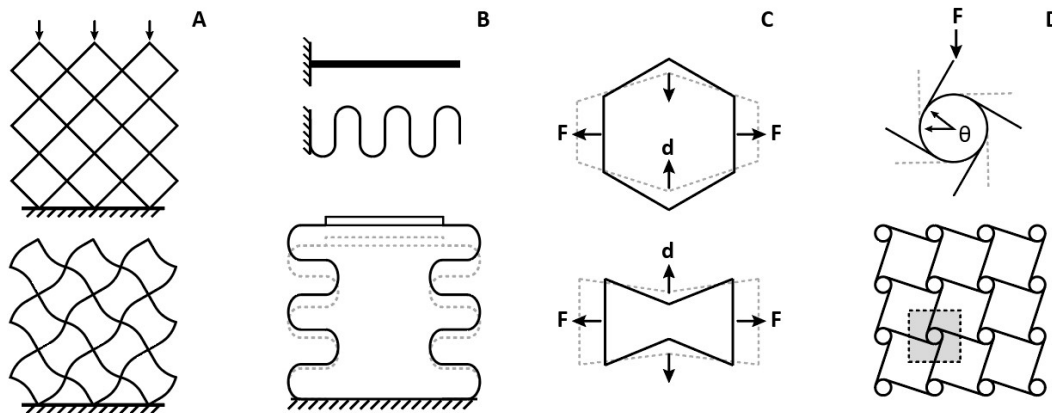
Figure 2-19: Overview of metamaterial mechanisms. A) Rigid, B) Compliant, C) Auxetic, D) Chiral.
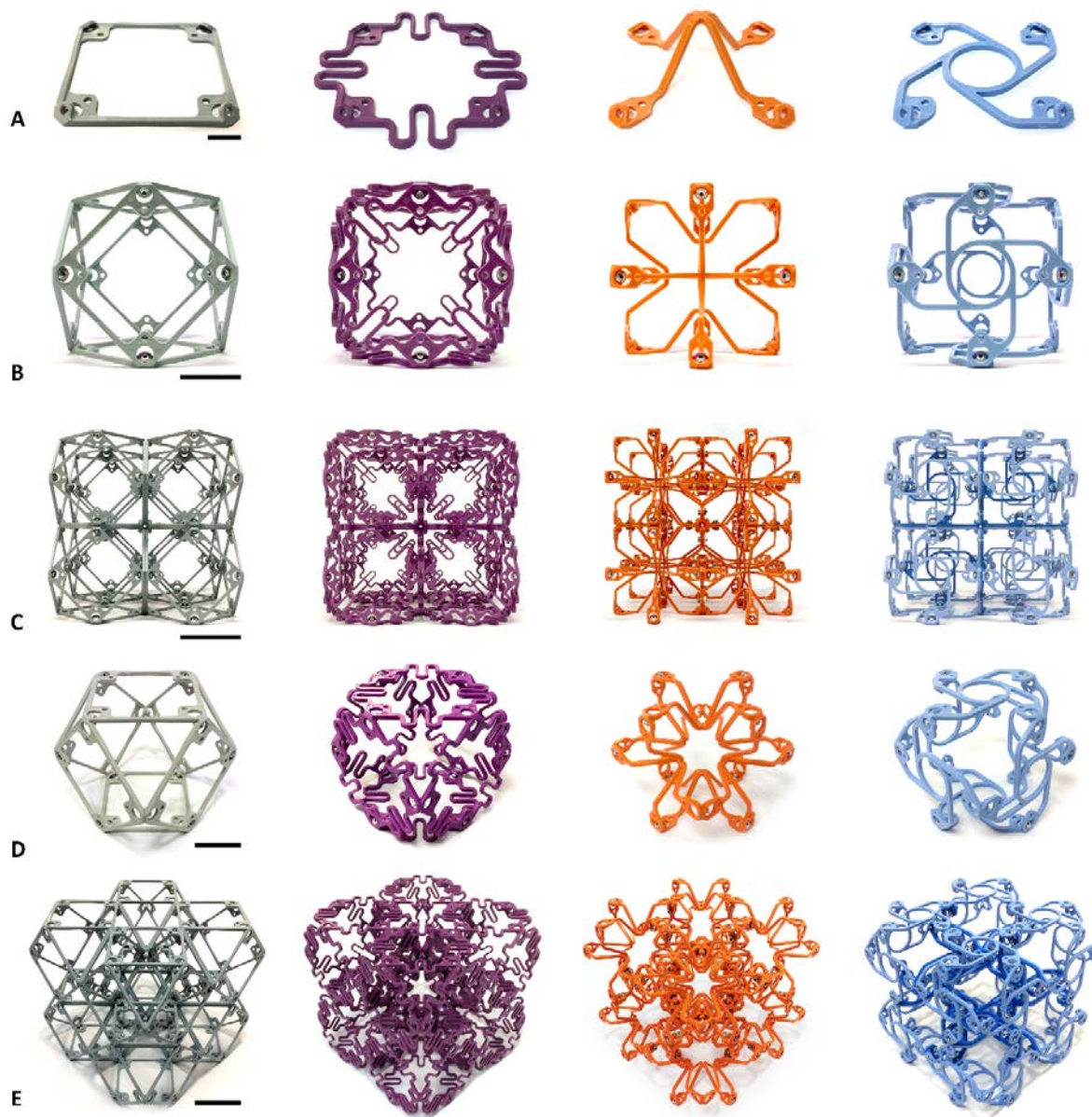
Figure 2-20: Four types of discretely assembled mechanical metamaterials, left to right: rigid, compliant, auxetic, and chiral. A) As-molded face parts, B) Single voxel, front view, C) 2x2x2 Cube, front view, D) Single voxel, oblique view, E) 2x2x2 oblique view. Scale bars: A) 10mm, B, D) 25mm, C, E) 50mm.

2.3.1 Rigid Lattice

The rigid lattice type exhibits modulus-density scaling which matches previous results in literature but does so with a novel geometric decomposition. The characteristic behavior of a unit cell voxel is shown in Figure 2-22. The geometry is isotropic along its primary axes, and it responds to loads through axial beam tension and compression. While individual voxels are dominated by under-constrained, mechanism behavior of the quadrilateral faces, when multiple voxels are joined, there is sufficient connectivity to provide rigidity through triangulation of neighboring voxel faces. Effective modulus increases with increasing cell count, eventually reaching an effective continuum value, as seen in Figure 2-24B.

Having established that the global behavior is governed by the beam properties, now I can correlate analytical models with experimental results for effective lattice behavior. Here I will look at effective elastic modulus E* and yield strength σ, the former corresponding to the linear portion of the stress strain curve under quasi-static loading, and the latter corresponding to the failure load divided by the specimen cross section area. Stress-strain curves for lattice specimens of cube side voxel count n = 1-4 are shown in Figure 2-23, where an initial linear elastic regime is followed by a non-linear elastic regime and plastic yield. Using load and displacement data, stress and strain values are calculated based on lattice specimen size. The calculated moduli are shown with numerical results in Figure 2-24. It can be seen that as voxel count n increases, E* approaches a continuum value depending on the beam thickness, and thus relative density of the lattice. Numerically, I investigate the effect of increasing beam thickness t as a function of lattice pitch P and plot the resulting curves in Figure 2-24.

These predicted effective lattice properties over the range of effective densities are plotted relative to constituent values in Figure 2-30A. The slope of the curve connecting these points, plotted on a log/log chart, provides the power scaling value, which is used to analytically predict lattice behaviors at the macroscopic scale [26]. Effective modulus and density are related to constituent modulus and density by $E^*/E = k(\rho^*/\rho)^a$, where a is 1 for stretch dominated lattices and 2 for bending dominated. I find a = 1.01 for our rigid lattice. This scaling value had been shown previously for the monolithic (additively manufactured) cuboctahedron lattice [55] and for discretely assembled, vertex connected octahedra [53], to which I now add this novel lattice decomposition.

Next, I compare experimental yield stress results with analytical predictions of local beam failure based on relative density, as a function of beam thickness t and lattice pitch P. Here, I will use experimental data from the 4x4x4 specimen, as this is closest to demonstrating continuum behavior. Based on the load at failure and lattice geometry, I can determine a given beam compressive failure load to be 88N. I determine the analytical critical beam load using either the Euler buckling formula or the Johnson parabola limit, depending on the compression member's slenderness ratio (Figure 2-11) I determine our beam slenderness ratio to be 29.5, which is over the critical slenderness ratio of 19.7, thus I use Euler buckling formula. Because the as-molded material properties vary, I determine the critical load to range from 70 to 108 N, with the mean value of 89 N very closely approximating the experimental value.
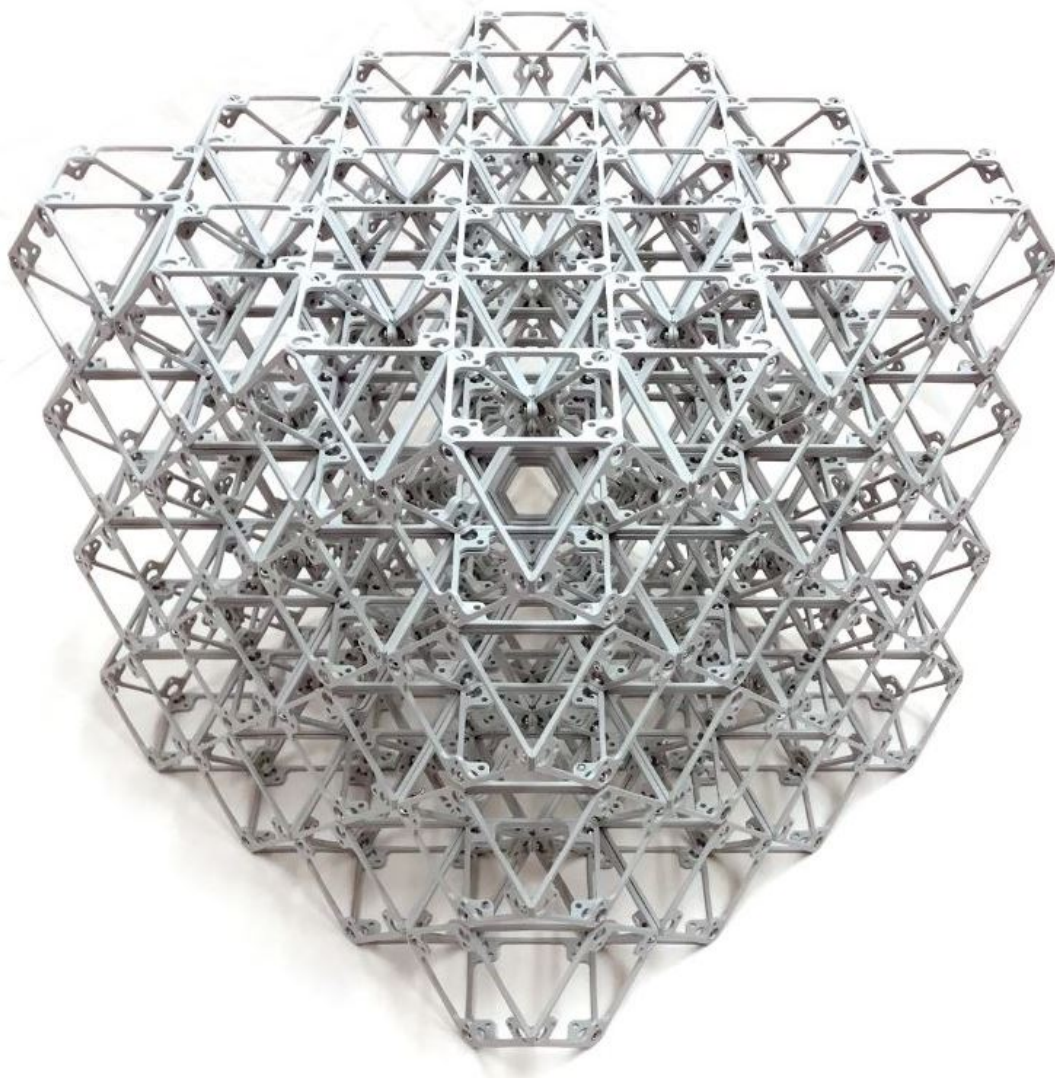
Figure 2-21: Rigid lattice. (Top) Built 4x4x4 voxel cube, (bottom) single voxel and face part.
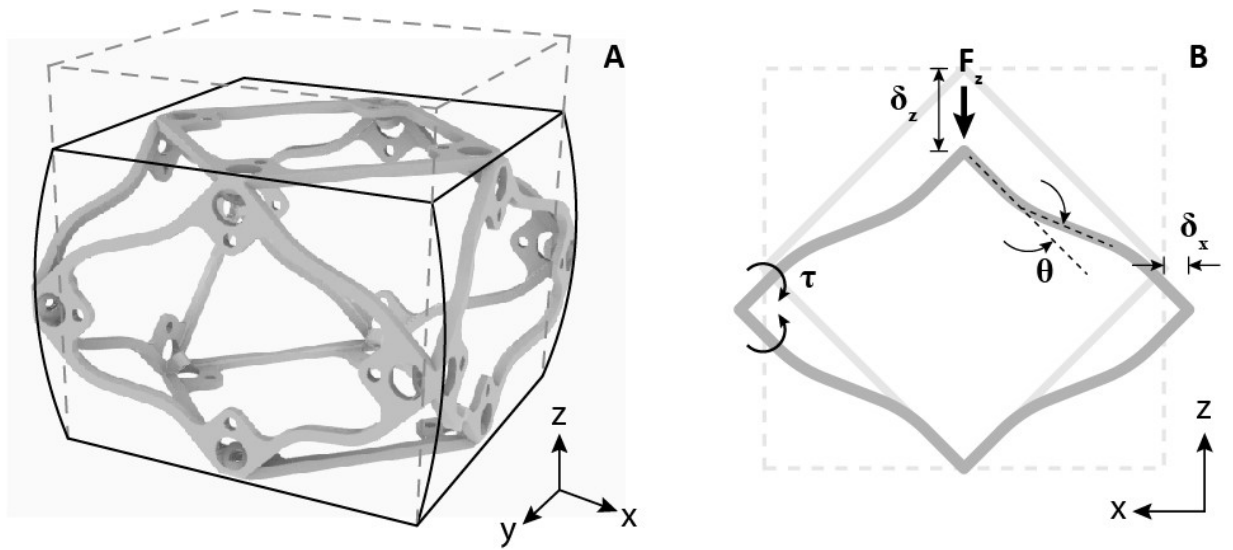
Figure 2-22: Rigid lattice voxel. A) Characteristic unit cell voxel demonstrating beam buckling and positive transverse strain in response to compressive load, B) in plane FBD of face part.
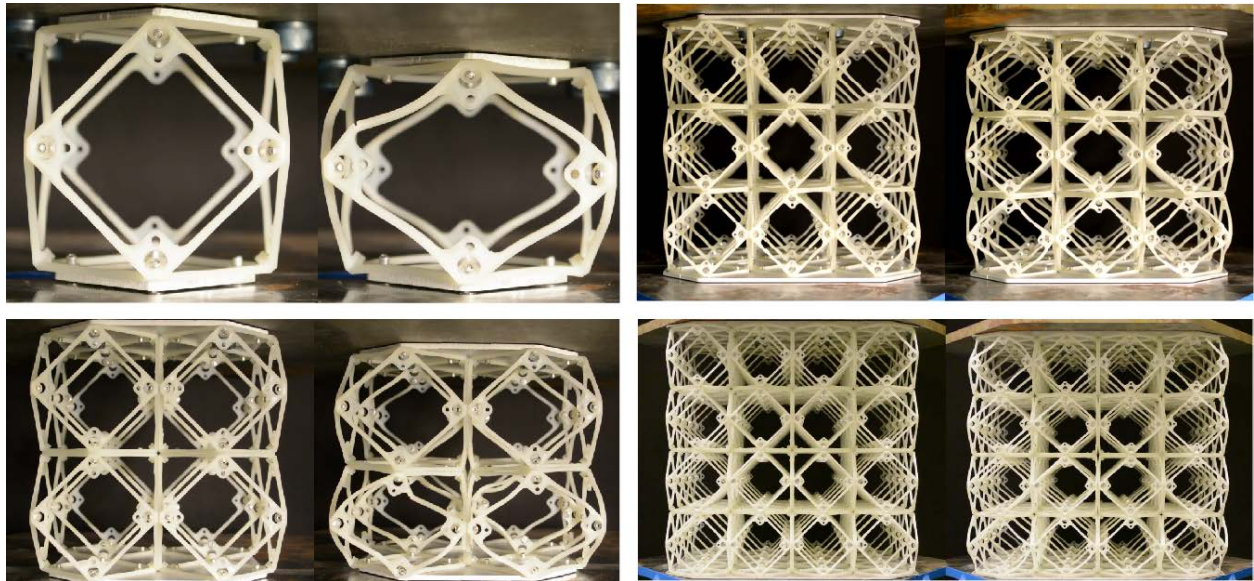
Figure 2-23: Rigid lattice testing. Experimental test setup for n = 1-4, showing undeformed, and deformed shape at initial beam failure.
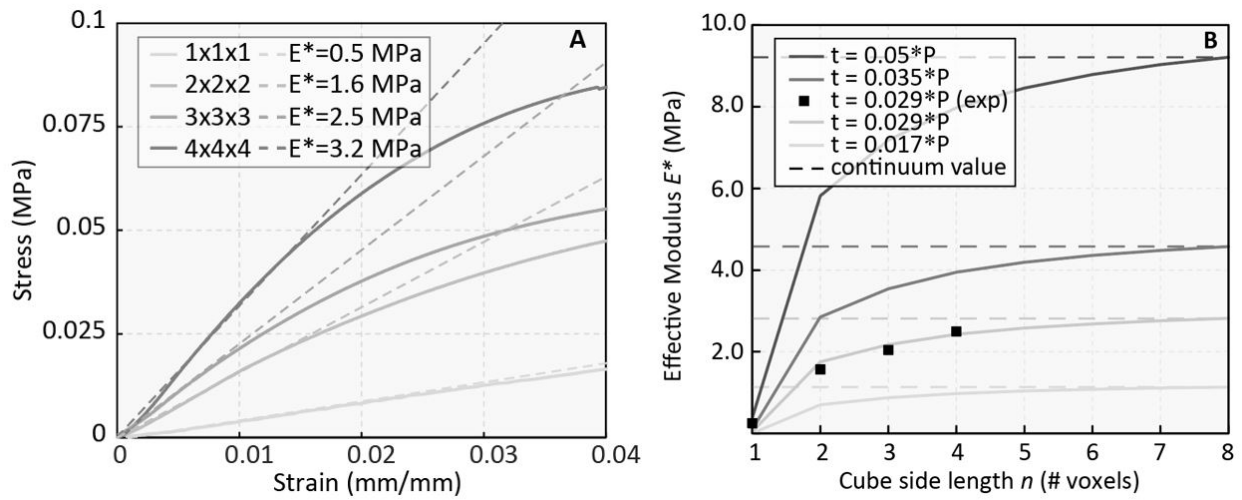
Figure 2-24: Rigid lattice testing results. A) Compression testing results, B) Effective stiffness simulation and experimental results demonstrating continuum behavior at increasing voxel count.
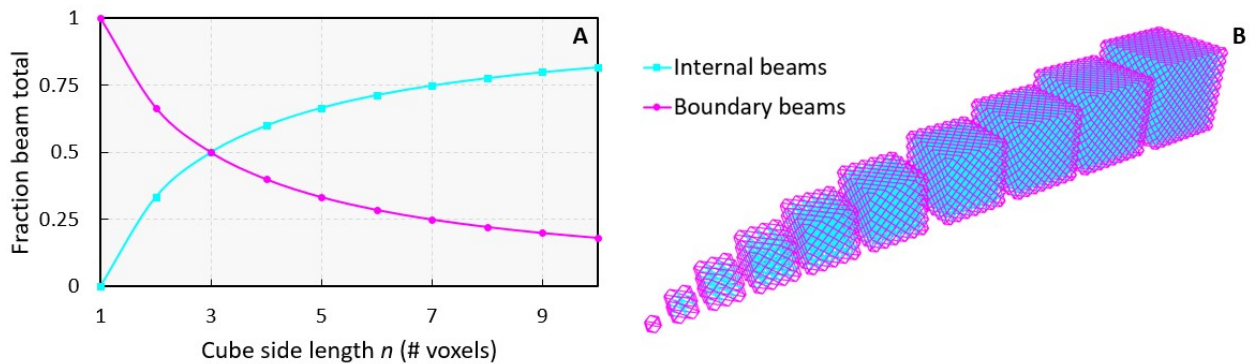
Figure 2-25: Effect of boundary conditions as a function of cell count. A) In this plot of cube side length versus fraction of total beams for internal and boundary beams, we see an interesting crossover at n = 3, which suggests this should be the minimum lattice size to ensure global behavior is not governed by boundary conditions. B) View of cubes from n = 1 to n = 10, with color codes for internal and boundary beams.

2.3.2 Compliant Lattice

The compliant lattice type exhibit quadratic scaling for effective stiffness, as well as consistency across voxel counts regarding continuum behavior and elastic limit values. We present experimental and numerical results for the compliant lattice type in Figure 2-29. The characteristic behavior of a unit cell voxel is shown in Figure 2-27. While the load paths are topologically the same as the rigid voxel, as this is a function of lattice connectivity, the mechanism through which beams resolve these loads is different. Here, the planar-spring beams deform in combined axial and in-plane bending, as a controllable property of the compliant features we design. This produces several unique properties in this lattice type.

First, we can see from the experimental stress-strain curves that for similar strains, the compliant lattice shows linear elastic behavior, up until the elastic limit (Figure 2-29). The stress at which this transition occurs is consistent across voxel counts, from n = 1 to n = 4. Second, the effective modulus is also consistent across voxel counts. This is confirmed by simulations. Given the large range of linear to non-linear and individual to continuum behavior seen in the rigid lattice, the compliant lattice is markedly different in its consistency. This behavior is attributable to the spring-like behavior of the beams, a similar observation to analytical models for stochastic foams (30). As cube specimen side length voxel count increases, so do the number of springs acting in parallel, which produces an effective spring stiffness. But as spring count increases, so does effective area, both proportional to side length squared. Thus, a single voxel has the same effective modulus as a 4x4x4 or an n x n x n cube. This effect is reduced as beam-spring amplitude a goes to zero, meaning it approaches behavior similar to the rigid cuboct lattice.

Another property observed experimentally, and confirmed numerically, is a low, near-zero, Poisson's ratio. Figure 2-30B shows the simulated effective Poisson's ratios for the compliant and rigid voxel. At the largest compliant amplitude, we see a value of near zero. As the amplitude a of the compliant spring feature goes to zero, the Poisson's ratio converges to around 0.15, which is the effective value for the entire parameter range of the rigid lattice.

Finally, this lattice shows near quadratic stiffness scaling, in contrast to the near linear scaling shown by the rigid lattice, while having the same base lattice topology and connectivity as the rigid version (Figure 2-30A)—meaning it has bending-dominated behavior with a stretch dominated lattice geometry. This is attributable to the localized behavior of the spring-like beams. Whereas in the rigid lattice vertically oriented beams in compression are offset by horizontally oriented beams in tension, resulting in stretch dominated behavior, here global strain is a function of local spring-beam strain, which does not produce significant reactions at beam ends opposite an external load. This behavior gradually changes as we approach a = 0.05 but is clearly after the experimental data at a = 0.075.
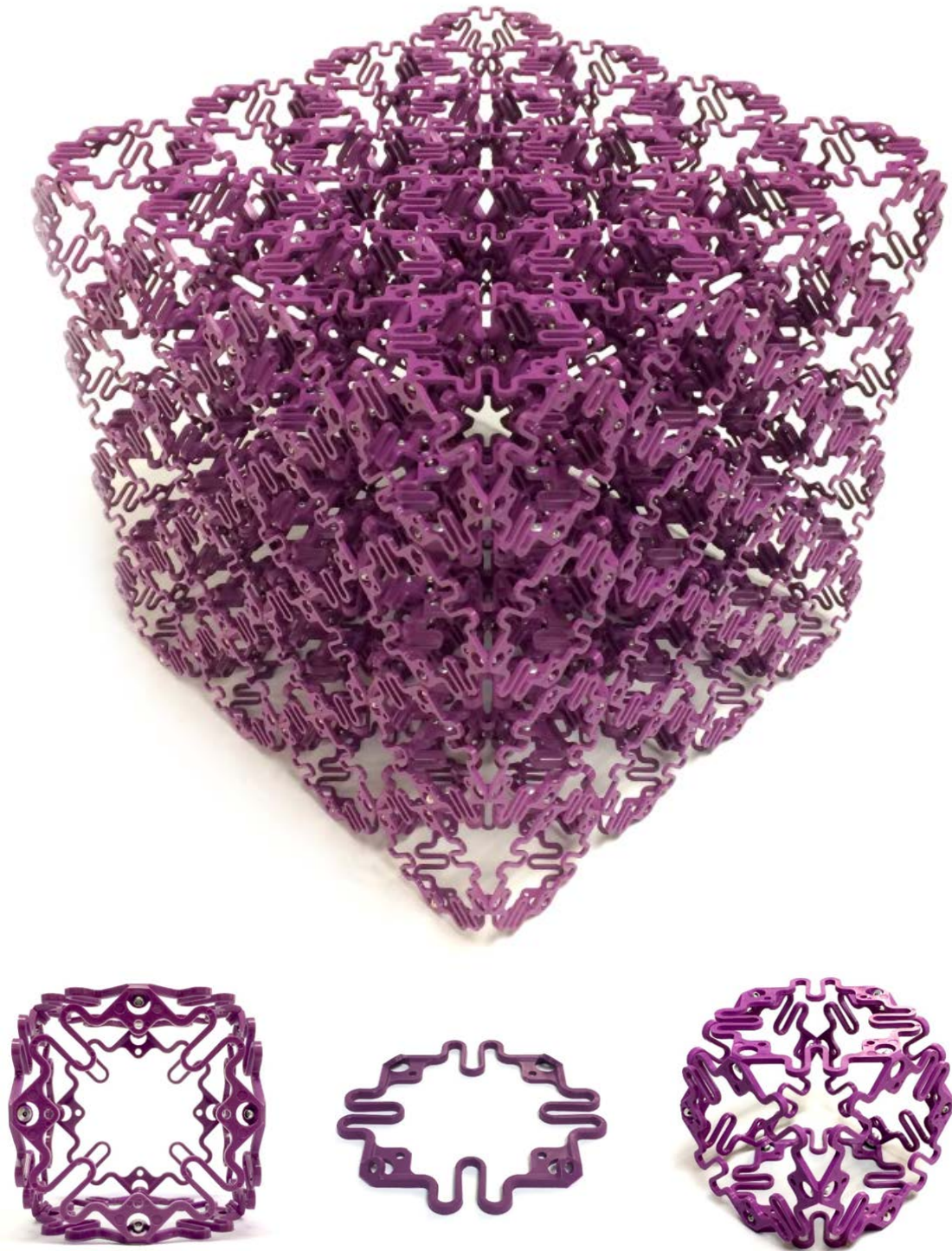
Figure 2-26: Compliant lattice. (Top) Built 4x4x4 voxel cube, (bottom) single voxel and face part.
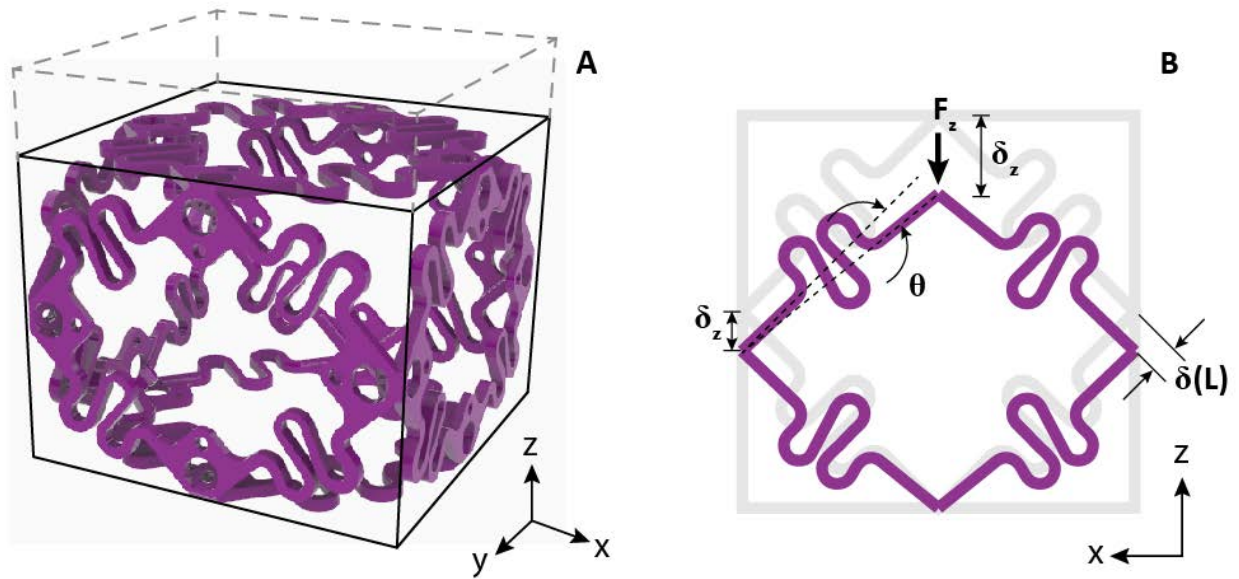
Figure 2-27: Compliant lattice voxel. A) Characteristic unit cell voxel demonstrating flexure spring-beam deformation and small transverse strain in response to compressive load.
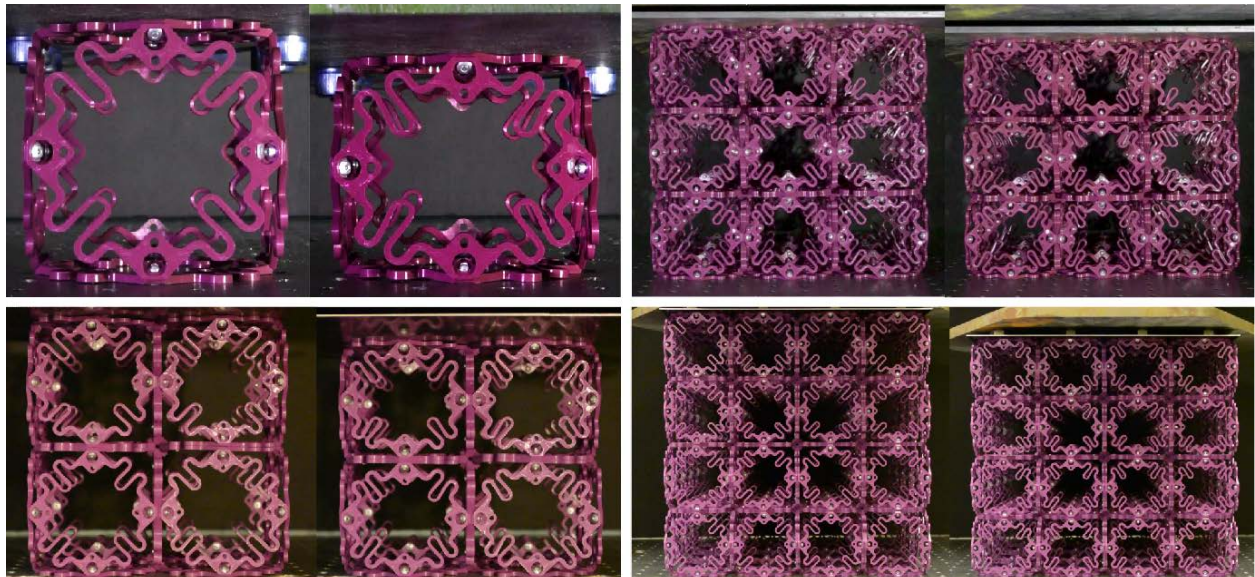
Figure 2-28: Compliant lattice testing. Experimental test setup for n = 1-4, undeformed and deformation at the onset of non-linearity.
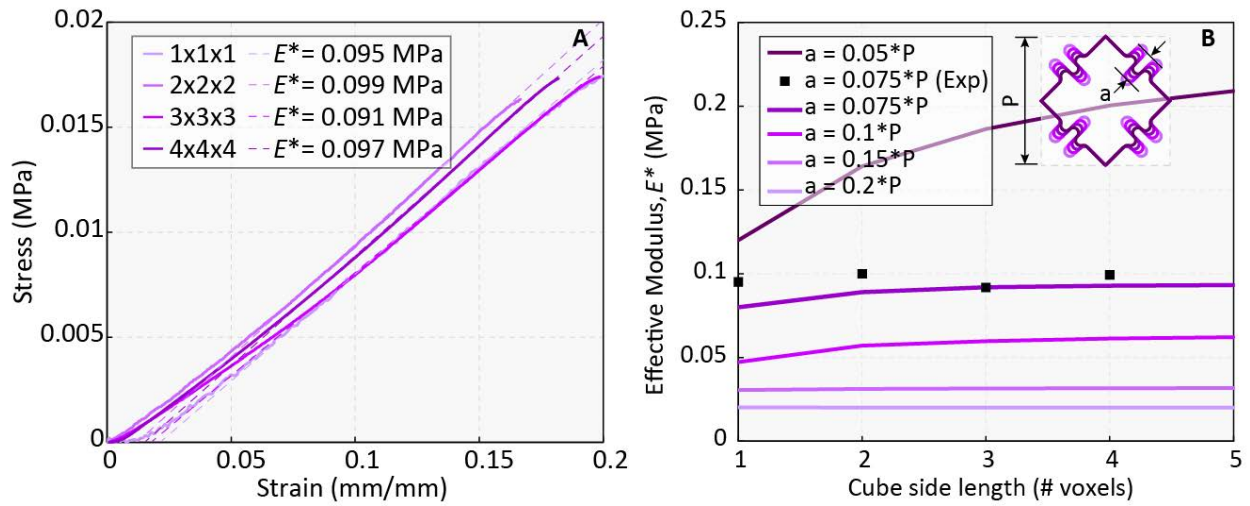
Figure 2-29: Compliant lattice testing results. A) Compression testing results, B) Effective stiffness simulation and experimental results, which show near continuum value at low voxel count for all but the smallest spring-beam amplitude designs.
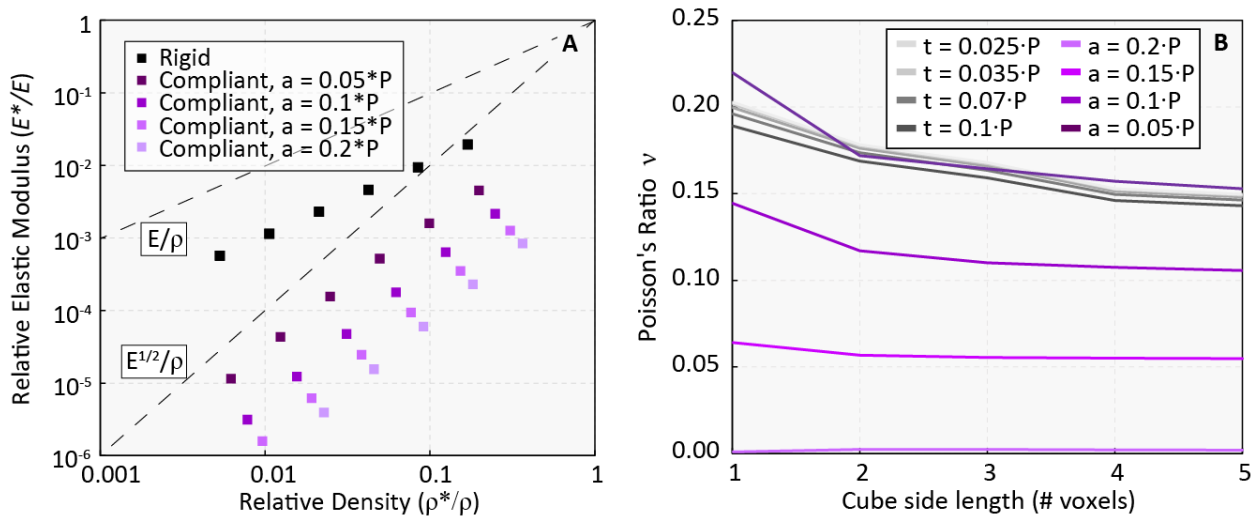
Figure 2-30: Comparison of effective properties for rigid and compliant lattice. A) Simulation results for modulus-density scaling value for rigid and compliant lattice, which are linear and quadratic, respectively. B) Simulation results for effective Poisson's ratio for rigid and compliant lattice, with large spring-beam amplitudes having a value of near zero.

2.3.3 Auxetic Lattice

The goal of the auxetic lattice type is to exhibit a controllable negative Poisson's ratio. I present experimental and numerical results for the auxetic lattice type in Figures 2-34 and 2-35. The characteristic behavior of a unit cell voxel is shown in Figure 2-32. Due to the internal architecture, which consists of interconnected, re-entrant mechanisms seen elsewhere in literature (14), the cell responds to axial strain with a similarly signed transverse strain, resulting in a negative Poisson's ratio $\nu = -\epsilon_{trans}/\epsilon_{axial}$. This value can be controlled based on the re-entrant distance d as a function of lattice pitch P, as shown in Figure 2-34B.

Experimental results are shown in Figure 2-34A. Lattice specimens are cubes of voxel width n = 1-4. Specimens were compressed to identical axial strain values of 0.2, and transverse strain was measured by visually tracking points using fiducials mounted to the nodes along transverse faces (yz plane) parallel to the camera. These results are slightly obscured due to reduced reentrant behavior at the edges of the lattice. In Figure 2-34B, we show contour plots element translation in the y direction, which is out of plane and normal to the camera view. While this behavior is generally isotropic, it should be noted that the effect of the internal mechanisms is reduced at the corners/edges of the cube specimen, as shown in Figure 2-35. This effect is taken into account when calculating the effective strain values which are plotted in Figure 2-34B, over the range of parameters shown.

There are two main insights from this study. First is that the effective metamaterial behavior approaches a nominal continuum value as cube side length of voxel count n increases. For any re-entrant distance, this behavior can be attributed to the increase of internal mechanism architecture relative to boundary conditions. Boundary conditions increase as a function of surface area proportional to n^2, while internal mechanism architecture increases as a function of specimen volume proportional to n^3. For lower values of d, the single voxel demonstrates lower values for Poisson's ratio (increased auxetic behavior) compared to multi-voxel specimens, but this is strongly influenced by boundary conditions, and is considered an outlier.

The second insight is that the effective Poisson's ratio decreases (becomes more negative) as re-entrant distance d is increased, for voxel specimens larger than n = 1. This can be understood by considering the continuous beams of the re-entrant faces as a pseudo rigid body model (PRBM), where continuous flexural mechanisms are discretized as effectively rigid links connected by planar joints with torsional stiffness (ie: a spring) (31). As d decreases, so does link length, causing less clearly defined boundaries between the rigid link and compliant spring joint (see supplementary material for further analysis). As a result, the rigid link behavior begins to dominate, causing higher overall effective stiffness and lower compliance, thus reducing the re-entrant mechanism efficacy. Further description of this behavior can be found in supplementary material.
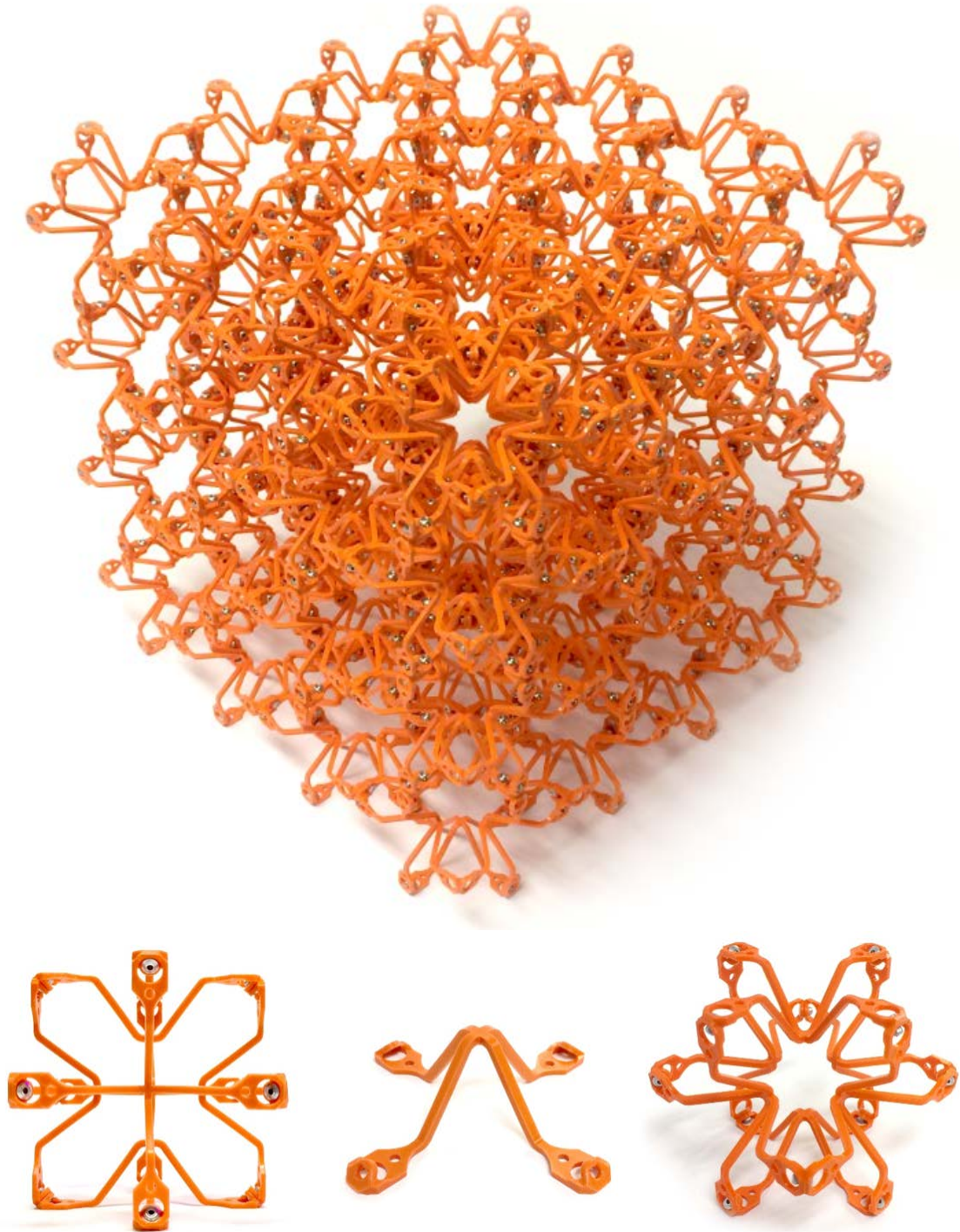
Figure 2-31: Auxetic lattice. (Top) Built 4x4x4 voxel cube, (bottom) single voxel and face part.
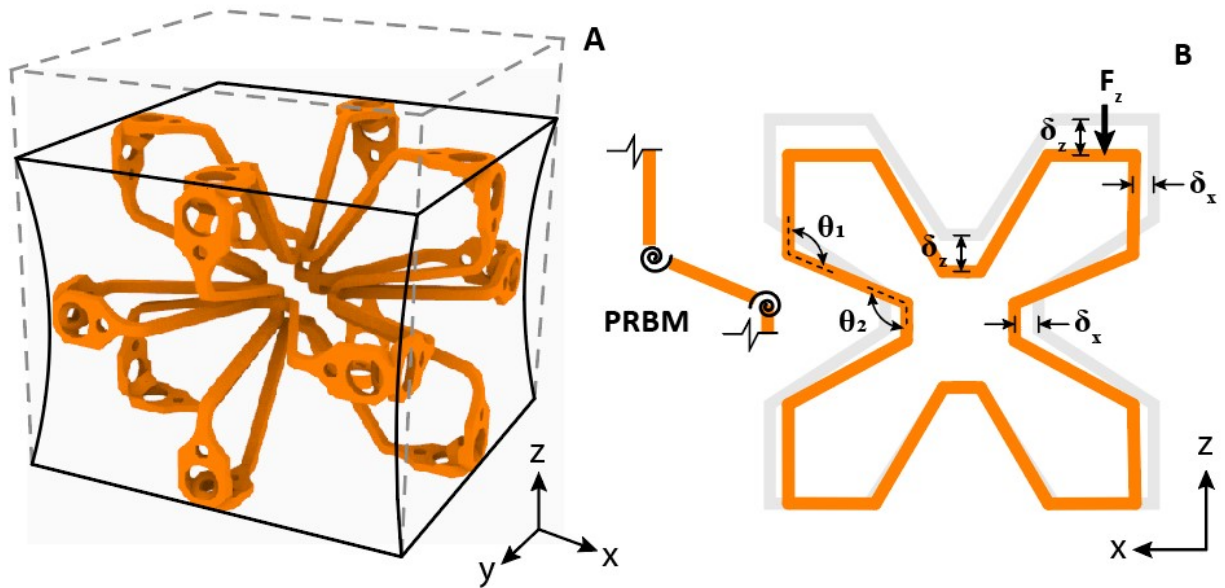
Figure 2-32: Auxetic lattice voxel. A) Characteristic unit cell voxel demonstrating reentrant mechanism action resulting in negative transverse strain in response to compressive load, B) in plane FBD of middle section of voxel (note: this consists of portions of four face parts).
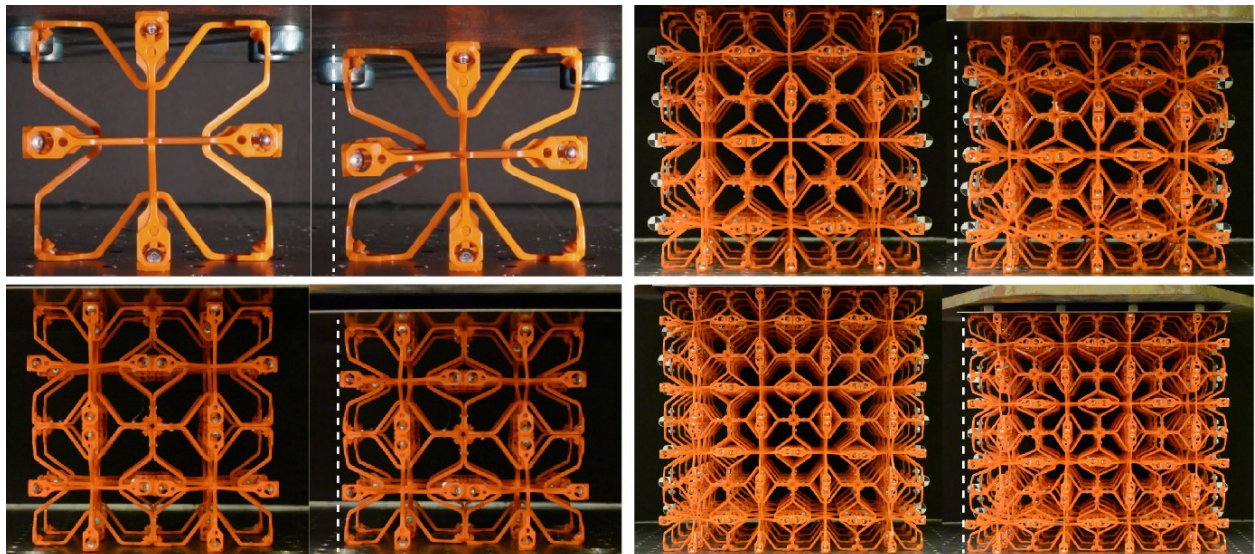
Figure 2-33: Auxetic lattice testing. Experimental test setup for n = 1-4, undeformed, and deformed to 0.2 strain , with partial out of plane auxetic behavior visible.
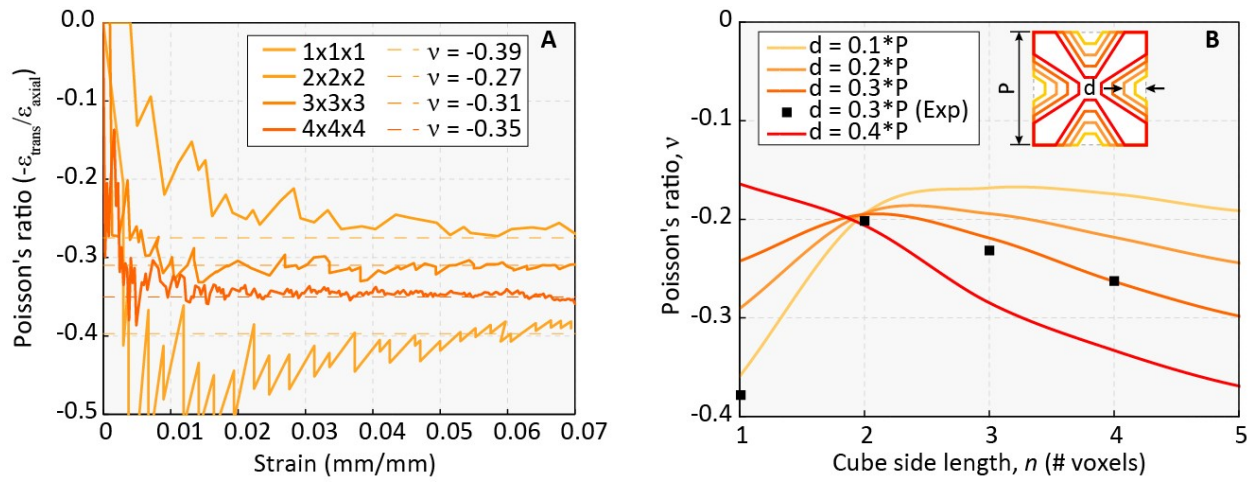
Figure 2-34: Auxetic lattice testing results. A) Raw data, B) Experimental and simulation results compared.
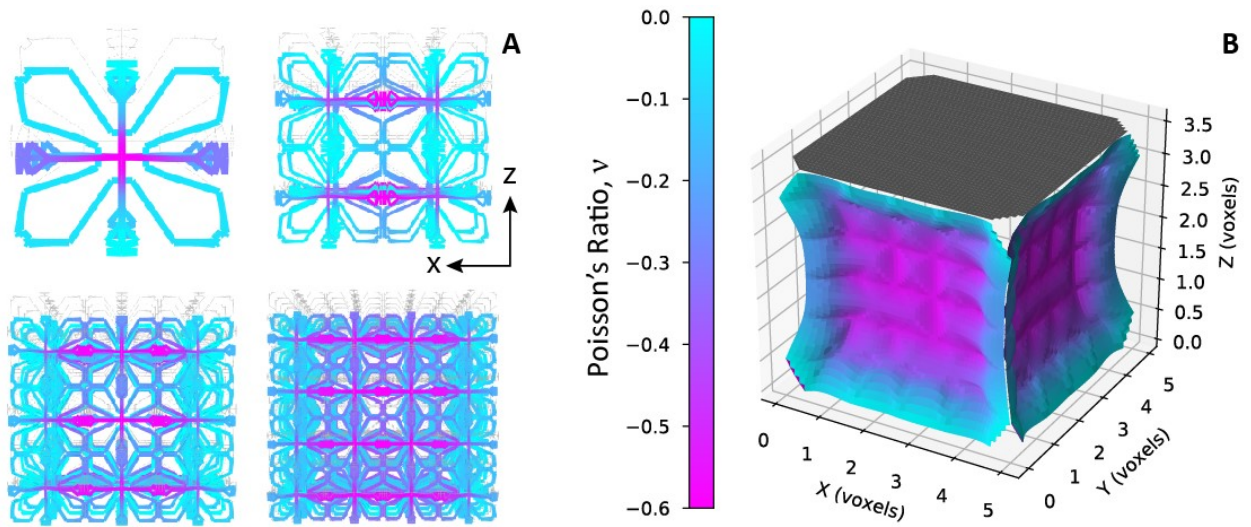
Figure 2-35: Auxetic lattice boundary condition study. 3D contour plot demonstrating effect of boundary conditions resulting in near zero Poisson's ratio at edges.

2.3.4 Chiral Lattice

The chiral lattice type exhibits scalable twisting behavior, which is attributable to having two chiral part types, and developing a construction logic to avoid internal frustrations. I present experimental and numerical results for the chiral lattice type in the following section. The characteristic behavior of a unit cell voxel is shown in Figure 2-37. Based on the chirality orientation, the cell will respond to an axial strain with a macroscopic twisting in either the CW or CCW direction, in the plane normal to the direction of loading (ie: loading in z direction results in twisting in xy plane). The effective chirality can be measured as degrees twist per unit strain.

Experimental results are shown next to their numerical simulations in Figure 2-39. Lattice specimens are designed as columns with 1:4 width to height ratio, similar to (15). The top half is CCW chiral lattice and the bottom half is CW chiral lattice. This produces the largest net twist at the rigid interface between the two halves and allows fixed boundary conditions at the top and bottom. Chiral columns of 1x1x4, 2x2x8, and 3x3x12 were tested in compression to identical axial strain values of 0.05, and twist was measured by tracking a single point at the center of the lattice. Experimental results are shown in Figure 2-39A. Surprisingly, the 1x1x4 shows larger values for twist than the 2x2x8. This is attributable to internal architecture, which is also the cause of the scalable twisting found over a range of beam sizes.

There are several key takeaways from this. First, we see that performance does not decrease monotonically with increasing voxel count n, but rather stabilizes to a continuum value. This is in contrast to comparable results in literature (15), and can be explained by looking more closely at the combination of CW and CCW part types. Done properly, internal frustrations—when CW and CCW faces are joined they essentially cancel each other's twist, resulting in zero twist per strain—can be avoided, as shown in (32) by using voids. In our case, we get improved twist performance by logically designing the internal architecture according to rules chosen to avoid frustration. This means that voxel types are directionally anisotropic, in contrast to the previous three lattice types, and further are spatially programmed to produce desired global effective behavior. Strategies for this spatial programming are shown in Figure 2-38. On the left, we show a beam with odd number voxel widths. Here, design rule 1 is to orient the net face chirality (represented as arrows) away from the column interior. The experimental lattices for n=1 and n=3 widths were built using rule 1. Design rule 2 was developed starting from n=2, where the orientation of interior faces is ambiguous when following rule 1. Rule 2 introduces continuous, clockwise circumferential orientation of the interior chiral faces and was used in construction the n=2 experimental articles. Both rules are hierarchical, e.g. a rule 1 5x5 column contains a 3x3 and 1x1 column in its interior as shown. Simulations were performed for all column widths using both rules and show decreased twist response for rule 2, in agreement with experimental measurements. These rules were determined empirically and are not considered exhaustive but indicate the importance of rational design in this lattice type.
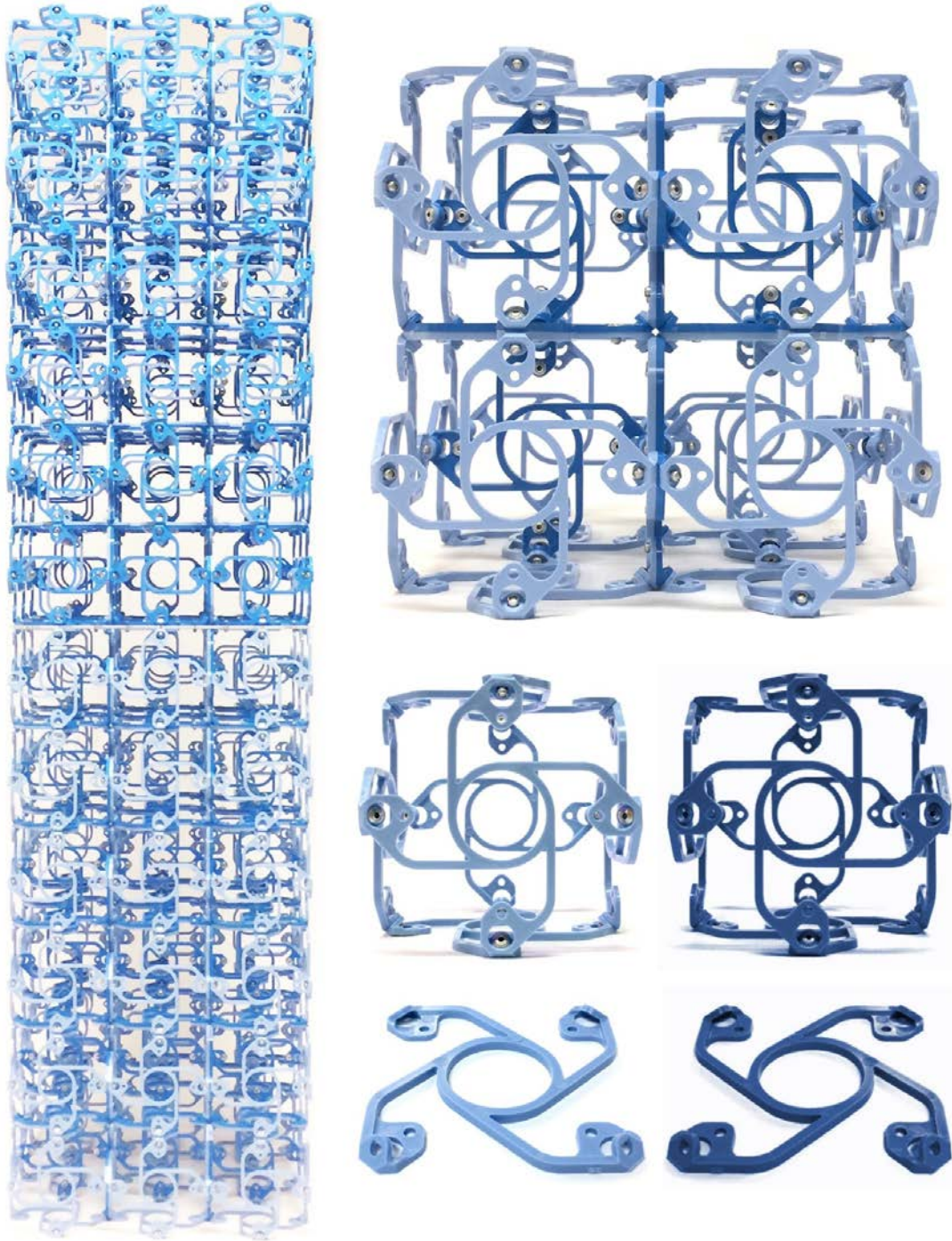
Figure 2-36: Chiral lattice type. (Left) 3x3x12 chiral column, (Right) 2x2x2 cube showing internal architecture of CCW (light blue) and CW (dark blue) parts with programmed spatial distribution
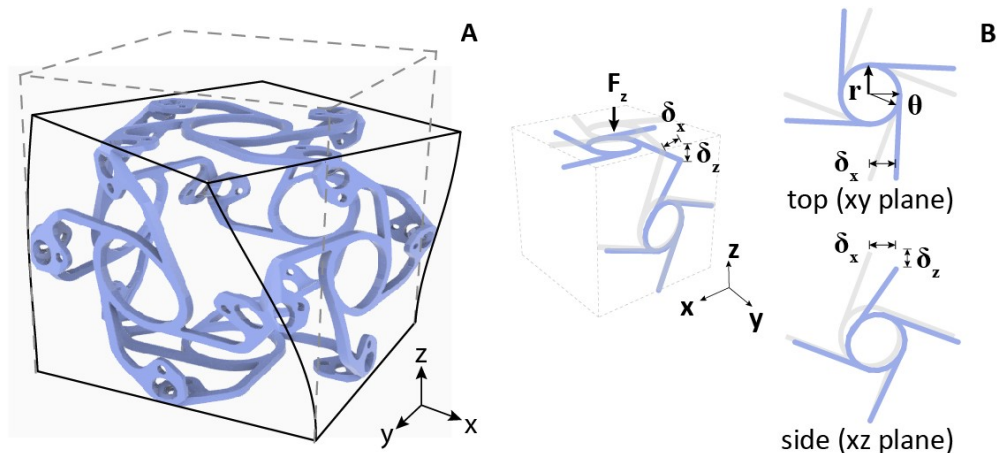
Figure 2-37: Chiral lattice voxel. A) Characteristic unit cell voxel demonstrating out of plane coordinated rotation in response to compressive load. B) FBD of deformation mechanisms.
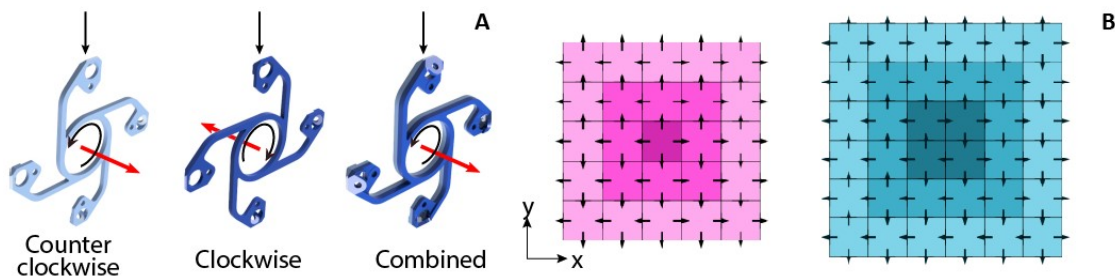
Figure 2-38: Chiral design rules. A) Two chiral part types allow internal frustration to be avoided, thus enabling scalable chiral architecture, B) Design rules 1 (L) and 2 (R), which emerge from odd and even columns, respectively.
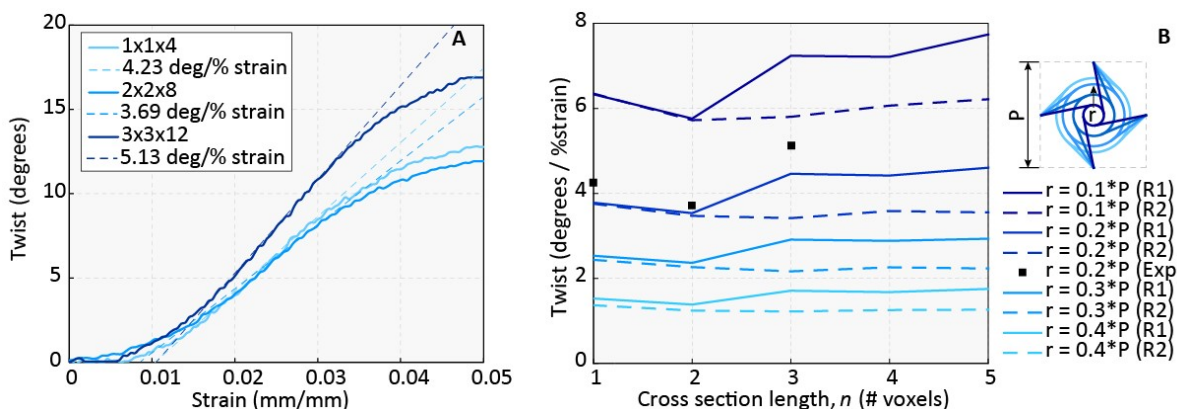
Figure 2-39: Chiral testing : Experimental and simulation results of n = 1, 2, and 3, showing total twist increases as column voxel width increases, but normalized twist per strain is lower for n = 2.
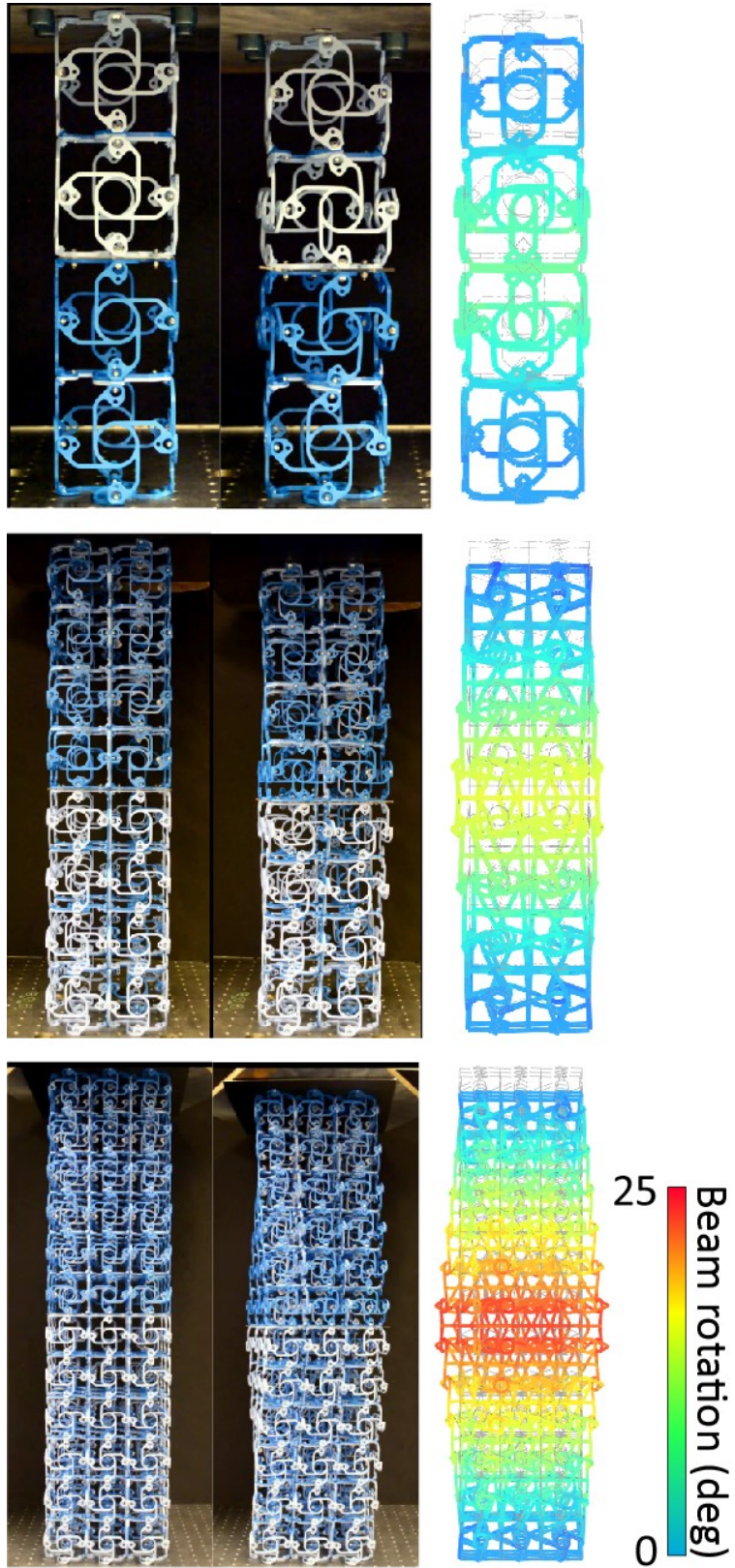
Figure 2-40: Chiral testing : Experimental results (left) and simulations (right).

2.3.5 Discussion

I successfully demonstrated that it is possible to discretely assemble several types of mechanical metamaterials. Each type demonstrated near-continuum behavior, and the resulting lattices have strong parallels to prior art in the metamaterial body of research. These are typically seen at the micrometer scale (Figure 2-41), but this work enables them to be realized at the centimeter to meter scale—an increase of 10^3, without the associated cost of scaling up a machine several orders of magnitude to 3D print them.
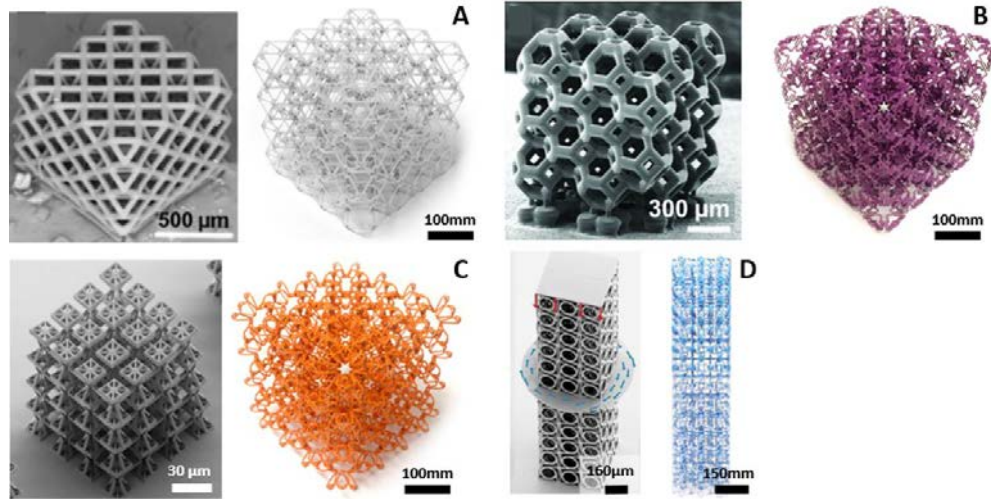
Figure 2-41: Comparison of microlattice to discretely assembled lattice, where we see a factor of 1000 scale increase. A) Rigid [55], B) Compliant [33], C) Auxetic [68], D) Chiral [41].

The scale of our system was originally driven by an application (see Section 4.2). A 75mm lattice pitch was deemed appropriate in terms of spatial resolution (the higher the better) and number of parts (the fewer the better). But a 75mm unit cell is quite large compared to the majority of published lattice metamaterials, which typically have micrometer scale beam elements composing centimeter scale parts. One argument in favor of discrete assembly is the practicality: for tooling on the order of 10^3 USD and parts on the order of 10^2 USD, with commercially available fasteners and tools summing 10^2 USD, one can build large-scale mechanical metamaterials with no additional overhead. But if one wanted higher spatial resolution with a smaller unit cell, how well would the system presented here scale down? Here we can look at two critical aspects: part manufacturing and part joining.

Commercially available injection molding specifies minimum wall thickness of around 0.5mm, with some more specialized micro-molding services offering as thin as 0.15mm [69]. Our parts have beam thickness of 2.5mm, so just looking at isometrically scaling the part down (which is sub-optimal, but useful for this exercise), we can get a part size shrink of 5x with typical commercial molding. Micro-molding can potentially provide up to x16 shrink, but for now, we will use a x10 shrink factor, to give 0.25mm thick beams. So, while the cost model may become less favorable, micro-molding can produce lattice parts with 7.5mm pitch (Figure 2-42).
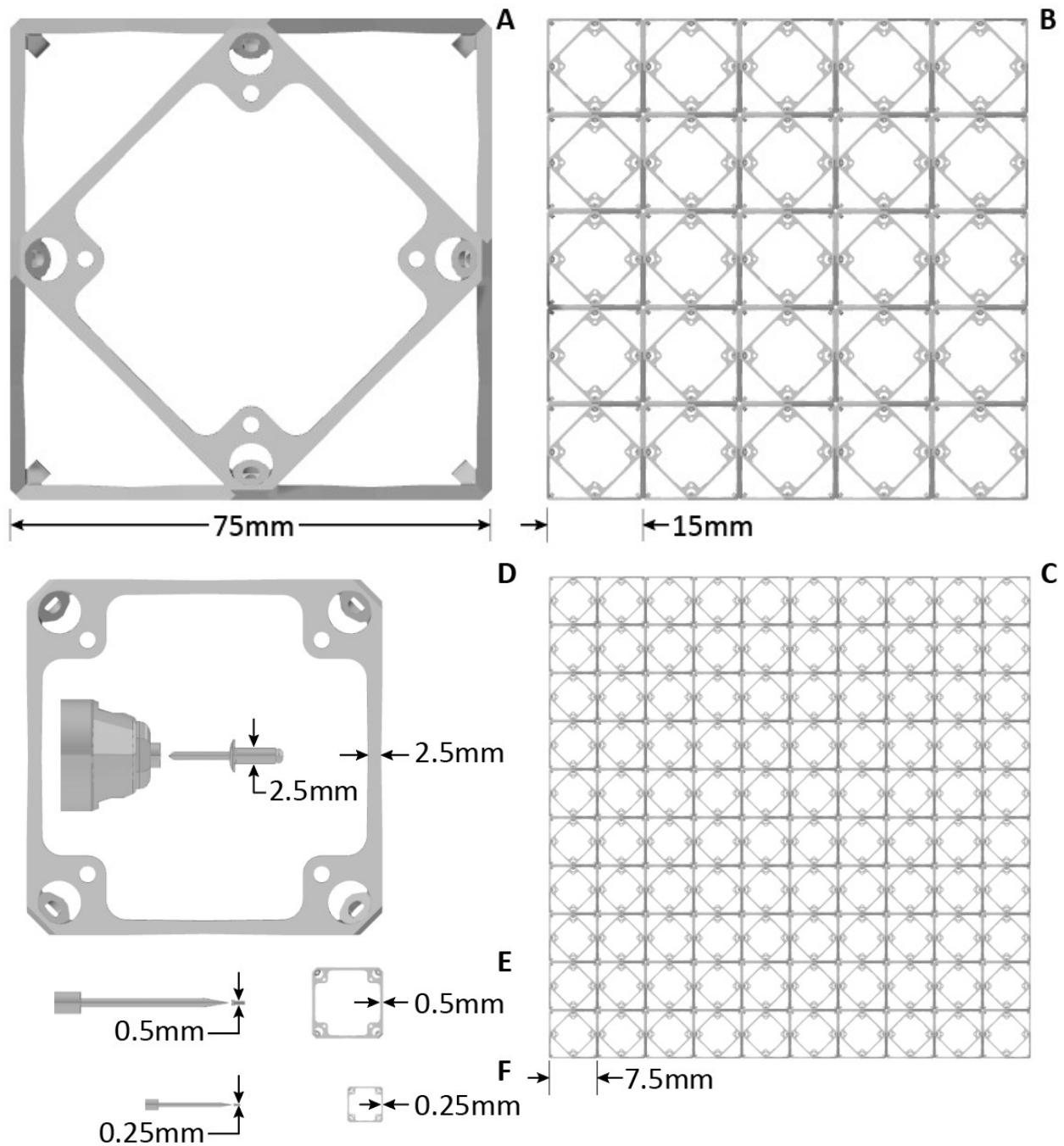
Figure 2-42: Voxel scaling study (shown at actual scale). A) Current voxel with 75mm pitch, B) 5x shrink (1/5 original size) with 15mm pitch, C) x10 shrink (1/10 original size) with 7.5mm pitch, D) 75mm pitch face part with 2.5mm beam thickness and 2.5mm diameter rivet with rivet tool, E) 15mm pitch face part with 0.5mm beam thickness and 0.5mm diameter fastener (screwdriver shown for reference), F) 7.5mm pitch face part with 0.25mm beam thickness and 0.25mm diameter fastener with scaled screwdriver for reference.

With low cost, this metamaterial construction kit can still achieve spatial complexity. In Section 4.4 I describe a heterogenous lattice using rigid and compliant parts. It is a simple 1D beam but demonstrates controllable anisotropy. For heterogeneous voxel-based metamaterials, the combinatorial possibilities scale exponentially with number of cells [44], and it has been theorized that with only these two part types, it is possible to realize any arbitrary elasticity tensor [70].

Of course, due to the high resolution, multi-material capabilities of polyjet-style 3D printers, nearly continuous gradients can be achieved between materials (all of which are photocurable polymers, but still offer at least an order of magnitude range of elastic modulus). For a discrete assembly system, it becomes a question of number of different parts and resulting degree of spatial programmability. In Figure 2-43, I show several studies on possible discrete graded heterogeneous lattices. In A), I show a beam starting as two part types, rigid and compliant, and adding gradual transitions between the two. The finer the step size, the more distinct part types there are. The face part themselves can also be heterogeneous, as shown in C), where I transition from rigid to compliant by adding compliant beams one at a time. This is anisotropic, but this could be leveraged to design specific deformation modes into a lattice, such as having compliant or rigid bands or stripes running throughout a given structure. Given the enormous potential of this topic, it will be explored further in future work.
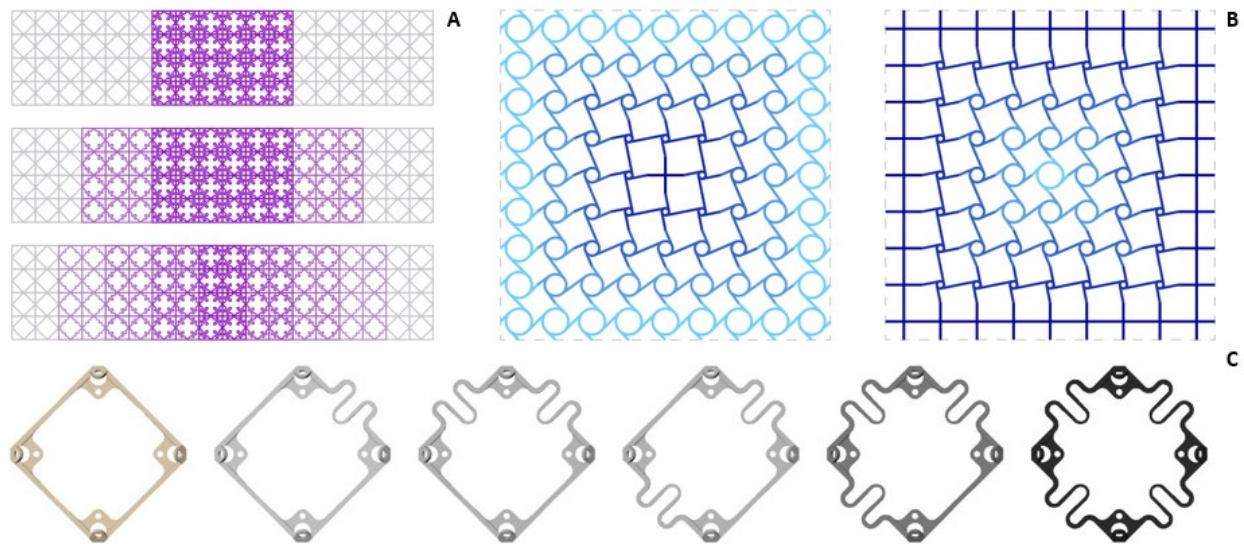
Figure 2-43: Graded heterogeneous discrete lattices. A) Compliant and rigid, with increasing gradation from top to bottom, B) Chiral to achiral by varying the diameter of the internal mechanism from D = P (lattice pitch) to D = 0, C) Heterogeneous part types allow inner-face architectural control.

We can compare discrete assembly to other lattice production methods, specifically, additive manufacturing processes such as selective laser melting (SLM), fused deposition modeling (FDM), polyjet (photopolymer), stereolithography (SLA), and large area projection microstereolithography. The results are shown in Table 2. The cost, scale, and throughput

60

rates of discrete assembly are competitive and in some cases better than state of the art additive, making this an appealing method for constructing large scale cellular structures.

Table 2: Comparison of additive manufacturing and discrete assembly

Manufacturing Method	Volume rate (cm³/hr)	Mass rate (g/hr)	Machine/ setup cost (USD)	Part scale
Selective laser melting (SLM) [71]	<170	<195	10^5-10^6	<1m
Fused deposition modeling (FDM) [72]	<60	<65	10^3-10^5	>1m
Polyjet (photopolymer)	<80	<95	10^4-10^5	<1m
Stereolithography (SLA)	<280	<340	10^4-10^5	<1m
Large area projection micro stereolithography (LAPµSL) [73]	1.2	1.4	>10^6	<<1m
Discrete assembly (this work)	≈5626	≈162	10^3	>1m

In this chapter, I presented a method for producing large scale mechanical metamaterials through discrete assembly of modular, mass-produced parts. I showed that bulk, continuum behavior can be achieved through design of the parts and connections, ensuring global behaviors are governed by local properties. I presented a finite set of part types which exhibit a diverse range of behaviors. Rigid lattice types show linear stiffness to density scaling with predictable failure modes. Compliant lattice types show quadratic stiffness to density scaling, as well as unique bulk behavior at low cell count, such as near-zero Poisson's ratio. Auxetic lattice types show controllable, isotropic negative Poisson's ratio. Chiral lattice types show scalable transverse twist in response to axial strain, which is a result of two part types being used to prevent internal architectural frustration. All four part types showed good agreement with numerical results, and their behavior is predictable through analytical means. All lattice types are made the same way: parts are injection molded and assembled with blind rivets to make voxels, and voxels are similarly joined to build lattice. This is a low cost, highly repeatable process that promises to enable mechanical metamaterials at macro scales.

By offering a simple yet diverse set of parts unified with a consistent assembly method, this work represents a significant step in lowing the barrier for entry to realizing the promise of metamaterials. Combined with hierarchical design tools and assembly automation, this research can enable emerging fields such as soft robotics, responsive aero and hydrodynamic structures, and user-defined programmable materials, thereby further merging the digital and physical sides of future engineering systems.

Chapter 3

Assembly Automation

3.1 Background

Here I will review the state of the art for digital fabrication in terms of processes (continuous vs. discrete) and platform mobility (stationary vs. mobile). Within each group, I will discuss relevant metrics such as performance (ie: throughput, precision), scale, and cost/complexity, specifically as they pertain to the production of useful structural parts and systems. I will end by describing a relatively unoccupied part of parameter space, that of a material-robot system.

Continuous Processes

A reasonable question to ask is why not just 3D print macro-scale cellular structures? In demanding applications, parts made with layer-based deposition processes can suffer from undesirable anisotropy [74], as well as being susceptible to stochastic error inherent to continuous material [75]. For risk-averse applications, such as 3D printed rocket parts, time and labor intensive non-destructive inspection, such as ultrasonic imaging [76], is required. While continuous material deposition techniques used in additive manufacturing offer promising complexity and efficiency at small scales, performance degrades as you scale up, with both motion control and deposition granularity becoming coarser. For these reasons, large structures made this way face significant hurdles in adoption to mass-production or high performance applications—the risk of failure is still too great.

Nearly all of the previously mechanical metamaterials are made with some form of additive manufacturing, most of which are summarized in [19]. These processes vary widely in terms of cost, precision, throughput, and material compatibility. The lower end of the cost spectrum, such as fused deposition modeling (FDM), also tends to have lower performance. Limits of thermoplastic extrusion include layer-based anisotropy [74] and errors resulting from build angles for complex 3D geometry [77]. Higher performance, and higher cost, processes such as selective laser melting (SLM) utilize materials such as stainless steel, but require non-trivial setup for particulate containment, and can suffer from layer-based anisotropy, thermal warping, and geometry irregularity [78]. Some of the highest performance

multi-scale metal microlattice production techniques based on lithographic and plating processes are well-studied and repeatable but are also highly specialized and labor-, time-, and cost-intensive. Polymerization, curing, plating, milling, and etching can require up to 24 hours from start to finish for sample preparation [28]. Large area projection microstereolithography is capable of producing lattices with micrometer scale features on centimeter scale parts [34] with significantly improved throughput, but extension to macro-scale (>1m) structures remains out of reach, due to practical limitations in scaling these processes and their associated machines. Given the finite precision of affordable digital control systems, these larger scale platforms inevitably tradeoff some precision for scale. In response to this, several mobile robotic approaches seek to extend the boundaries of continuous deposition processes. LiDAR directed, multi-DoF arms with rolling bases can coordinate on cementitious deposition within a given sensing range [79], while a foam-depositing arm mounted to a mobile crane has a large workspace [80], though relocation for extensible construction has not been demonstrated.
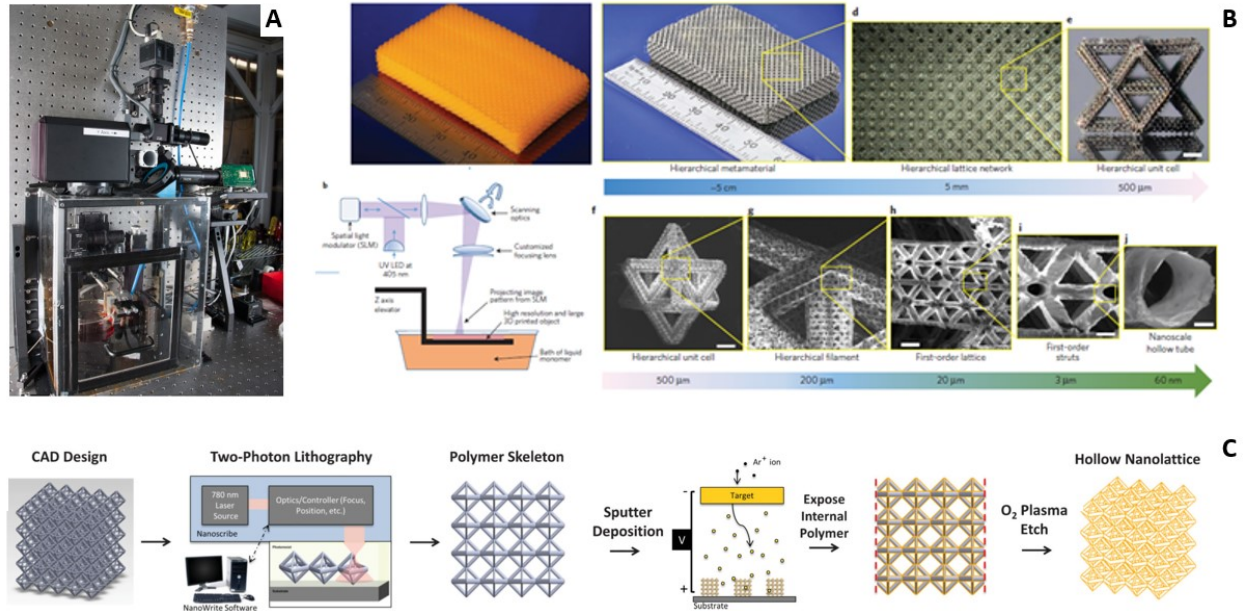
Figure 3-1: Small scale stationary platform for continuous deposition. Large area projection micro stereolithography machine [73], B) Hierarchical lattice made with LAPuSL [81], metal lattice manufacturing process [82].
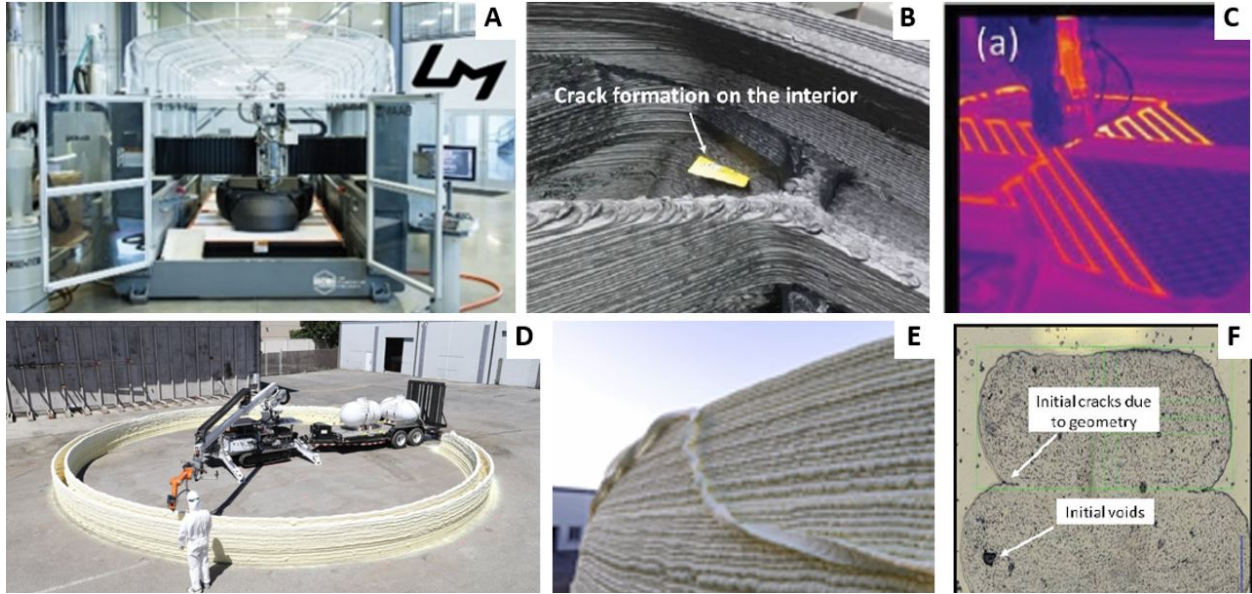
Figure 3-2: Large scale stationary and mobile platforms for continuous deposition. A-C) Big Area Additive Manufacturing (BAAM) platform [83] with noted delamination and thermal issues [13]. D-F) Digital construction platform (DCP) with noted delamination issues at larger scales [84].

Discrete processes

Discrete material systems used in mobile robotic assembly tend to be either bricks, which are solid, or struts and nodes, which are sparse. Brick-based systems can take advantage of the higher ratio of contact surface between parts to allow alignment [85] [86], or rely on passive, gravity-based stacking to build 2.5D structures [87] [88]. Struts and nodes require different strategies for assembly [89], or can be grouped as a modular truss unit [90]

Several implementations of automated assembly show promise for high throughput manufacturing. Desktop-size gantries place parts individually [50] or in parallel [91], and rely on end effector alignment and elastic averaging of part error for overall precision. Strut and node systems designed for human assembly of trusses [92] have been robotically assembled, but at a slower pace due to challenges of alignment and dexterity [93]. Voxel systems have been assembled manually with a throughput on par with commercial FDM [21], and robotic assembly improves this metric [94], indicating benefits of modularity that will be leveraged in this work (Figure 3 3).

Locomotion strategies for mobile assembly robots tend to be either flight, ground-based rolling, or in situ climbing (Figure 3 4). Flight allows robots more spatial access, at the cost of more complex controls to navigate this larger space [87] [89]. Rolling provides stabilization on a ground plane, while requiring the robot to position itself successfully within this more confined space [88] [90]. Crawling, specifically, on the structure, can result in highly customized kinematics, but also allow robots to locally align to the structure [85] [86] [95] [96]. Local sensing, such as IR or contact sensors, gives robots a close feedback loop between

parts and themselves [85] [88] [95], but can have a limited error correction range. Global sensing, typically achieved with LiDAR [89] [87], provides control of the entire workspace, but is limited to a finite range, and thus is not arbitrarily scalable. Centralized control manages single [90] or multiple robots [87] [89], and can be more efficient for small-scale systems, but vulnerable to single points of failure. Distributed systems require more autonomy (and thus complexity) for robots [85][86], but can be more robust and scalable.
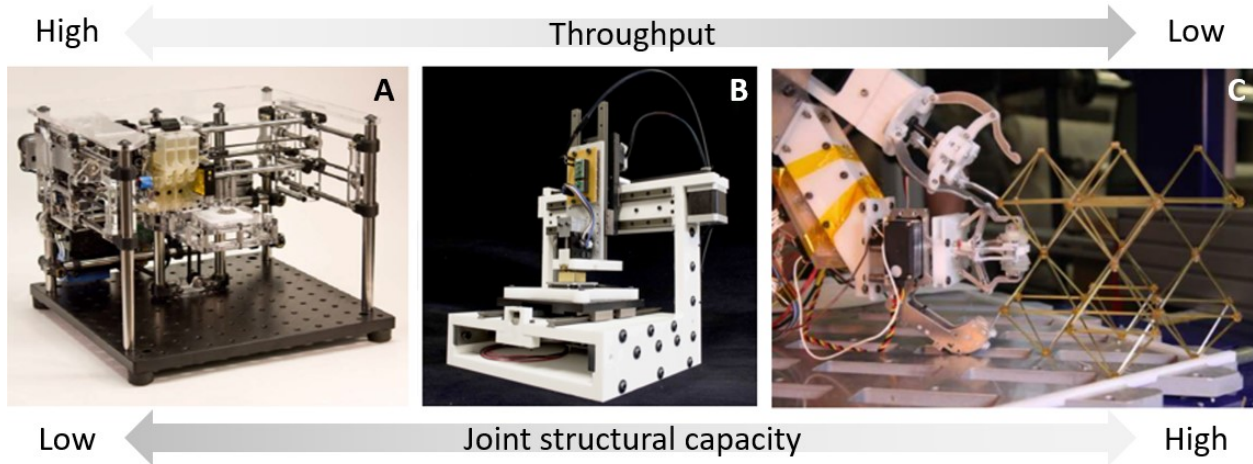
Figure 3-3: Stationary assembly platforms. A) Parallelized sphere deposition joined with binder [50], B) Cassette of parts press fit together one at a time [91], C) Voxels, nuts, and bolts are retrieved from pickup station and bolted together in build area [94].
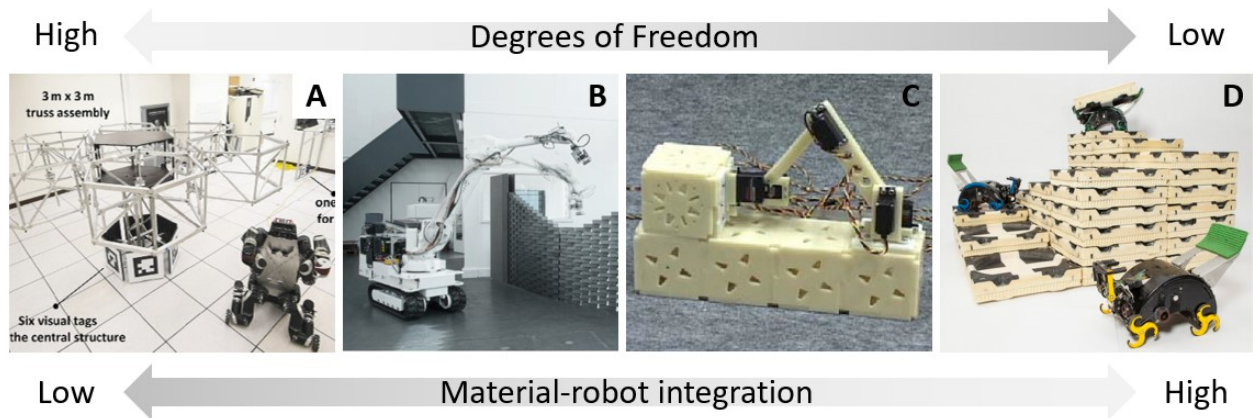
Figure 3-4: Mobile robotic assembly systems. Truss assembly [90] and brick placement [97] by externally mobile robots, and brick assembly by more integrated robots using active [86] and passive [98] bricks.

3.2 Relative Robots

I define *relative robots* as a new type of robot designed relative to a discrete material system. Relative robots are task specific, and their geometric, kinematic, and dynamic properties are a function of the periodic environment in which they operate. Relative robots seek to leverage this environment for simplification and improved reliability. The following examples will illustrate these points. Note: the following sections contain material previously published by the author and colleagues in [99] and [100]

3.2.1 MOJO

The MultiObjective Journeying (MOJO) robot is the first designed and tested relative robot. It is designed to explore the inside of the lattice, and does so by having two main capabilities: moving forward (or backward) a cell, and turning.

The robot consists of a top and bottom half which are identical and oriented 90 degree to each other (FIgure 3-5). A single half consists of two servo motors, each of which drives an arm that is paired to the opposite arm with a gear, such that one motor drives the top pair of left and right arms and the other motor drives the bottom pair. The arms are designed as a scissor mechanism, which can translate along a prescribed path as well as retract. The former is for performing climbing motions, which will be described more in a moment, and the latter is for avoiding collisions while the robot is moving. The robot has custom made end effectors which are designed to interact with specific portions of the lattice during specific steps of the motion, whether static or dynamic.
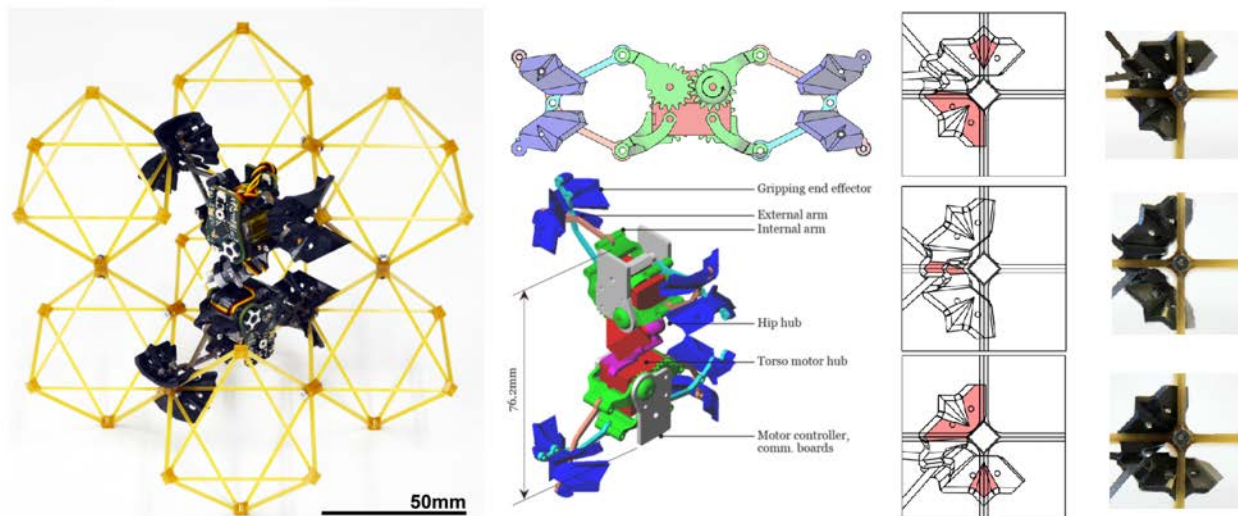
Figure 3-5: Multi-Objective Journeying (MOJO) robot, from [99]. (L to R) Robot occupies a single cuboctahedra cell in lattice, main components and arm scissor mechanism, custom end effectors for interfacing with lattice at various timesteps.

Climbing consists of the following motions: 1) Top and bottom engaged (stable starting position), 2) Bottom retract (top still engaged, maintains robot position), 3) Top performs sweeping motion to move robot up one half cell, 4) Bottom engages upward, 5) Top retracts (now contact is maintained by bottom feet), 6) Bottom performs sweeping motion to move robot up one half cell, 7) Top and bottom engaged.

Turning consists of the following motions: 1) Top and bottom engaged, 2) Top retract (bottom still engaged, maintains robot position), 3) Hip rotate, 4) Top extend and engage, 5) Bottom retract (top still maintains contact), 6) Hip rotate, 7) Bottom extend and engage.

The robot is shown completing these motions in a lab environment in Figure 3-6. Due to the scale of the robot (76mm nominal length), the motors that fit within the geometric constraints only had sufficient torque to enable vertical climbing. While climbing horizontally, the robot would deflect slightly under self-weight, and this overcoming the gripping force provided by the motors. Because the robot did not have any feedback or error correction capabilities, there was a roughly 50% failure rate for horizontal climbing.

Following these lab tests, the robot was tested in zero gravity on a parabolic sub-orbital flight. Here, the robot was able to successfully execute all of it's motions, as noted in Table 3. The only failures occurred due to battery hardware related issues, as the robot was wireless for these experiments. While the robot was successful, it also illustrated several key points: one is that while the parts may be able to scale down an order of magnitude, the same cannot be said for actuation without looking into what kind of torque density will be needed. As we saw here, using a commercial off the shelf servo failed to meet our needs, though a higher torque, custom actuator could of course be designed. Second, the ability to error correct is critical. This robot was not able to error correct, actively or passively, and simply would fail when it encountered error above a certain (small) threshold. Part of the strategy behind relative robots is to make this error threshold sufficiently large so that the precision requirements of the robot become relatively low. This enables a simpler, cheaper robot to be built, but as we have seen, that has its limits.

Table 3: MOJO 1g and 0g test results

Test	Time (gravity agnostic)	Success rate, 1g	Success rate, 0g
Vertical climb	10s	100%	95%
Horizontal climb	10s	50%	95%
Turn	5s	67%	95%
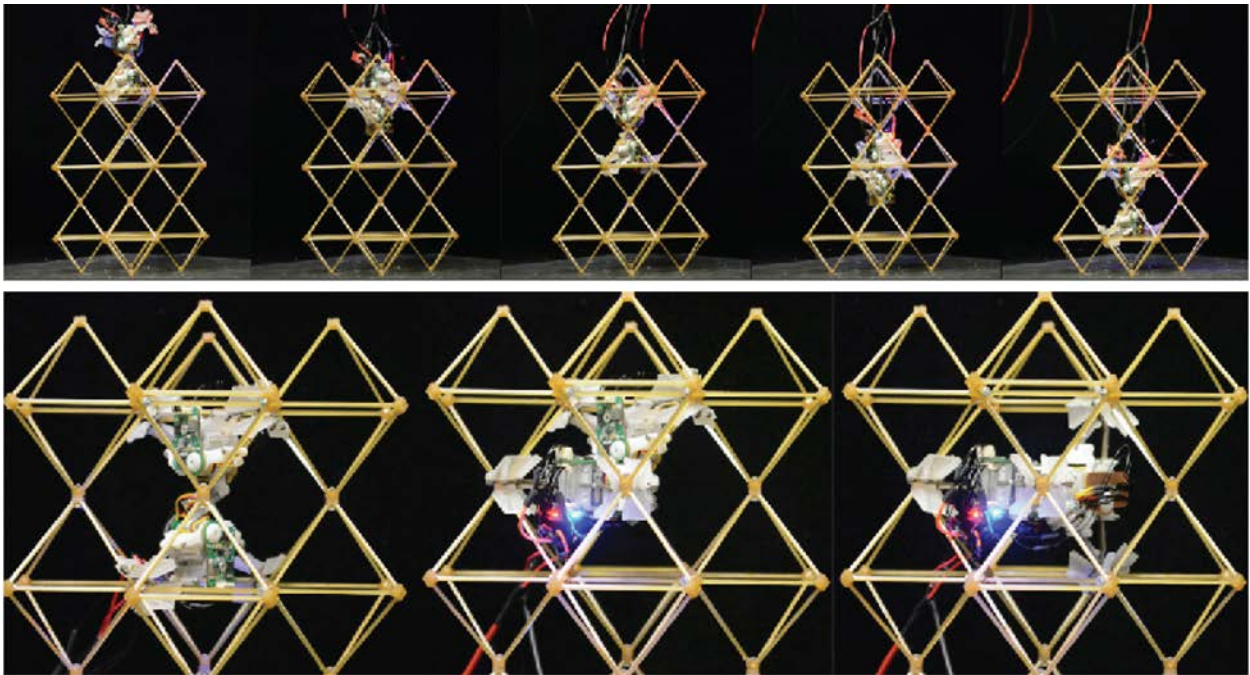
Figure 3-6: MOJO experiments. Performing vertical climbing and turning maneuvers in a 1g envionment, from [99].

3.2.2 BILL-E 1.0

Here I will describe the Bipedal Isotropic Lattice Locomoting Explorer (BILL-E) [100], which is a relative robot designed to locomote on the exterior of a lattice structure. In contrast to MOJO, this robot has more space to occupy, and also was designed with some error correction capabilities, as we will see this contributes to its overall better performance and greater functionality, thus demonstrating one of the key strengths of relative robots.

The robot was designed to accomplish this using the following functional requirements:

- Ability to traverse linearly (X, Y or Z)

- Ability to turn between orthogonal directions (X to Y and Z, Y to Z)

- Ability to turn up/down concave and convex corners

- Ability to step up/down a level ($+/-$ Z)
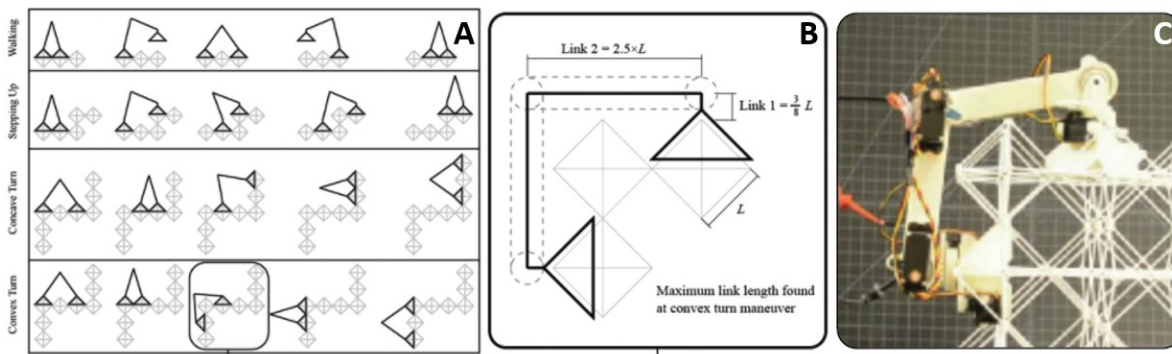
Figure 3-7: BILL-E functional requirements. A) Walking, stepping up, concave and convex turning, B) Robot dimensions governed by requirements of convex turning, C) Built robot [100]

Based on the functional requirements, we can determine the approximate dimensions as a function of lattice pitch L. The convex corner turn requires the longest reach, and thus the robot design is based on this maneuver. Simpler maneuvers, such as linear steps, can reach much further than a single inch-worm step (Figure 3-8).

From here, we discuss sub-components, the following of which will be described: foot, lower leg, upper leg, and actuated joints, as labeled in Figure 3-9. The foot is designed to fit around the outside of the top half of one octahedron. It terminates in a cylindrical feature with outside diameter designed to press-fit into the ankle bearing. The foot has mating features that align with the four nodes of the voxel. These contact points provide a rotational constraint in X, Y, and Z as well as a translational constraint in X, Y, and –Z. The +Z constraint is provided by the latching mechanism, which passes through a pair of holes in the foot and underneath the top interior corner of the voxel, thereby constraining the foot in +Z. The latch is driven by a small servo motor mounted to the outside of the foot.

The foot is press fit into the inside race of a radial bearing. The outside race is press fit into the lower leg link. This provides a rotational degree of freedom in the Z direction, while providing a translational constraint in X, Y, and Z, and a rotational constraint in X and Y. This rotation is actuated by a pair of spur gears. One gear is built into the lower leg, the other gear is mounted to a small servo. The top of the lower leg consists of a bracket and a shaft which is press-fit into the inside of a bearing. The outside of the bearing is press-fit into the end of the upper leg portion.

There are two types of upper legs. Each type has a similar interface with the lower leg. A servo motor is mounted so that its output spline radial axis is aligned with bearing interface with the lower leg. The lower leg shaft extends through the bearing and rigidly attaches to the servo spline. This allows a rotational degree of freedom between the upper and lower leg to be controlled by the servo. The upper legs interface at the "hip", where a similar rotational degree if freedom is used between the two upper legs. One leg has a shaft which press-fits into the inside of a bearing. The other leg press-fits around the outside of the bearing, and a servo is mounted to align with the bearing. The servo is rigidly attached to the shaft of the other leg which passes through the bearing.
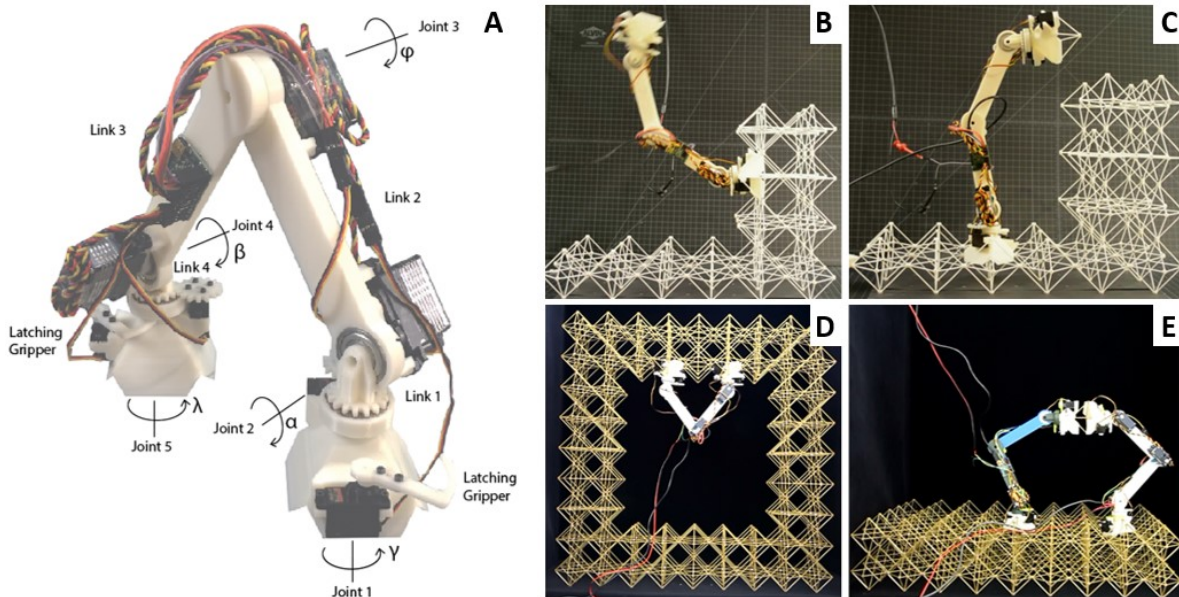
Figure 3-8: BILL-E (v1) robot. A) Robot platform, B) Stepping up a level, C) Placing a voxel, D) Inverted locomotion, E) Passing a voxel between robots. From [100]

1- Knee Joint Actuator
2- Servo Horn Hirth Joint Coupling
3- Knee Joint Radial Bearing
4- Upper Leg Link
5- Lower Leg Link with Integral Gear
6- Ankle Joint Radial Bearing
7- Ankle Joint Mechanism + Actuator
8- Latch Mechanism + Actuator
9- Latch Mechanism Slot
10- Foot End Effector
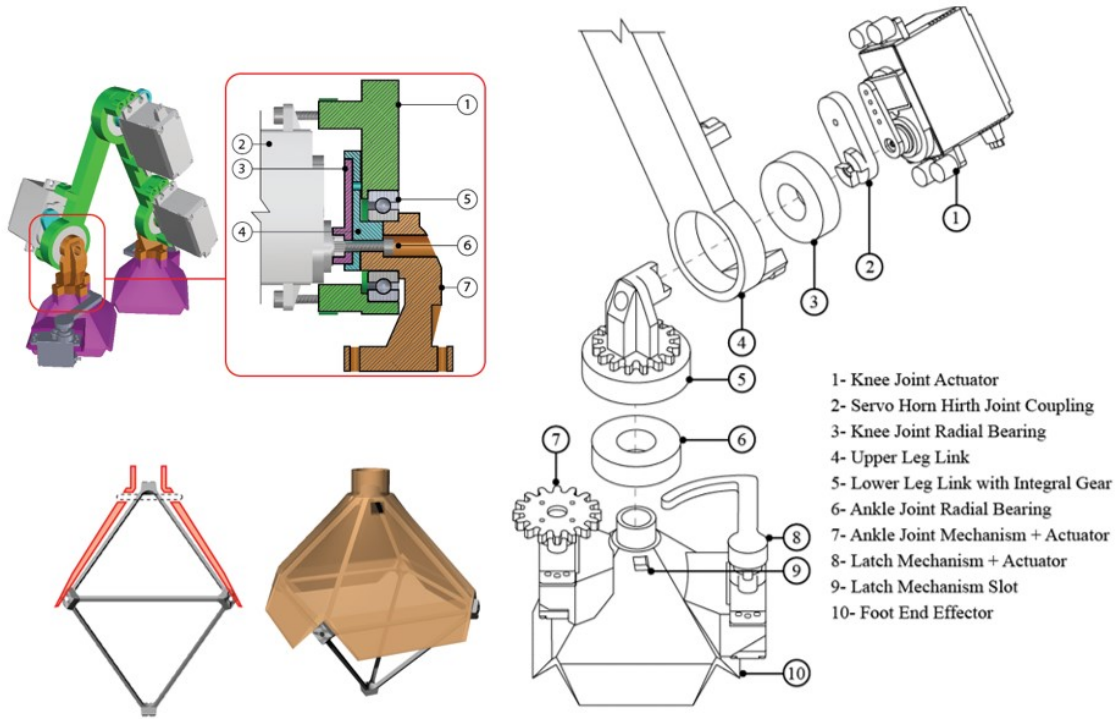
Figure 3-9: Voxel gripping end effector. (L) Voxel geometry is used to design the end effector, which aligns with voxel features, (R) exploded view of foot, ankle, and leg mechanisms. From [100]

Basic experiments
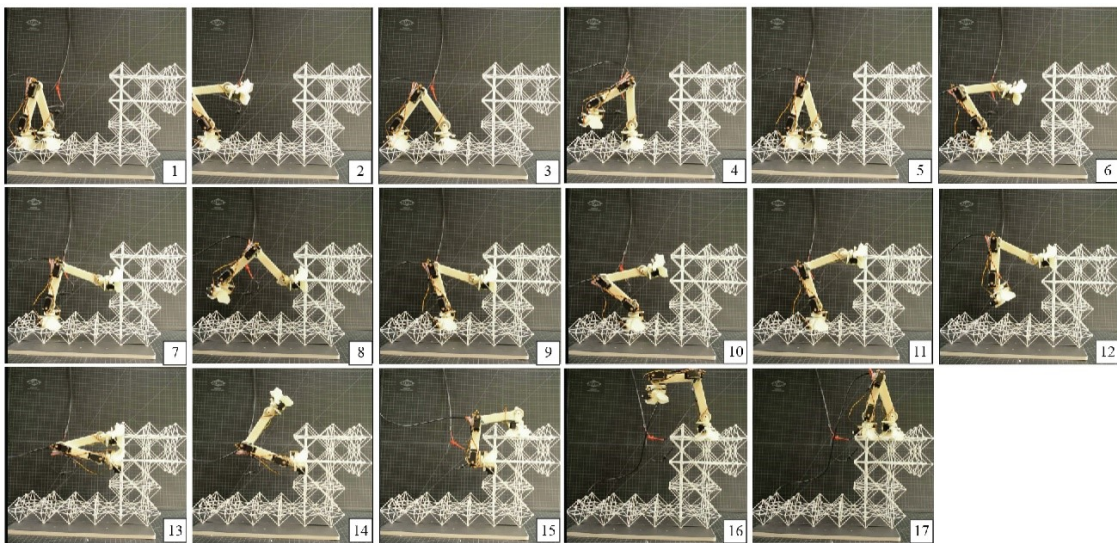
Figure 3-10: Simple stepping locomotion. (1-5) the robot takes single steps forward, (6-11) concave cornering, (12-13) it steps entirely onto the vertical face of the structure, (14-15) convex cornering, (16-17) sequence completion. Total elapsed time: 5 min. From [100]

Figure 3-11: Demonstration of climbing 360° around a loop. (1-3) Concave cornering, (4-6) 180° ankle rotation, (7-9) concave cornering, (10-12) stepping, (13-15) concave cornering, (16-18) 180° ankle rotation, (19-20) concave cornering, (21-24) 180° ankle rotation, end sequence. Total elapsed time: 10 min. From [100]

Error correction

Following this proof-of-concept demonstration, I decided to investigate a bit further the ability of the robot to error correct by aligning to the lattice as it takes steps. This is a critical assumption for the robot to travel long distances while maintaining high relative precision without and global sensing or metrology. To test this, I designed two types of robot feet to modify the existing BILL-E platform: one using electromagnets to allow the robot to walk on a flat, ferrous surface (ie: a large optical table), and another with a spring-loaded sliding mechanism to enable passive error correction of large, deliberate errors (Figure 3-12). The test would be to determine to what extent passive error correction can be employed over long distances, and compare this to how a rigid, non-error correcting robot with the exact same geometric and kinematic parameters would perform.

The results clearly demonstrated the significance of error correction. In Figure 3-13, I show the standard robot taking a step on the lattice with a programmed step error of 12.7mm. The robot fails to engage with the lattice, and when it begins to move the back foot, it falls off the lattice, which is considered a failure. Next, the same robot, with the same programmed step error, performs the same test, but this time with the passive error correcting foot. In Figure 3-14, the robot is successful in completing the steps, as a result of the passive error correction.
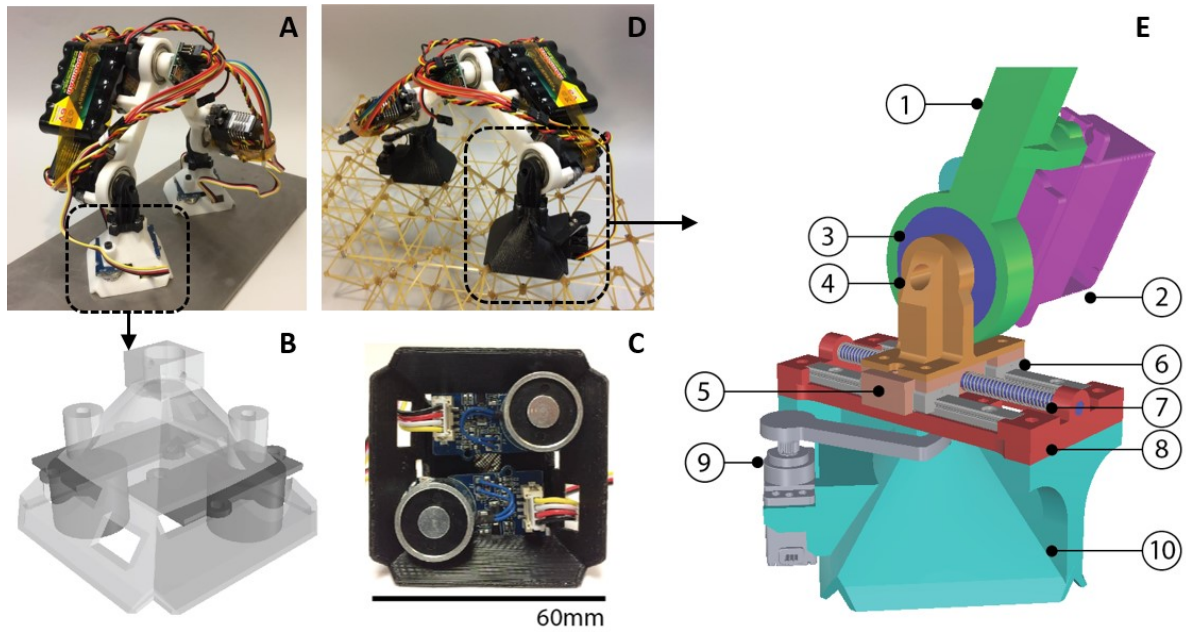
Figure 3-12: Error correction test platforms. A) Flat surface locomoting robot, B) Detail and C) Bottom view of electromagnetic foot, D) Lattice locomoting robot with E) Foot modified with spring-loaded linear degree of freedom to enable passive error correction.

Next, I tested this capability over a longer distance. In Figure 3-15, I show a test using a beam which is 3x2x40 voxels (length = 3m). On top, I show the lattice and magnetic surface BILL-E's overlaid. They are programmed with the same motion, which is each step equal to a single lattice pitch (75mm). The difference in their end positions is negligible (under 1mm). In contrast, on the bottom I show the same test using the 12.7mm error. While the magnetic surface robot shows cumulative error over the span of its travel, the lattice robot performs passive error correction, ending at the exact same position as the robot with the error-free motion program.

The step length is 76.2mm. Due to the design of the compliant mechanism, there is only 22mm of error tolerance, while the design of the foot end effector can accommodate up to 30.5mm while still aligning.

Table 4: BILL-E error tolerance test results

	Error tolerance (mm)	% of step (76.1mm)	Factor increase
Rigid Foot	1.25	1.6	1
Compliant foot	22	29%	18
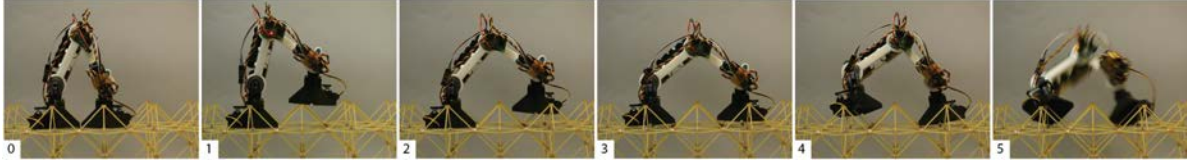
Figure 3-13: Failure of lattice robot with deliberate error. Robot fails to correct errors over 1.25mm. Current error is set to 12.7mm
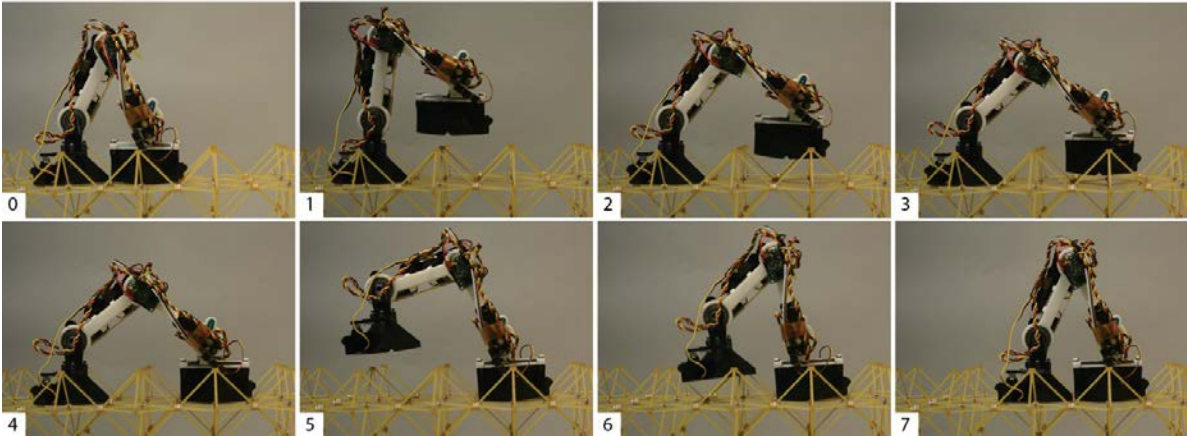
Figure 3-14: Passive error correction. The same error as shown in the rigid version, 12.7mm, is easily accommodated by the alignment mechanism.
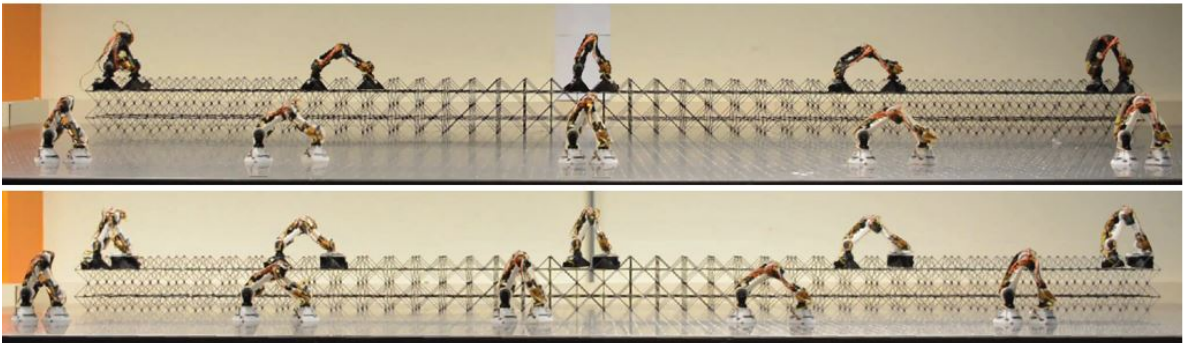
Figure 3-15: Long distance (3m) travel tests. (Top) Ideal step size with discrete lattice robot and continuous robot showing nearly identical travel distance. (Bottom) Compliant lattice robot and continuous robot with artificial error, showing compliant robot provides error correction while continuous robot suffers from cumulative error.

3.3 Material-Robot System

Building on *relative robots*, here I introduce the *material-robot system*. Here, the discrete material and robot are designed simultaneously, which enables the benefits of relative robotics while ensuring geometric compatibility and practicality. While the previous robots were designed for a vertex connected octahedra with a 3in pitch, here the voxel is scaled up slightly based specifically on robot requirements, and the size of the motors available to do it. In this way, we can achieve both structural performance and robot functionality without sacrificing either. Note: this section contains material previously published by the author and colleagues in [105]

3.3.1 BILL-E 2.0

In contrast to BILL-E v1, the voxel geometry used here is a cuboctahedron (referred to herein as Cuboct), with lattice pitch P = 101.6mm (4in), and strut length l = 71.84mm (2.83in). The Cuboct cell is decomposed into 6 uniform faces (Figure 3-16). The faces are 3D printed PLA, oriented parallel to the build plate to promote continuous material orientation along the strut axes. 3.175mm cube magnets are then press-fit into pockets at the nodes, with opposing magnet poles oriented as shown. This ensures that the faces, and thus the voxels, are rotationally symmetric and orientation agnostic. Faces are then joined at their vertices using interlocking features and a screw which acts in shear, in addition to partially cold-tapping into the plastic for retention.
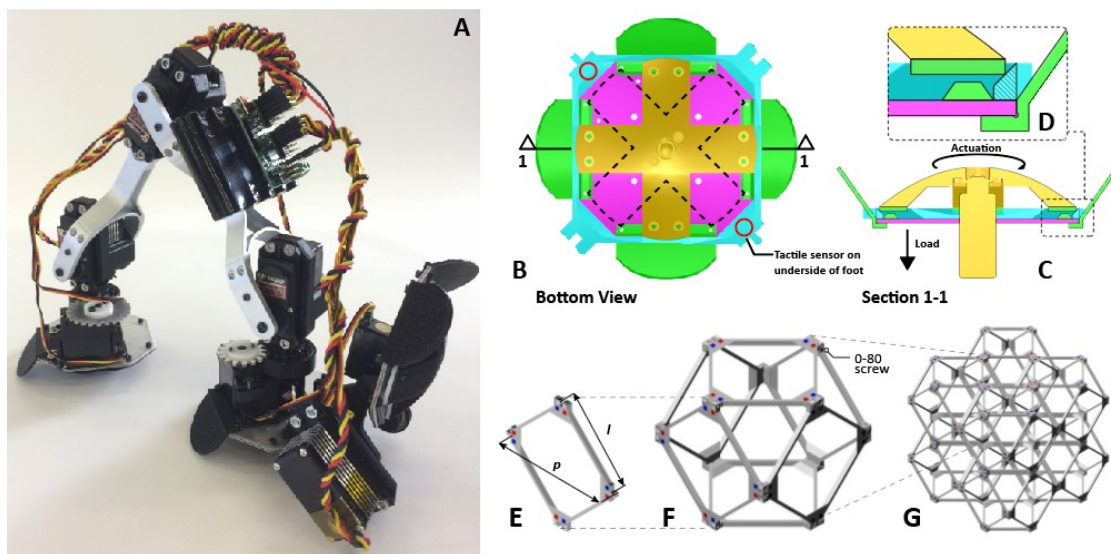
Figure 3-16: BILL-E v2 [105]. A) Final robot, and details of end effector, B) Bottom view of voxel face, shown in blue. Ungripped key position is shown in dashed lines, allowing entry/exit to/from a voxel. C) Section view of key in gripped position, D) Magnified view showing passive and active constraints engaging with voxel feature, E) Modular face with press-fit magnets, colored to indicate orientation. F) Cuboct voxel consisting of 6 faces, G) Assembled 2x2x2-voxel cube
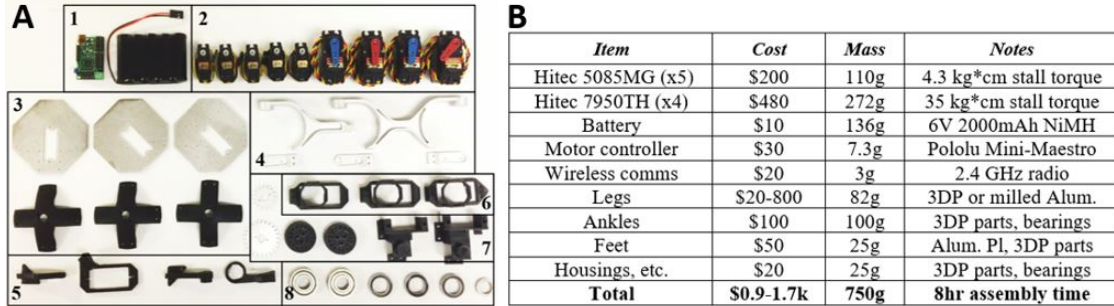
Figure 3-17: BILL-E v2 bill of materials [105]. 1. Control board and battery, 2. Motors, 3. Foot end effectors, 4. Legs, 5. Part placement mount, 6. Main motor hubs, 7. Ankle hubs and gears, 8. Bearings.

Item	Cost	Mass	Notes
Hitec 5085MG (x5)	$200	110g	4.3 kg*cm stall torque
Hitec 7950TH (x4)	$480	272g	35 kg*cm stall torque
Battery	$10	136g	6V 2000mAh NiMH
Motor controller	$30	7.3g	Pololu Mini-Maestro
Wireless comms	$20	3g	2.4 GHz radio
Legs	$20-800	82g	3DP or milled Alum.
Ankles	$100	100g	3DP parts, bearings
Feet	$50	25g	Alum. Pl, 3DP parts
Housings, etc.	$20	25g	3DP parts, bearings
Total	**$0.9-1.7k**	**750g**	**8hr assembly time**

Our robot architecture is based on an inchworm archetype [40]. The geometric configuration is driven by functional requirements for navigating within a cellular environment, as described in [36]. Besides requiring a new end effector to interact with voxels, the most critical update from this previous version is a redesign of the leg motor hubs. Motors have been relocated to align with the robot primary axis, reducing the robot width to that of a single voxel, which allows the robot to pass by a wall without collision. This requires a new fork-type interface to attach legs to the servo horns and a low-profile bearing pressed into the back of the motor housing. The robot comprises nine servo motors, is powered by a 6V rechargeable battery, and communicates wirelessly with a central controller using 2.4 GHz radio (Figure 3-17).

The end effectors for foot attachment and voxel placement are the same (Figure 3-16). The gripping mechanism is designed to use as many passive and as few active degrees of freedom (DoFs) as possible. Alignment features constrain translation in x and y, and rotation in z. A single actuator rotates a cruciform "key" 45° to create four contact points with customized surfaces on the underside of each beam of the top square face of the voxel. This constrains z translation and x and y rotation. The actuation DoF is orthogonal to the loading direction, thus decoupling these functions and requirements. When the key is in the locked position, the stiffness of the gripper is a function of the key's geometric and material properties, as opposed to the torque capacity of the motor.

3.3.2 Controls

Architecture

The overall control architecture is shown schematically in Figure 3-18. Individual control levels will be described in order from high to low level in the following subsections. To summarize, our control scheme works as follows: CAD models of a given discrete cellular structure can be represented as a 3D bit matrix, or as functional representations (f-reps) in our custom software environment. Next, a build sequence is determined, based on environmental/operational constraints. Depending on single or multi-robot construction, path planning for each voxel in the build sequence is sent to the robot. Each path consists of

linked primitive moves, such as "step" or "turn 90°". Primitive moves consist of a list of motor positions, which when executed in order, result in the desired motion. Lastly, sensors detect errors during motion execution, and thus can provide feedback to avoid failure.
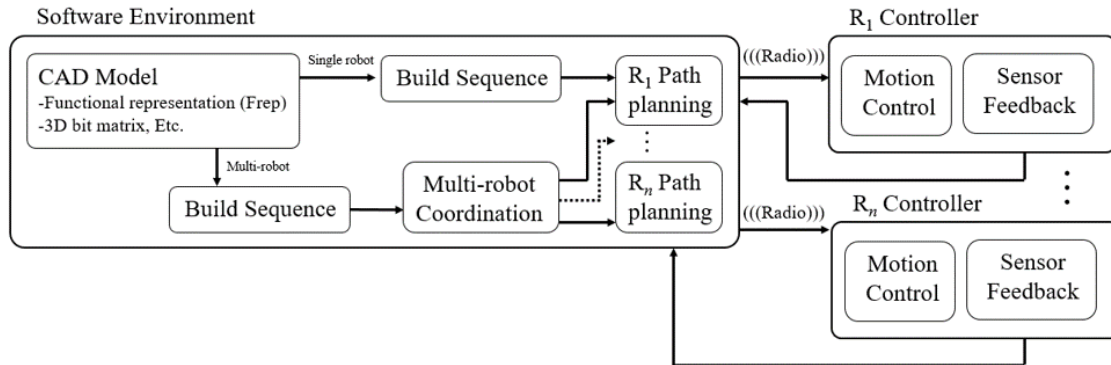
Figure 3-18: Schematic control hierarchy [105]. The software environment centrally computes build sequences and path planning and delivers strings of motion commands to robots through serial over 2.4 GHz radio

Build Sequence

We determine the order in which voxels are placed based on three main considerations. First is the number of robots. Multiple robots allow multiple build fronts, or group construction on a single build front, but require coordination to avoid collision and deadlock, which will be addressed later. Second is environmental factors such as gravity. In a 1g environment, it is reasonable to build in layers parallel to the ground plane, moving up in the z direction. In a zero-gravity environment, this restriction would not exist. Algorithms for zero-g construction will be addressed in future work. Lastly, we must consider where the part source, or pickup location is, and how many locations there are, as this will drive where construction begins as well as possible build directions.

The proposed building sequence algorithm imposes geometric constraints of what can be built. We assume the built geometry is a connected geometry, though horizontal layers can have unconnected areas, as long as each area has at least one voxel connected to the layer underneath (Figure 3-19). A voxel can be built at layer n as long as it has at least one empty neighbor in the same layer. If a sacrificial layer is required as shown, this could be removed later by a robot similar to [37] but would not be needed in zero gravity.
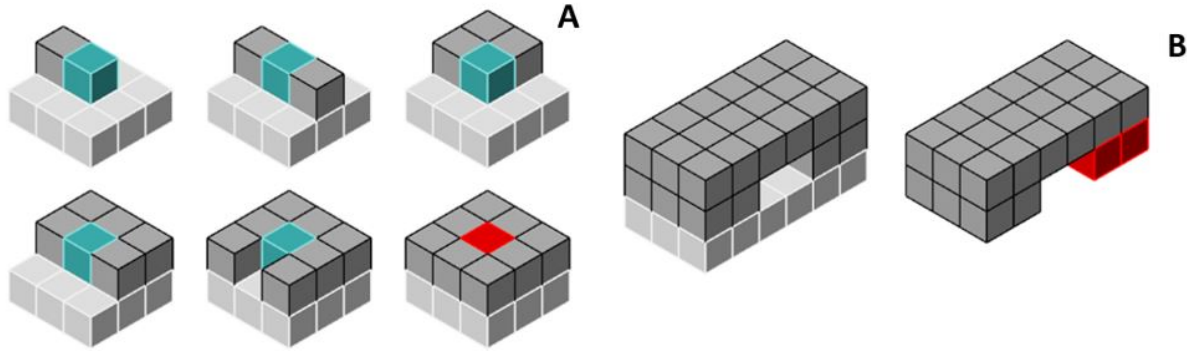
Figure 3-19: Geometry Specifications and Building Constraints [105]. A) Placement constraints based on the current robot design, B) Unconnected areas for a build layer are possible with connectivity below, under-hangs are not possible.
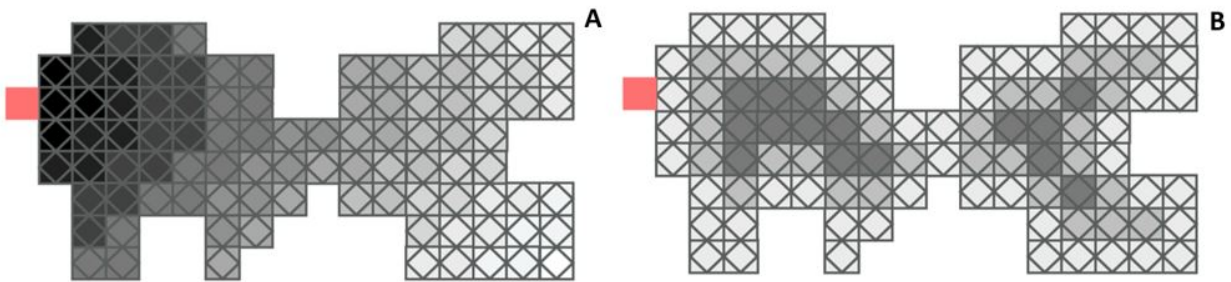
Figure 3-20: Layer Building Sequence comparison between the proposed algorithms [105]. A) Algorithm 1: Manhattan distance values to the pickup station B) Algorithm 2: Distance field values/ranks.

Two algorithms for choosing the building sequence will be presented, one is a deterministic algorithm that is more suited for single robot construction, and the other is more flexible for multi-robot construction. The first algorithm assumes the simple case of single robot with one set pickup station. The building sequence is layer by layer, and in each layer the voxels are sorted based on the Manhattan distance to the pickup station location. In this case the entire build sequence can be precomputed. For structures with no overhangs and no unconnected areas at any layer, no extra consideration is needed to determine the building sequence (Figure 3-20A).

For structures with overhangs and cantilevers, the voxels are sorted differently. At each layer, we find the voxel with both the smallest Manhattan distance to the pickup station and an existing neighbor underneath it. Then, the rest of the voxels are sorted based on the Manhattan distance to this first voxel. In the case of layers with unconnected areas, for each area, we have to find the voxel with both the smallest distance and connected to the layer underneath it and start to build around it. This sorting algorithm is presented here in pseudo code:

Algorithm 1: Sorting algorithm for single robot construction

1:**For** each layer *I* in structure
2:    set *v_not_sorted* to voxels in layers *i*
3:    set *v_reference* to *pickup_location*
4:    set *v_sorted* to empty list
5:    **While** *v_not_sorted* length not = to *v_sorted* length
6:        **If** *v_reference* is the *pickup_location* **then**
7:            *V* is the closest voxel to *v_reference* and
                    neighbor at layer *i-1* exists
8:            set *v_reference* to *V*
9:            add *V* to *v_sorted*
10:      **Else**
11:           *V* is the closest voxel to *v_reference* and at
                least one neighbor in *v_sorted*
12:        **If** *V* doesn't exist **then**
13:            set *v_reference* to *pickup_location*
14:        **Else**
15:            add *V* to *v_sorted*
16:        **End if**
17:      **End if**
18: **End while**
19: **End for**

Path Planning

After having determined the build sequence, an individual robot needs a path from a pickup location to a target location, given an existing voxel configuration. Here we employ a method that uses A* search which minimizes the function:

$$f(n) = g(n) + h(n)$$

Where g(n) is the cost of moving from the start to voxel n and h(n) is the estimated cost of moving from voxel n to the goal. The Manhattan Distance between two voxels is used as the heuristic function. For single robot construction, all paths are computed offline, which are then sent to the robot. Individual path sequences consist of linking together primitive motions to move the robot from starting location to target location. In the case shown in Figure 3-21, the goal is to place the voxel in the bottom left corner of the image. To accomplish this, the robot follows a path sequence which is exported as a string to be read and executed by the motor controller.
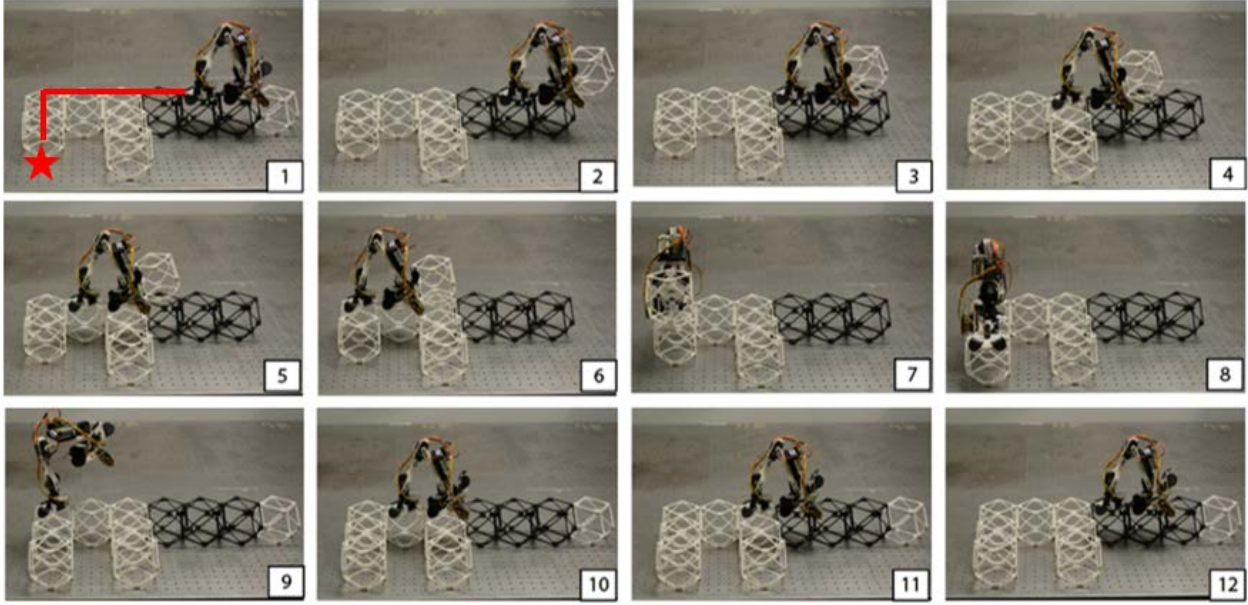
Figure 3-21: Step-by-step path sequence [105]. 1) Stand, 2) Pick up voxel, 3) Step back, 4) Step back, 5) Step back, 6) Step back, 7) Turn 90º, 8) Place voxel, 9) Turn -90º, 10) Step forward, 11) Step forward, 12) Step forward

Robot coordination

In case of multiple robot construction, when using the second algorithm, we wish to avoid robot collision. The centralized system is aware of the location of the deployed robots at each timestep t (based on the previously calculated paths) and uses this when performing the next path search. If no such path exists, the robots wait for a certain amount of timesteps until a path is cleared. We call this strategy spatio-temporal scheduling, and it is similar to a strategy studied by Murata and Terada [41]. Whereas in that example they rely on distributed robot communication and independent agents to perform individual searches, in our centralized approach we search for a collection of robots, noting performance decrease for larger systems. We look at several cases and show how enforcing certain rules will prevent collision (Figure 3-24). Cases A and B look at beginning and ending intersections, case C looks at construction dependencies, and case D looks at mid-path intersection:

-Case A: $t_{\text{start } 1,3} \neq t_{\text{start } 2,4}$; $t_{\text{end } 1,3} \neq t_{\text{end } 2,4}$; $t_{\text{start } 1,2} \neq t_{\text{end } 4,3}$

-Case B: $t_{\text{start } 1} \neq t_{\text{start } 2, \text{end } 4}$; $t_{\text{end } 3} \neq t_{\text{start } 2, \text{end } 4}$

-Case C: $t_{\text{end } 2} > t_{\text{end } 1, \text{ start } 3}$

-Case D: $t_{1,3 \text{ between i-j}} \neq t_{2,4 \text{ between i-j}}$
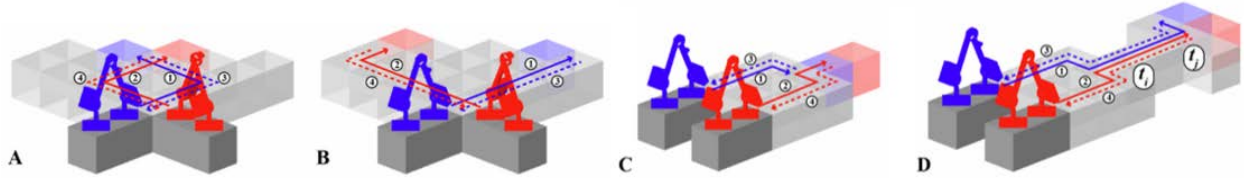
Figure 3-22: Spatio-temporal scheduling [105]. Paths are determined to include updated built structure and to avoid collision.

Motion control

Primitive motions consist of individual motor positions, linked as a sequence to execute the full motion. For example, stepping forward one cell consists of the following primitives: 1) Grip back foot, ungrip front foot, 2) Step front foot forward, 3) Grip front foot, ungrip back foot, 4) Step back foot forward. A list of the main primitive motions is presented in Table 5.

Table 5: Robot motion primitives for path planning sequencing

Motion	Description
Grip/ungrip	Rotation of end effector key between 0-45°
Step forward/back	Parabolic trajectory described by y = -x²+Px, where P is lattice pitch
Turn 0, 90, 180, 270°	Back foot only, front can turn +/- 90° due to placement end effector
Pick up/place voxel	Voxels can be placed on plane or above plane
Step up/down	Stepping up/down more than 1 voxel level requires cornering
Concave/convex corner	Convex corner requires furthest reach, informs minimum leg length

For multi-motor motions, we use inverse kinematics to determine motor angles, which are simplified by enforcing end effector orientation normal to the travel plane (Figure 3-23):

$$\theta_1 = \tan^{-1} 2(x, y) - \tan^{-1} 2(a_2 \sin \theta_2, a_1 + a_2 \cos \theta_2)$$

$$\theta_2 = 2 \tan^{-1} \sqrt{(a_1^2 + a_2^2)^2 - (x^2 + y^2)/(x^2 + y^2) - (a_1^2 + a_2^2)^2}$$

$$\theta_3 = 540° - \theta_1 - \theta_2$$
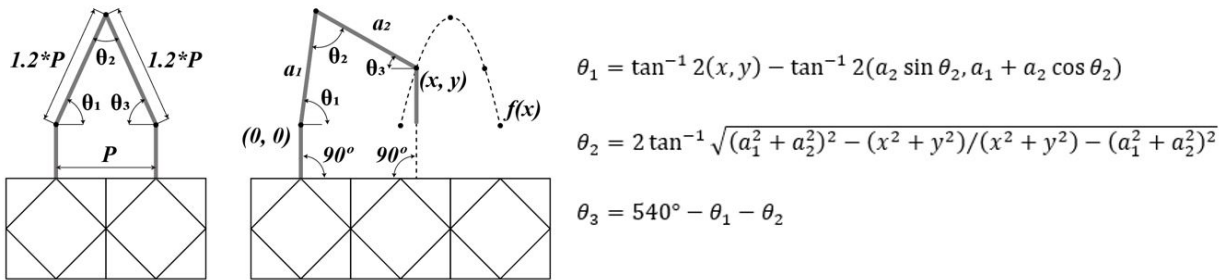
Figure 3-23: Motions and inverse kinematics [105]. Here the robot follows a path using the parabolic function y = x2+Px, where P is lattice pitch.

Feedback

Feedback is provided by tactile sensors on opposite corners of each foot (Figure 3-24). When both sensors are engaged, we can be confident that the foot is correctly placed. A control loop enforces this as a condition to be satisfied prior to locking the newly placed foot and unlocking the other foot to be moved next. Feedback for part placement can be obtained by monitoring torque of the placement motor while pulling on a newly attached voxel. It is assumed that this will be more critical for a fully structural connection scheme, and thus placement verification is left for future work.
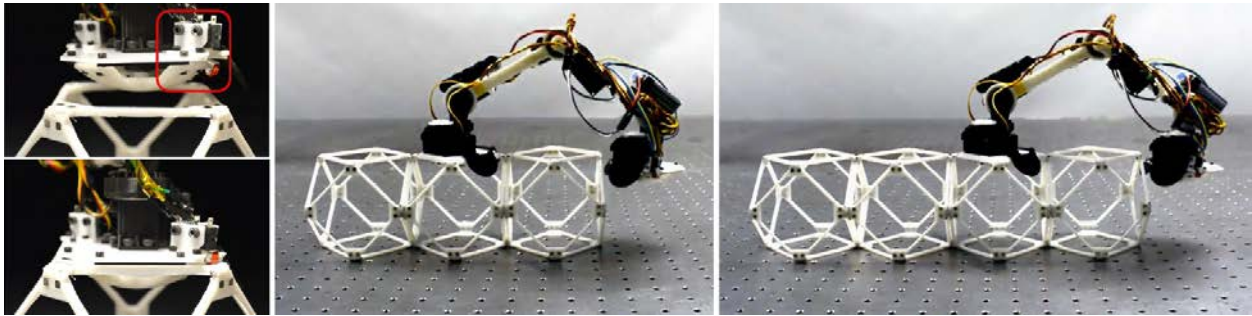
Figure 3-24: Feedback [105]. (L) Tactile sensors on foot end effectors, unengaged (top) and engaged (bottom). (R) Robot performs checking function to ensure it can safely make next step.

3.3.3   Simulations

In order to study tradeoffs and scalability of our system, we perform a variety of simulations in our software environment. This allows us to rapidly compare parameters such as number of robots, number of pickup stations, and number of voxels, while monitoring both number of steps and overall construction time (Figure 3-25). First, we assess the impact of number of robots and part pickup locations (both ranging from 1 to 4) for a 5x5x5 cube. In Figure 3-26, we focus specifically on how to decrease time, comparing between the effect of increasing robots versus increasing pickup stations. Although both decrease time, robot count has a greater impact. Lastly, we look at building cubes with side lengths of 5, 10, 25, and 50 voxels, containing 125, 1,000, 15,625, and 125,000 voxels, respectively, using one to four robots. We see an expected improvement with more robots, but we can also observe construction time increases exponentially with structure scale, due to the increased distance a given robot travels for part pickup and placement.
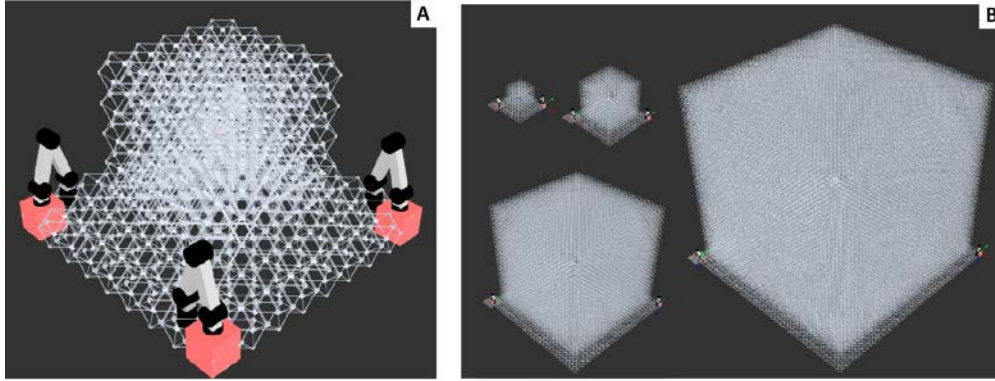
Figure 3-25: Simulation studies [105]. A) 5x5x5 cube, B) Cubes of side length n = 5, 10, 25, and 50.
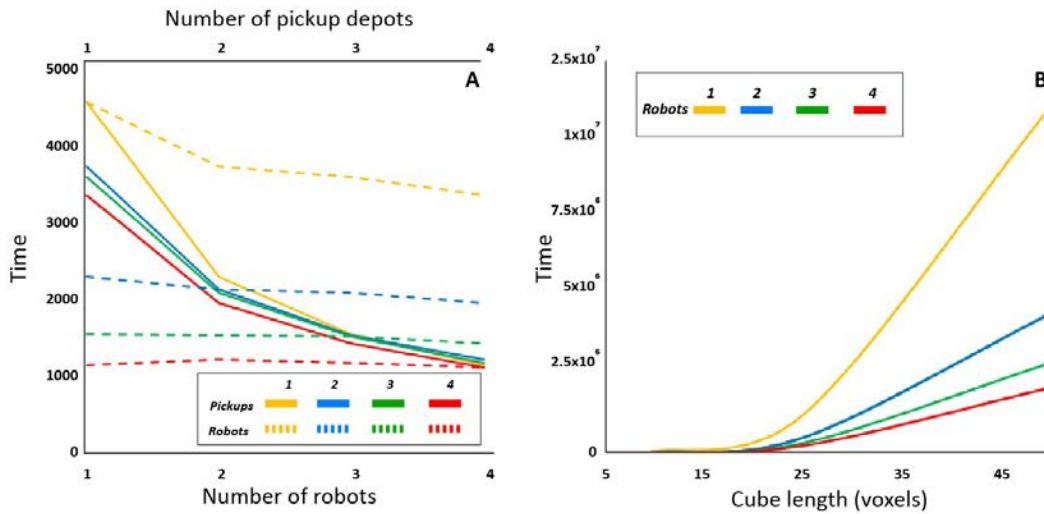
Figure 3-26: Simulation results [105]. A) Varying number of depots and robots for a 5x5x5 cube, B) Varying number of robots for cubes of side length n = 5, 10, 25, and 50.

3.3.4   Experiments

The experiments presented herein were performed on an optical table, which has two important properties to note. One is flatness, which is cited as +/- 0.1 mm (0.004 in.) over a 60 x 60 cm (2 x 2 ft) area. The other is a steel surface the voxels magnetically adhere to it. This provides a controlled build environment, which contributes to successful assembly. Regardless of the configuration of the final structure, there is a minimum base "seed", which consists of a row of three voxels (colored black) upon which the robot initially stands and picks up new voxels, which are refilled manually.

We used a single robot to build three kinds of structures: a 1D beam (Figure 3-28), a 2D plate (Figure 3-29), and a 3D enclosure (Figure 3-30). Results for these experiments are shown in Table 6. Also, we demonstrated 3D locomotion where a robot transports a voxel

over a "wall", requiring concave and convex cornering and vertical stepping (Figure 3-27), which is possible due to the 3D isotropic cellular structure and gripping end effectors.

Two robots were used to build a branching structure and a pyramid. In the former, the robots build separate single-voxel beams, which then turn to intersect. The successful demonstration of independent robot construction on an interconnected structure is significant because it supports the idea that local part metrology determines global precision. The pyramid structure is made up of three layers (5x5x1, 3x3x1, 1x1x1), and demonstrates implementation of multi-robot coordination with spatio-temporal scheduling. While this structure is essentially 2.5D and therefore could be built using other robotic assembly systems, it shows that we can use our approach to build a structure with a part count comparable to state of the art (on the order of 25) [85].
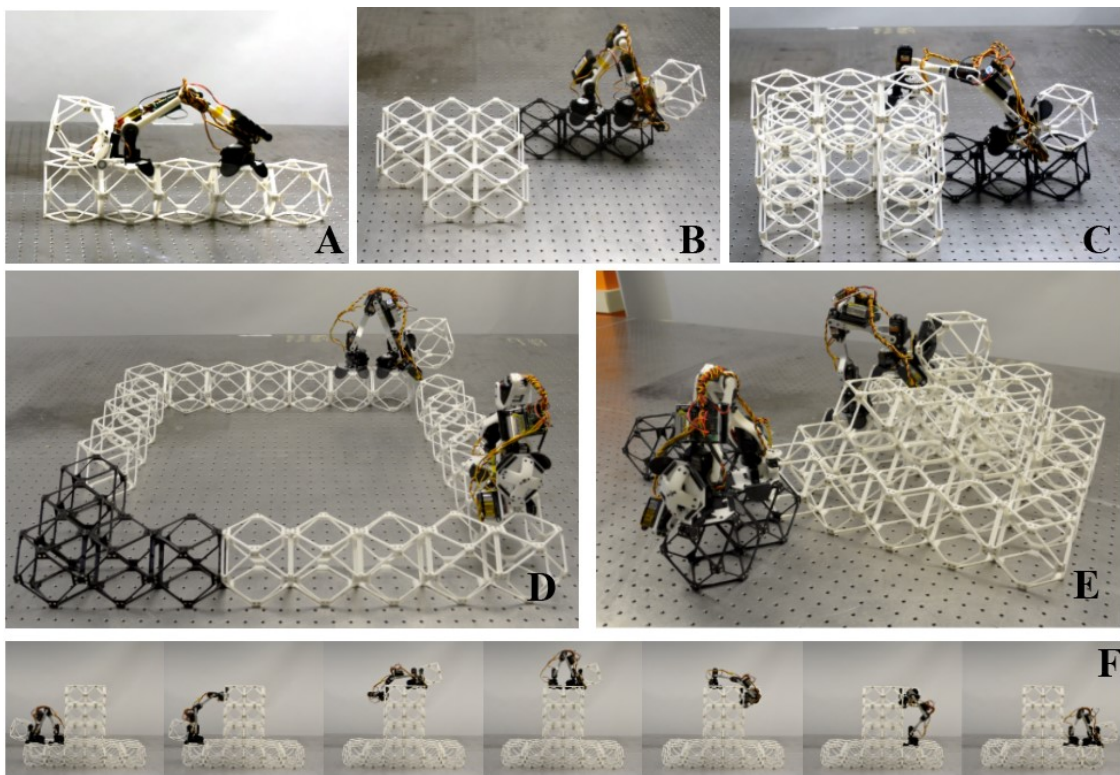
Figure 3-27: Robotic assembly experiments [105]. A) 1D beam reconfiguration, B) 2D plate assembly, C) 3D enclosure assembly, D) Multi-robot construction of branching structure showing global precision from part metrology, E) Multi-robot construction of 35 voxel pyramid, F) 3D locomotion and voxel transport.
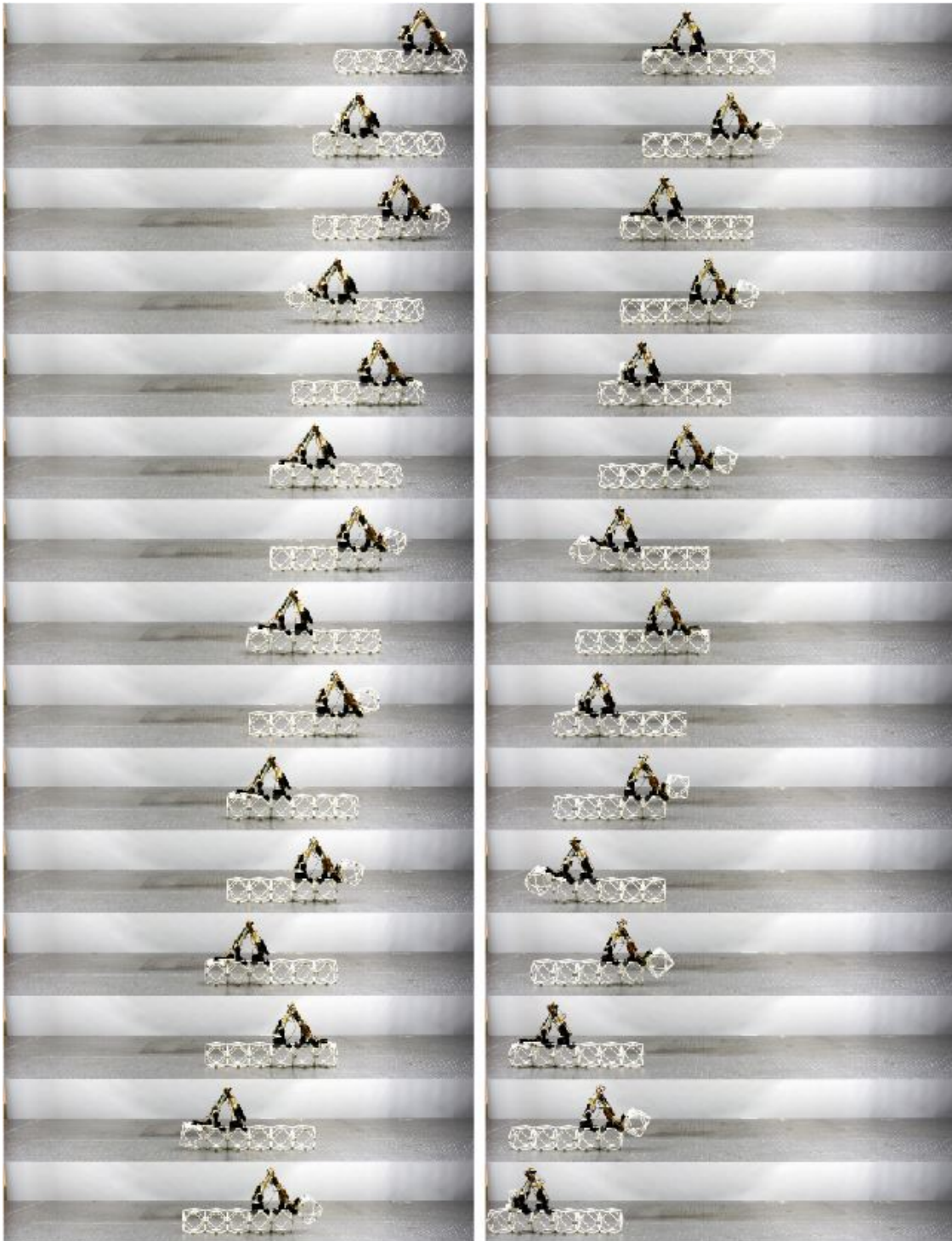
Figure 3-28: 1D beam experiment [105]. Consisting of 6 voxels, reconfigured 15 times. Total experiment time: 6.7 min.
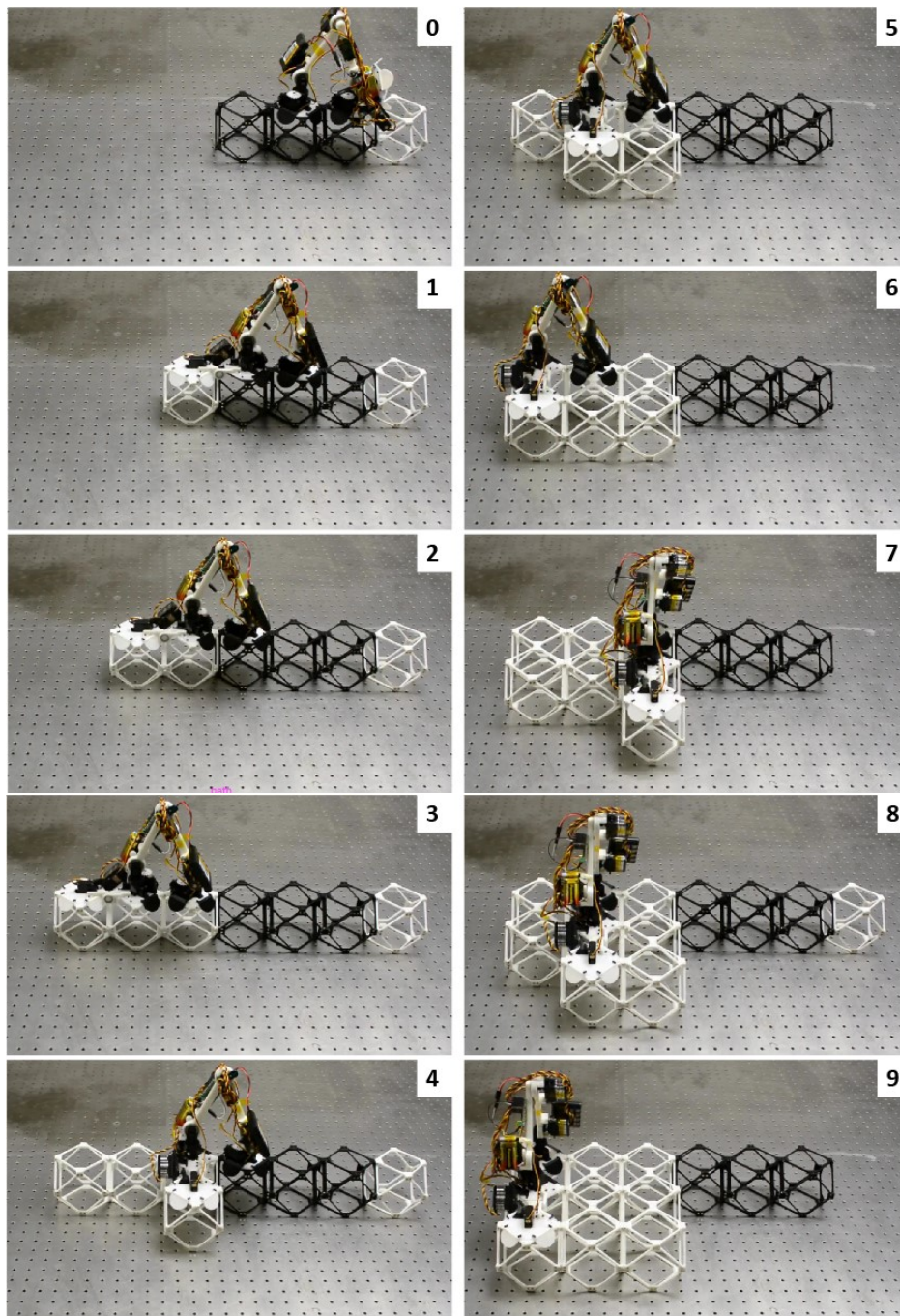
Figure 3-29: 2D plate experiment [105]. Consisting of 9 voxels. Total assembly time: 12 min.
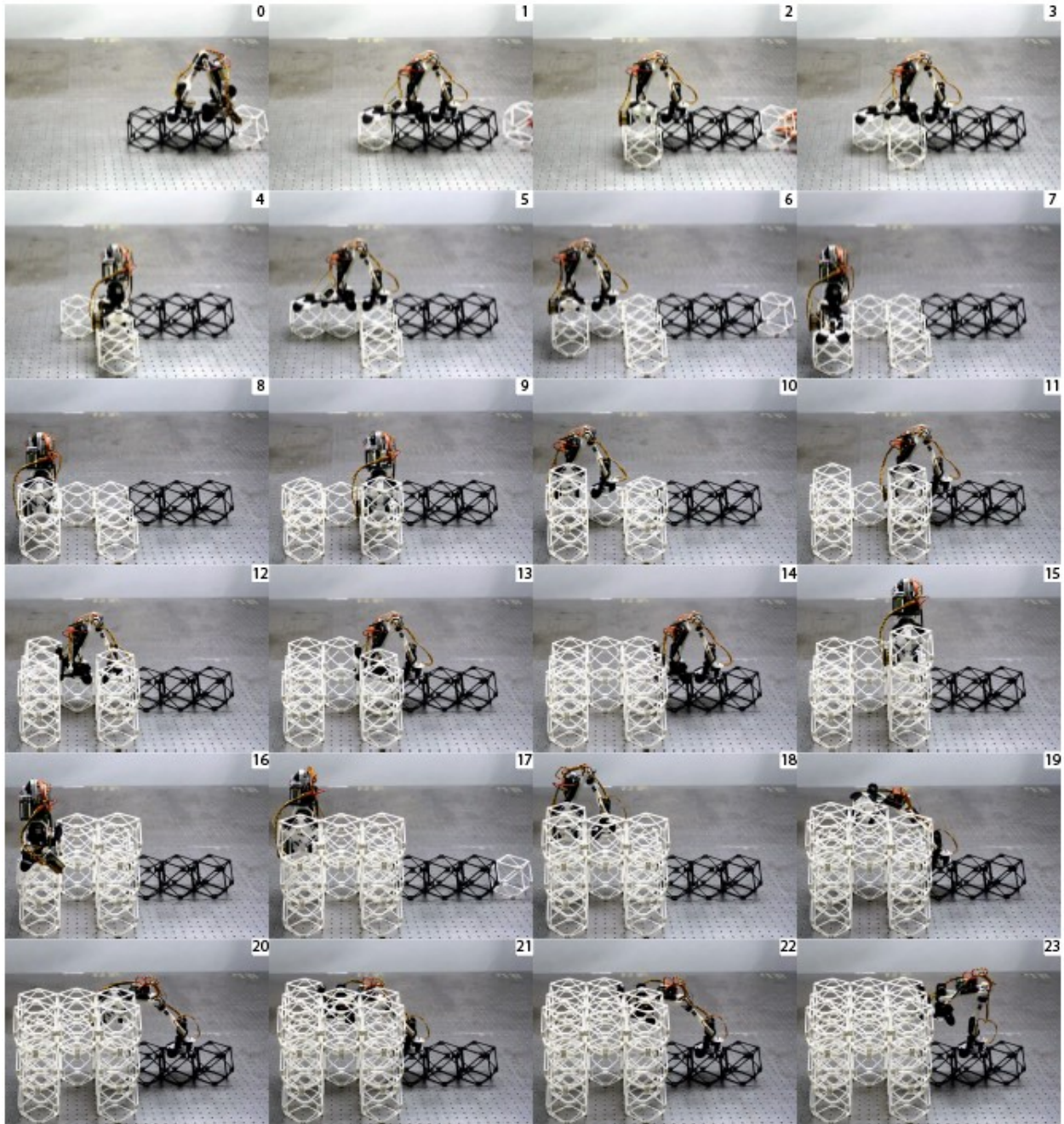
Figure 3-30: 3D volume experiment [105]. Consisting of 23 voxels. Total assembly time: 33 min

Table 6: Robotic assembly test results

	1D	2D	3D	Branch*	Pyramid*
# of voxels	6	9	23	23	35
Motion types	5	7	17	8	10
Total motions	36	70	207	338	352
Avg motion time (sec)	10.5	10	9.5	10	10.5
Build time (min)	6.7	12	33	28.17	30.75
Avg time/voxel (min)	1.1	1.3	1.4	1.21	0.87

3.4 Evaluation

Given a baseline performance for the relative robot in terms of function and speed, now we can look at scaling the system up and comparing to more traditional methods to identify possible advantages. Below is a 0.8x0.8x0.5m version of a low-cost gantry, supplied by Igus, Inc (Figure 3-31). It uses encoded stepper motors (NEMA 23XL) to control belt-driven axes on self-lubricating linear bearings. This gives it high speed at low cost, while maintaining +/-0.8mm accuracy with capacity for 0.5m/s travel with up to 24.5N (5.5lb) end effector payload. The entire platform costs under $10k. This presents a slightly different cost model from heavy, stiff, high capacity gantries for other CNC operations—it is essentially a lightweight pick and place. For this reason, in the future, it will be possible to construct stationary machines using voxels, which are well suited to act as modular, reconfigurable infrastructure ubiquitous in today's modern factories. With the addition of recursive assembly, addressed at the end of the chapter, there is a compelling ecosystem of a variety of material-robots.
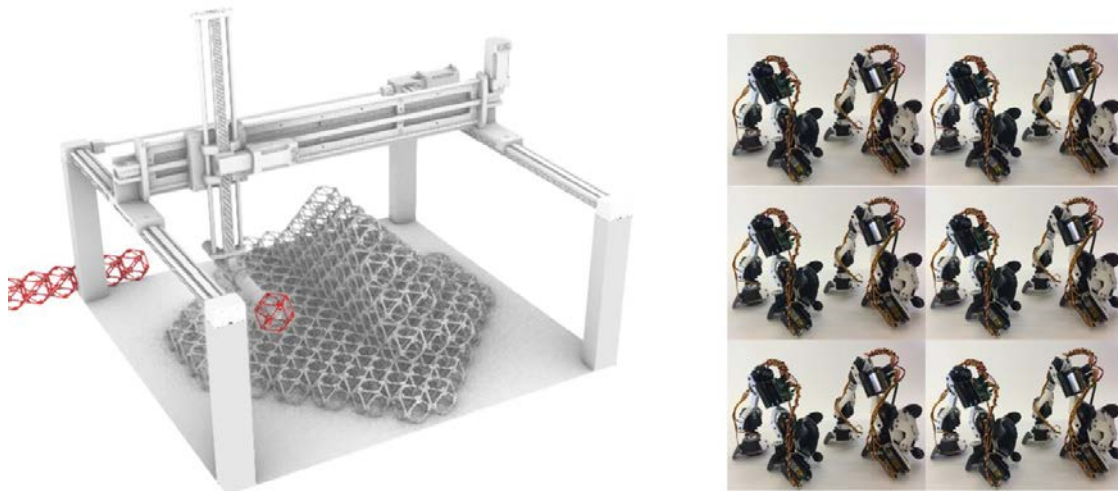
Figure 3-31: Stationary vs. Mobile platforms. (L) Low cost gantry CAD model. Rigid axes could be made as voxels. (R) Roughly equivalent cost in robots

In this section I will compare the performance of a stationary gantry with a team of mobile robots. For this I will use the following assumptions:

-Gantry cost scales relative to size
-Gantries move arbitrarily fast, the only timestep counted is assembly
-Gantries have a continuous voxel material feed

Based on this, a gantry can place one voxel per time step, and the total time for building a structure consisting of n voxels is t timesteps. For robots I make the following assumptions:

-Robots can only carry one voxel at a time
-Robots take one step per time step
-Robot must return to pick up station to retrieve next voxel to be placed
-One pickup station per robot

90

# voxels (n)	steps (t = 2n)	Total steps (n²+n)	Voxels per step
1	2	2	0.5
2	4	66	0.16
3	6	12	0.08
4	8	20	0.05
5	10	30	0.033
6	12	42	0.024
7	14	56	0.018
8	16	72	0.014
9	18	90	0.011
10	20	110	0.009

Figure 3-32: Relative robot step count increase and voxel per step decrease.

Let's look at the case of a 1x1x100 beam, where n = 100. For a gantry, this will take t = 100 timesteps.
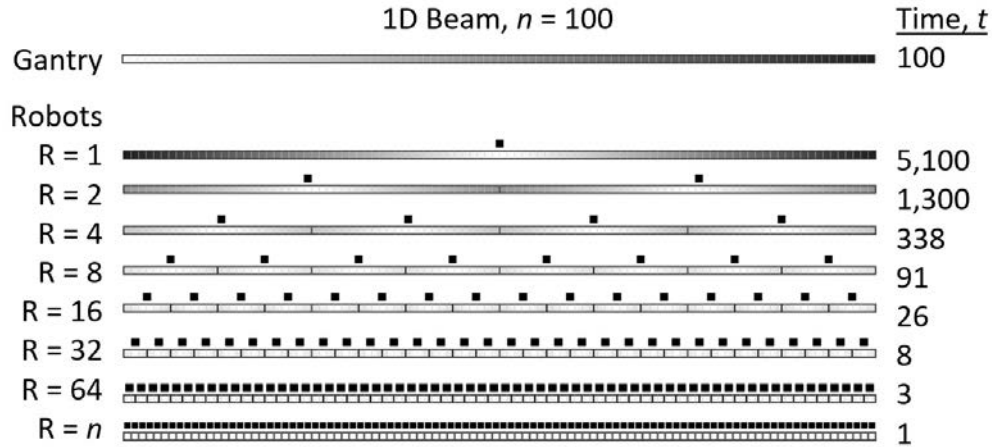
Figure 3-33: Relative robot improved throughput by parallelizing.

The robot has to return to the voxel pickup station every time, which means for every n, it takes 2n timesteps. The total timesteps for n voxels then is:

$t_{total} = n(n+1) = n^2 + n = n^2$ (for large n)

So, for the n = 100 beam, that would be:

$t_{total} = 100^2 + 100 = 10,100$ timesteps

If we divide the beam in half, so two robots each have to build a n = 50 beam, that would be:

$t_{total} = 50^2 + 50 = 2,550$ timesteps.

If there are n voxels and R robots, each robot then places n/R voxels. Because the robots work in parallel, the total time is the time for a robot to complete its section.

For a given number of robots R, we find that the timesteps as a function of n and R

91

gives:

$$t_{total} = n/R(n/R + 1) = n^2/R^2 + n/R$$

Also, we can have up to R = n robots, with some caveats. Below I tabulate some results and then plot them. We see there is a clear improvement in throughput over a single placing system:

	Gantry ($t = n$)	R = 1	R = 2	R = 4	R = 8	R = 16	R = 32	R = 64	R = n
$n = 100$	100	10,100	2,550	650	169	45	13	4	2
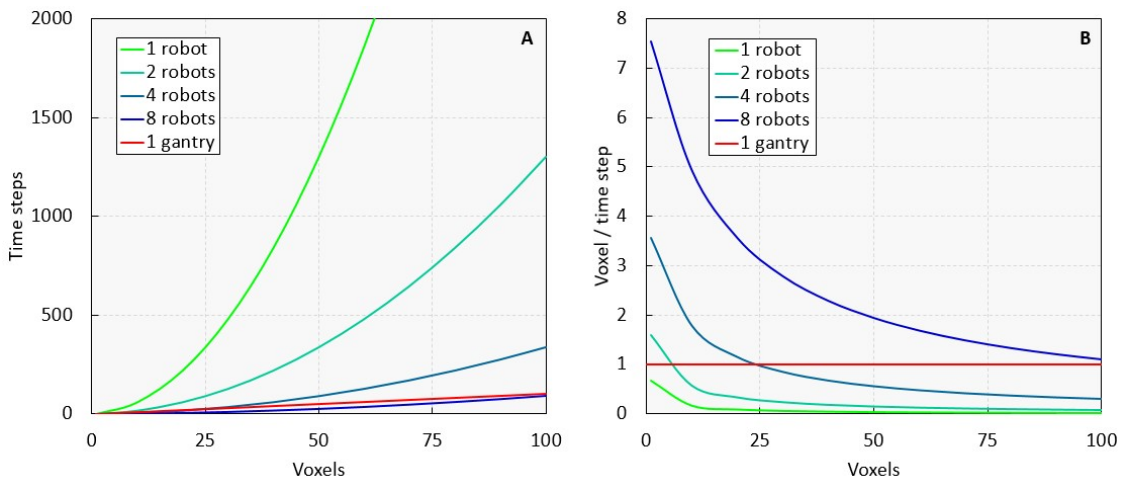
Figure 3-34: Throughput study results for 1 to 8 robots. A) voxels vs time steps, B) voxels vs voxels per time step.
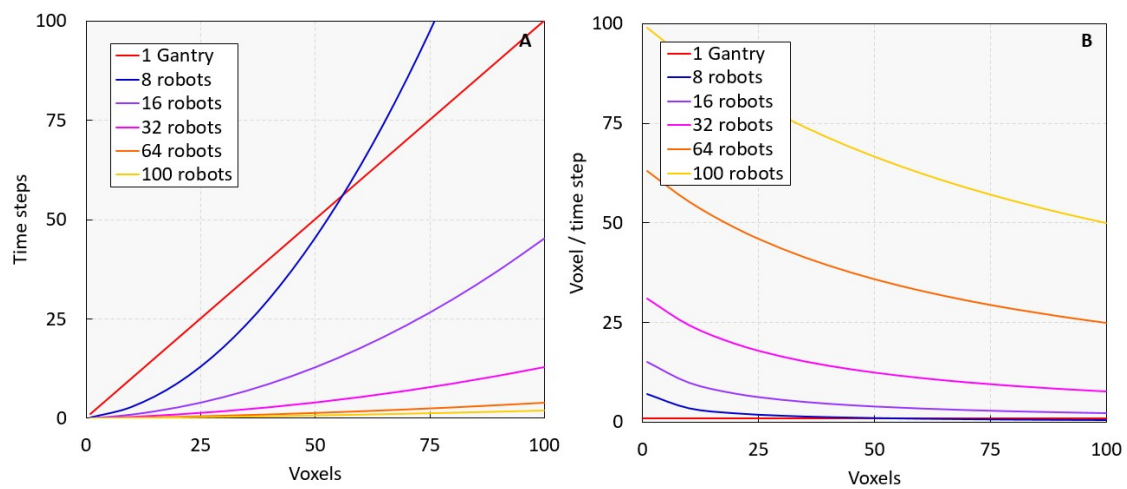
Figure 3-35: Throughput study results for 8 to 100 robots. A) voxels vs time steps, B) voxels vs voxels per time step.

3.5   Discussion

Fungible Manufacturing

Presumably for small jobs, like a car frame, a gantry can have less setup time and be an economic solution. But as scale increases, the cost of a fixed gantry increases proportional to length to the power of 1.5. So, economically, at scales over several meters, the fixed cost of a gantry might be outweighed by the benefits of a flexible, or fungible, mobile robot manufacturing system (Figure 3-36). A 1m gantry costs $10k, which affords you 10 robots, which as we saw, can actually be quite speedy when working together. Similarly, a 10m gantry costs around $1 million, which is one thousand robots, which could also be used for making something long and skinny like a turbine blade. A 100m length scale gantry costs at least $10M, if not closer to $100M, and this gets you over 10,000 robots.

At this point, since you're making something the size of an aircraft, you might as well consider having a factory full of robots. And while in Figure 3-37, the Boeing Everett factory shows dedicated lanes for making specific types of aircraft, our factory might look a bit different. The image on the top left is a simulation of a network of kiva robots in an amazon warehouse. The largest installation I believe is something like 4 floors of 2,000 robots per floor, for 8,000 robots total which is a lot, but also exactly the scale we're projecting to.
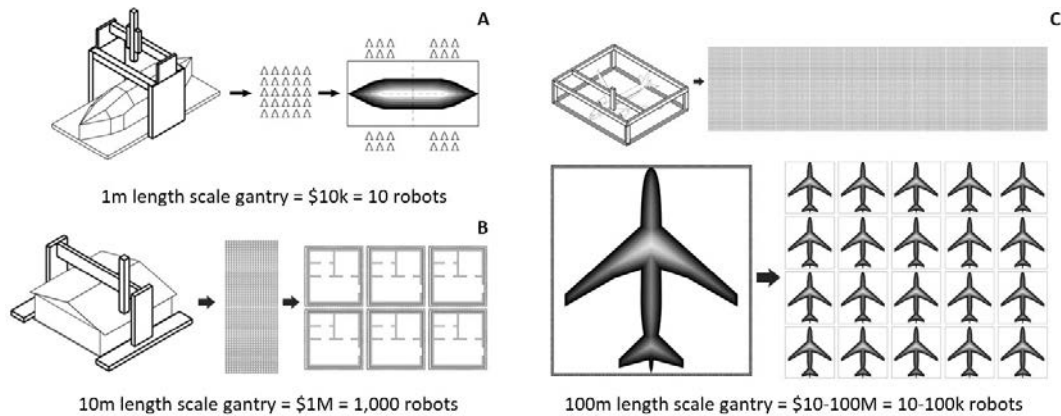
Figure 3-36: Comparison of scaling fixed gantries vs scaling fungible robot supply.
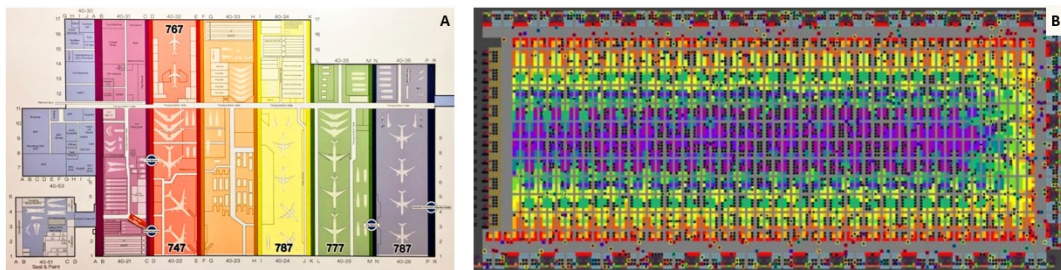
Figure 3-37: Factory organizations. A) Boeing Everett production facility [164], B) Notional amazon warehouse with simulation of Kiva robot system [165].

Scaling and recursion

With thousands of robots, scalable compilers are needed for path planning [107]. Alternatively, distributed control can use simple, finite-automata based rules to execute simple actions such as reconfiguration, which has been demonstrated experimentally [108]. Swarm robotics is another popular approach, where collective intelligence informs decentralized decision making [109], although this can be fairly sub optimal. And yet, while throwing more robots at the problem might be a solution, ultimately we're still trying to catch up with nature, where ribosomes can make ribosomes—this enables exponential construction.

While self-assembly is a popular topic in the modular robotics field, rarely does it translate to construction. One reason for this is the dissimilarity between the robot and the construction medium, which requires significantly different functions, thus significantly increasing the robot complexity. The material-robot system I presented can address this issue by making lattice-based robots, such as the inchworm platform shown in Figure 3 38. Here, voxels are used as the rigid link elements of the robot. They offer structural efficiency and impart lattice-based metrology into the robot– when both motors are at 90 degrees the robot spans exactly three voxels. While this is still a nascent topic, the ability to self-assemble will potentially enable exponential productivity in synthetic construction systems.

Finally, there is now an emerging material-robot ecosystem, where simple, modular degrees of freedom combine with various lattice types to make, for example, quadrupeds Figure 3 39 with bio-inspired gaits. At this point, the robots and structure are fully merged, and this is precisely what leads us to the next chapter on discrete systems.
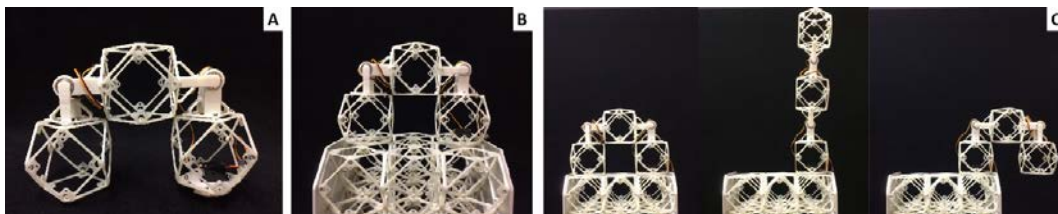
Figure 3-38: Bipedal inchworm-style voxel robot. A) VoxRob consists of voxels, motors, and end effectors, B) voxel-based length of links makes for convenient alignment with the lattice, C) locomotion based on cartwheel stepping.
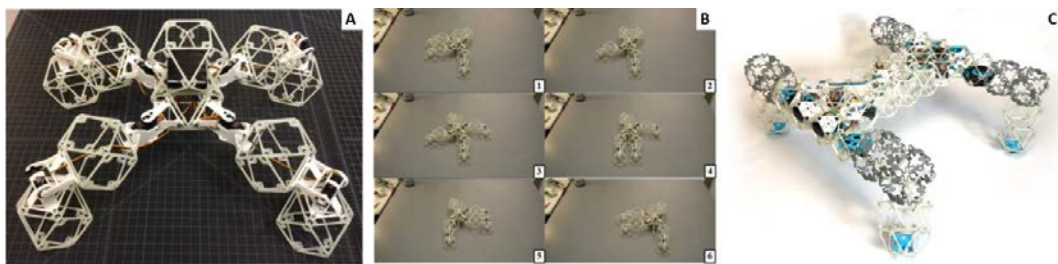
Figure 3-39: Quadrupedal insect and mammal-style voxel robots. A) Crab-bot, B) Incremental stepping gait, C) VoxDog (image and robot credit: C. Cameron).

Chapter 4

Discrete Systems

Discrete systems are application-specific engineering platforms made from discrete materials. While they share the same fundamental building-block approach, each system is different in both its external and internal conditions. Scale, geometry, and performance vary based on the application's requirements. Discrete systems include sub-systems such as structural boundary conditions or interfaces, power and actuation, and input and output sensing and communication. Modularity, scalability, and adaptability are present themes throughout.

Here I will present a total of six case studies: five built, and one unbuilt:

- **Infrastructure**: statically reconfigurable bridge

- **Ground transportation**: supermileage vehicle

- **Air transportation**: morphing, ultralight, novel geometry aircraft

- **Sea transportation**: morphing hydrostructure

- **Wind energy**: >100m turbine blade

The goal for each of these projects will be to look at how to design, build, and implement a new, lattice-based system, and then to evaluate against traditional materials and systems to point to possible wins for performance, cost, or scalability

4.1 Infrastructure

Background

Bridges are some of the oldest and most widely used engineering structures. However, today the United States' infrastructure gets a "D+", with bridges coming in at a "C+" [110]. There is much interest in low-cost, high performance, easily deployed bridge technology (Figure 4-1). One of the most successful is the "Bridge in a Backpack" project, which uses VRTM-formed CFRP arch tubes filled with concrete to span up to 15m [111]. Deployable bridges are used in disaster response and military operations, but these sacrifice structural efficiency

for deployability and tend to be quite heavy [112]. Additive manufacturing has recently been used to demonstrate both metal [14] and concrete bridges [113] on the order of 10m in length. While the ultimate vision is for robots to perform in situ construction, these are currently fabricated in a shop or factory, then transported and installed on site.

Figure 4-1: State of the art advanced bridge technologies. A) CFRP tubes which arguably can fit "in a backpack" [111], B) rigid deployable bridges [112] , C) Wire-feed metal 3D printed bridge [14], D) layer-based deposition concrete bridge [113].

Design
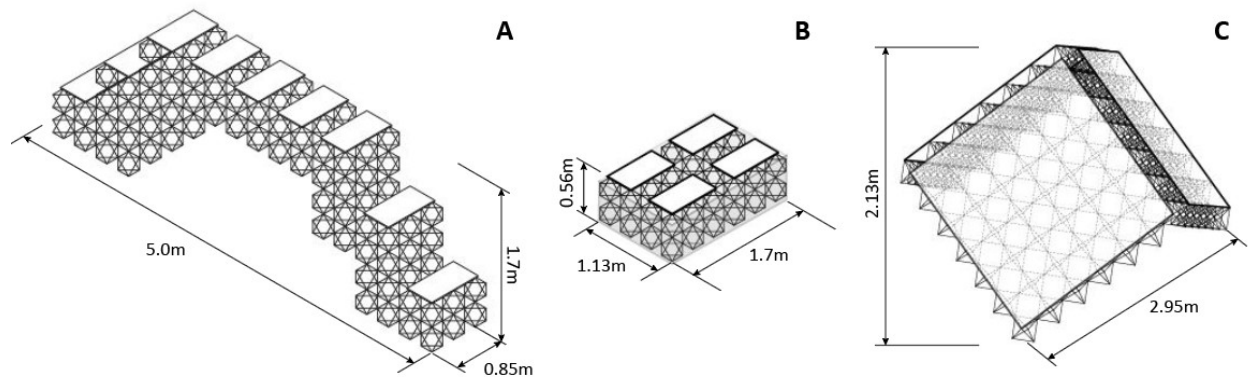
Figure 4-2: CFRP Lattice-based reconfigurable infrastructure [114]. A) Bridge, B) boat, C) shelter.

The first case study is a 5m span bridge, capable of allowing a person to walk over some obstruction (ie: a gorge). The design is based on using "macro-blocks", a 3x2x2 (12 total) voxel assembly. The design acheives a total height of 1.7m. The width is set at 3 voxels (0.85m).The final design requires 156 voxels, which weigh 17.94 kg. Plywood panels are added to give a surface to walk on. These panels (600 x 300 x 12.7mm, 9 total) each weigh appoxmately 1.15 kg, increasing the total bridge weight to 28.3 kg. These panels are bolted onto the structure. Every boundary condition (outside facing) node is also bolted, in order to ensure that boundary struts remain captive. After the bridge is built and tested, it is partially disassembled for transport. Four of the 12 voxel macro-bricks are then assembled

together to form a 1.7 x 1.13 x 0.56m boat, weighing 5.52kg. Four plywood panels served as decking, adding an additional 4.6 kg, for a total weight of 10.12 kg. A polyethylene tarp is wrapped around the bottom and attached with elastic cords across the decking. The design is based on the buoyant force required for floating the boat with two passengers (total mass = 150 kg). At a minimum, we need 0.15 m^3 displaced, and at a depth of one-half voxel (0.15m) the buoyant force generated is 0.288kg- nearly double that required to float. The last case study is a shelter, sufficiently large to stand inside of, and with a large enough footprint to provide shelter for a few occupants. Using one-voxel deep panels, a three sided shelter is designed. The shelter is skinned with mylar panels attached to boundary nodes using snap rivets.
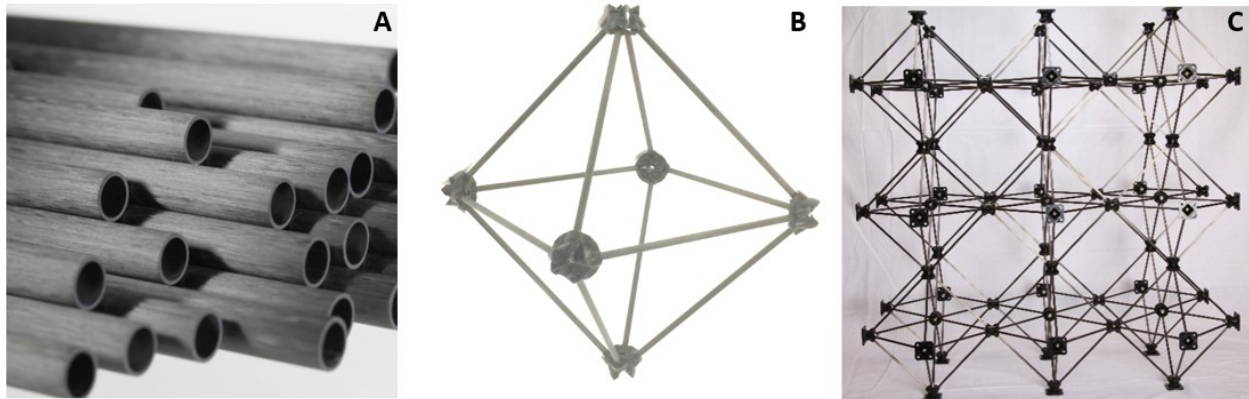
Figure 4-3: CFRP Lattice material system [114]. A) Pultruded carbon fiber tubes (image source: www.rockwestcomposites.com), B) Octahedra voxel with tube struts and injection molded nodes, C) 3x3x3 voxel cube.

Production

This projected utilized the CFRP strut and node voxels (Figure 4-3). The bridge is built by a team of four people, at a rate of 5 minutes per voxel. Constructing 160 voxels takes 3.5 hours. Assembling the voxels into the bridge takes approximately 4.5 hours, for a total of 32 person hours. It takes four people two hours to partially disassemble the bridge, and two people two hours to assemble the boat, for a total of six hours. It takes two people six hours to assemble the shelter. The entire construction process, from struts to voxels to bridge to boat to shelter, takes 50 person hours.

Performance

Aside from the demonstration of large scale assembly and reconfiguration, it was reported by Gregg that the resulting effective mechanical properties for an ultralight lattice are among the highest ever [115]. Owing to the high elastic modulus of the base material (130 GPa, unidirectional pultruded carbon fiber), the resulting lattice had effective stiffness and density values of 16 MPa and 5.1 kg/m3.
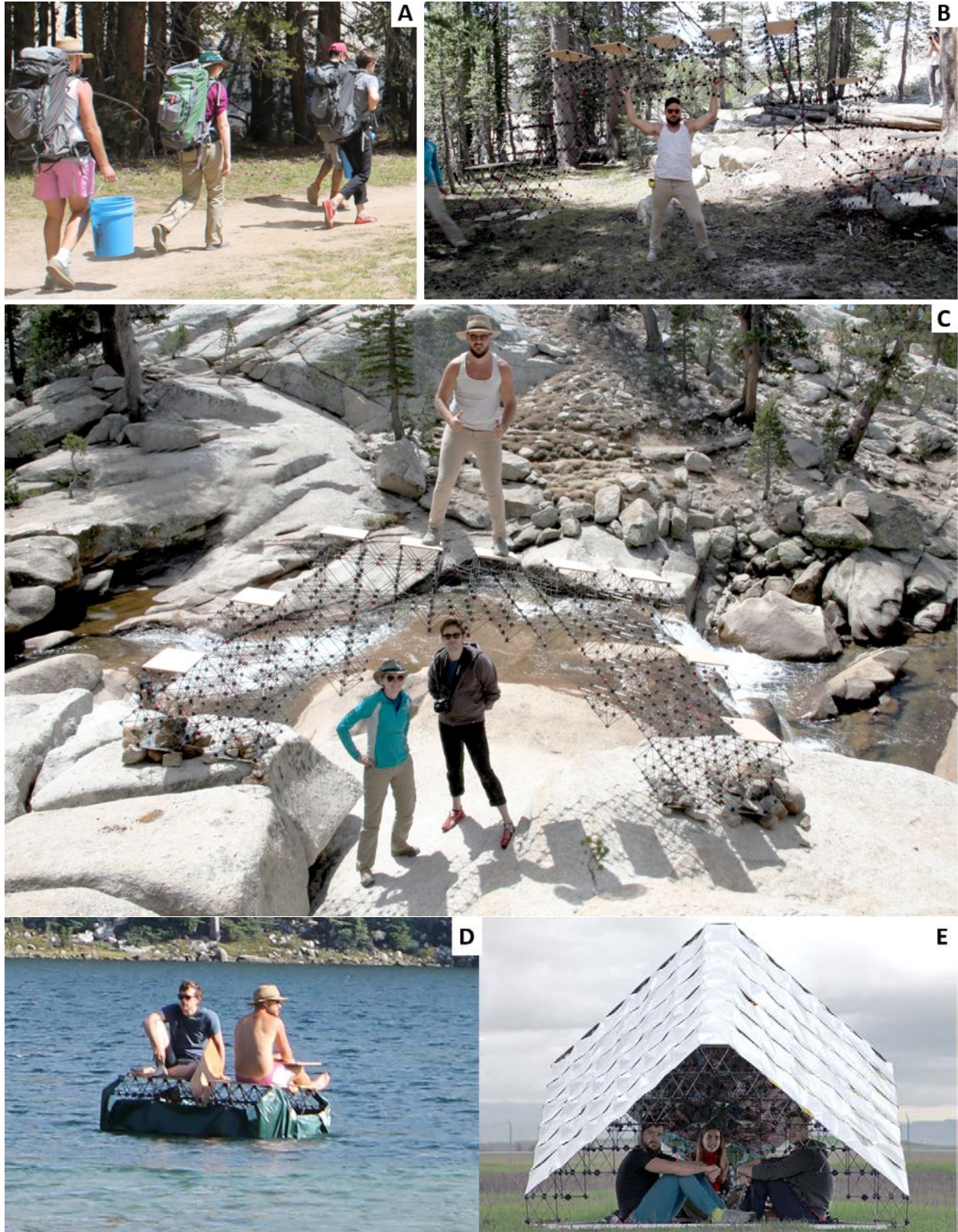
Figure 4-4: CFRP Lattice infrastructure [114]. A) Fits in a backpack, B) Ultralight structure, C) 5m bridge, D) Boat, E) Shelter

4.2 Ground Vehicles

Toyota Lattice Digital Racer (TLDR)

Note: this work was completed with Mitsuru Asai, Ken Motozawa, Takayuki Mori, and Kohshi Katoh, all from Toyota Racing Club, Japan.

Background

This project sought to apply discrete lattice assembly to the production of a supermileage vehicle. These single-person vehicles are usually custom built to have aerodynamic profiles with good structural properties. These are not representative to traditional automobiles, rather, are closer to race cars in terms of cost and performance. Their goal is to use the smallest amount of fuel to travel the greatest distance. This is typically accomplished with a combination of innovative fuel, engine, transmission, and cruising strategies, in combination with aerodynamic outer mold lines [116]. Typically, composite shells are fabricated using Vacuum assisted resin transfer molding (VARTM), which produces good results, but can be very labor, time, and resource intensive, sometimes taking up to a year to generate a design from start to finish (Figure 4-5).

Here, we sought to create an aerodynamic, high stiffness-to-weight lattice supermileage vehicle. Whereas most vehicles are composite shells attached to rigid internal frames, our vehicle would be entirely made of lattice, aside from various subsystems to provide vehicle capabilities. The strategy employed here is quite similar to [21], where a discrete material system is mass produced to build a high performance structure, then is fit with a finite set of interface parts and skin elements to form an outer mold line. Here I will describe the design process, the production and assembly, and testing results. Then I will expand the discussion to consider applying discrete lattice assembly to the manufacturing of commercial car frames, using a techno-economic analysis to compare to traditional approaches.
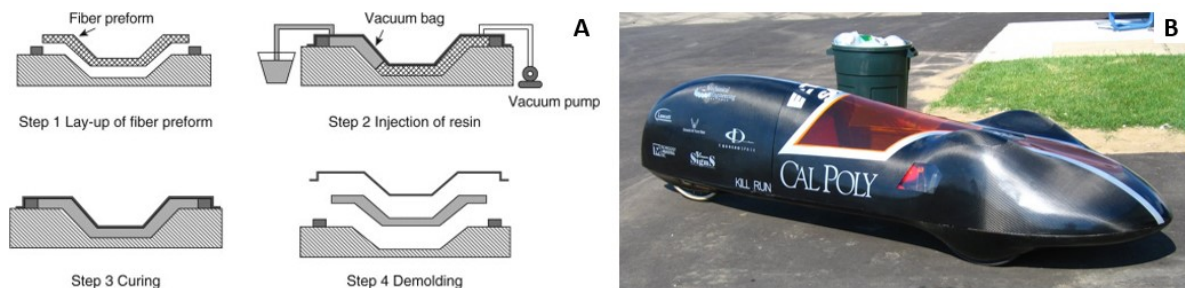
Figure 4-5: Composite monocoque manufacturing for supermileage vehicles. A) Vacuum assisted resin transfer molding (VARTM) [117], B) example vehicle [118]

Design

The evolution of the outer mold line is shown in Figure 4 6. The initial geometry began as a generic ellipsoid, then shifted more towards a 0024 NACA airfoil. The final, faceted geometry is made up of 1:1, 2:1, and 4:1 slopes, and also provides space for vehicle subsystems like the motor, steering, and seating. CFD studies were performed to determine the coefficient of drag of this geometry, with qualitative drag coefficient contour plots shown over the geometry in Figure 4 6D. Simulations were performed in COMSOL Multiphysics by Filippos Tourlomousis. The total drag coefficient for the current TLDR design is 0.16. The results are promising showing us that we are in the light-weight fast car regime (typical drag coefficients).
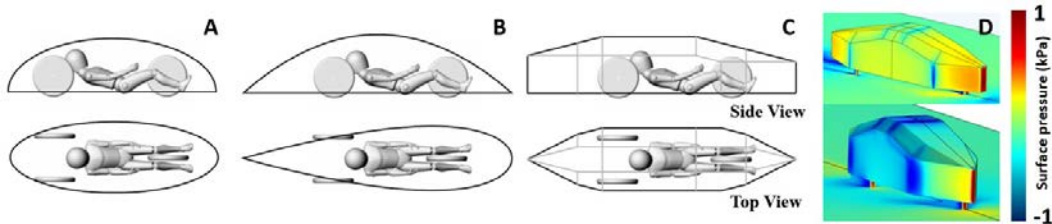
Figure 4-6: TLDR outer mold line development. A) Initial ellipsoid, B) NACA 0024, C) resulting faceted geometry, D) CFD studies of faceted geometry drag (image credit: Filippos Tourlomousis).

Following this, the structural lattice design began using specifications from Toyota, which were a first natural frequency greater than 30 Hz, and a frame mass under 20 kg. Using NASATRAN in Fusion's modal frequency simulation tool, the frame body was modeled as a monolithic entity, and a range of the possible effective stiffness and density parameters were input. The results are shown in Figure 4-7 and Table 7. Given the mass overhead of skin and skin attachment components, the lattice with $\rho^* = 20$ kg/m^3 was selected. Upon deciding the lattice pitch (75mm, based on various studies on part count vs. surface curvature resolution), the volume could be filled with lattice, and simulated with quasi-static loading conditions using beam thickness and material properties based on the aforementioned modal study.

Table 7: TLDR Lattice study results

Effective lattice density, ρ^* (kg/m³)	Effective lattice modulus, E^*(GPa)	First natural frequency (Hz)	Lattice volume (m³)	Lattice mass (kg)
10	0.01	33.37	0.65	6.5
20	0.05	52.67	0.65	13
30	0.1	60.92	0.65	19.5
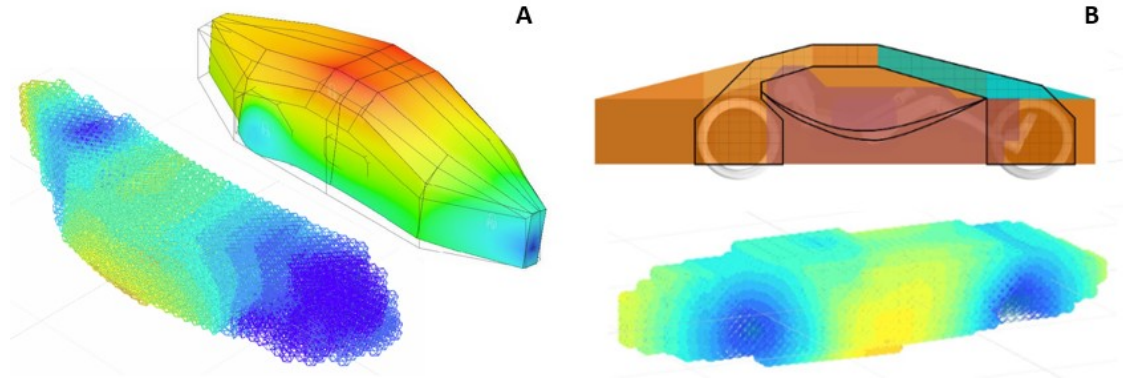
Figure 4-7: Preliminary simulation studies for TLDR. A) modal response and B) quasi-static deflection with driver mass suspended from seat mounting locations.

Production

The general assembly strategy is shown in Figure 4-8, where the lattice is assembled layer by layer while integrating subsystems such as wheels and motor, followed by the skin frames and finally the outer mold line (skin and windows). The lattice was produced first as 1,069 individual voxels. Then, vertical layers were assembled from rear to front. Using the established metric of 4.5 minutes per voxel, which includes individual voxel construction time and subsequent lattice assembly, the entire frame took approximately 80 hours to assemble, which was split between multiple people. This time is useful when considering the effectiveness of this approach: a similarly sized monocoque composite shell may take several times as long to produce.

Following the design of the lattice, voxel, and face parts for molding and mass production, an array of subsystems were designed to provide all the additional functionality for the vehicle, such as the motor, axles, wheels, seat, windows, and skin. The majority of mounting points for external hardware used aluminum plates with hole patterns which matched the lattice hole pattern.
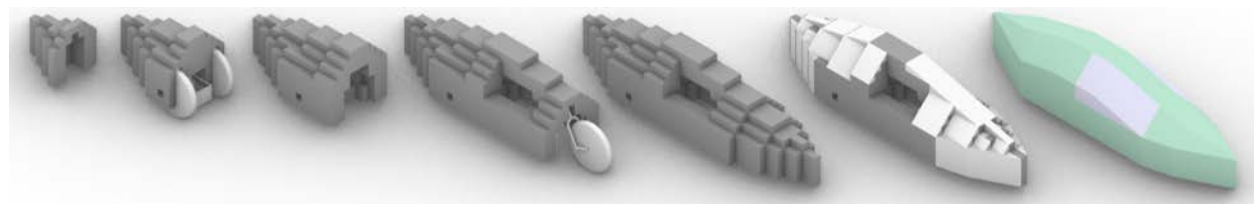
Figure 4-8: TLDR build sequence. Layers were built individually then added up in following the sequence as shown.
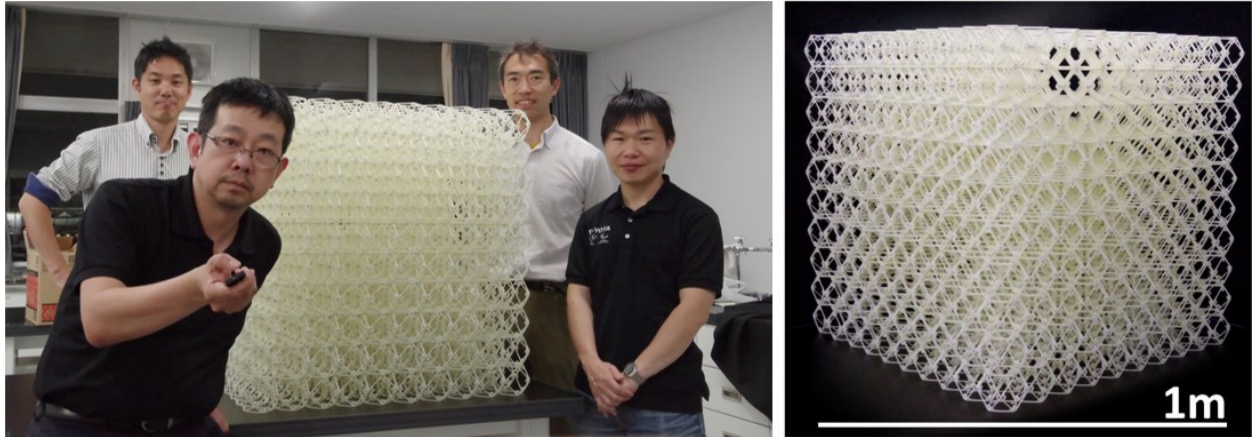
Figure 4-9: Lattice production. Part of the Toyota Japan team, after completing assembly of 1000 voxels. L to R: Mitsuru Asai, Ken "No Mercy" Motozawa, Kohshi Katoh, Takayuki Mori (Driver).

Figure 4-10: Completed lattice car frame.
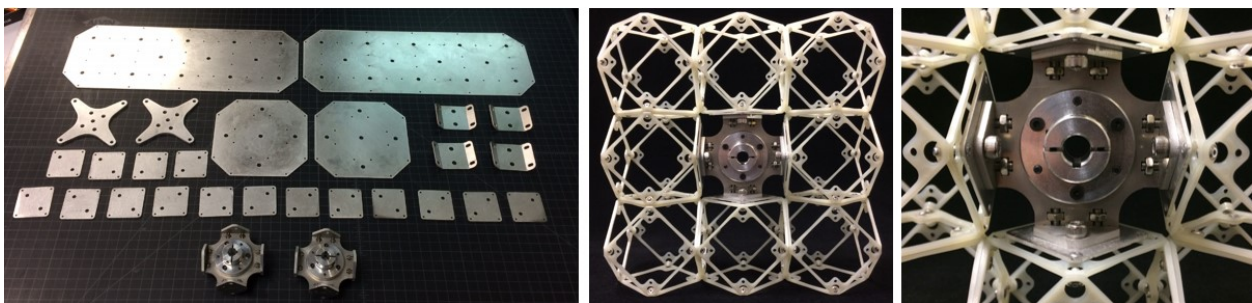
Figure 4-11: Plates and hubs. Waterjet, lasercut, folded, and bolted aluminum plate to make mounting plates for engine, seat, and hubs for axles.
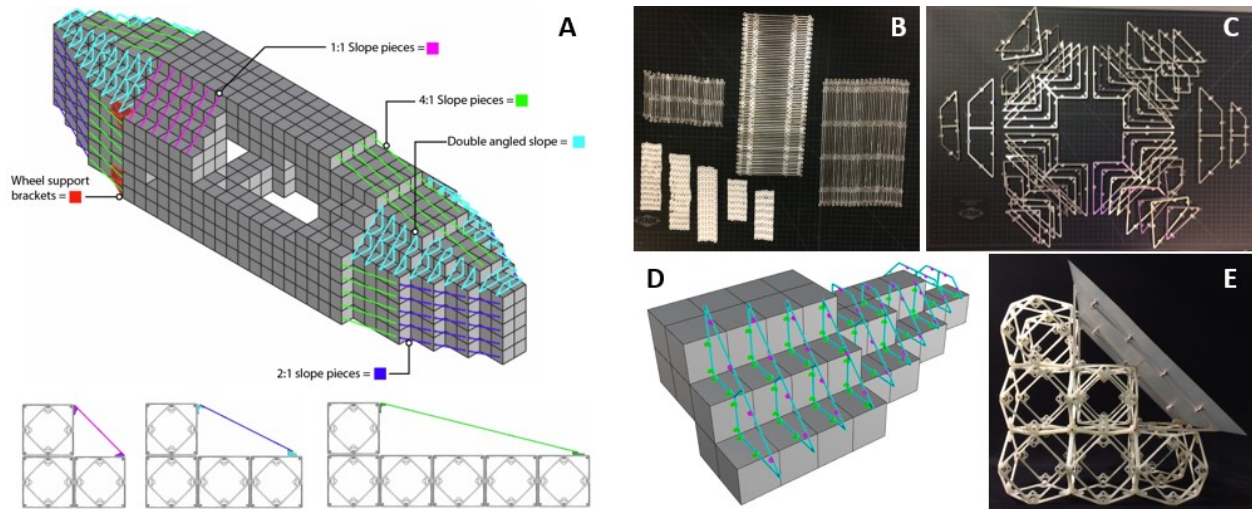
Figure 4-12: Skin support system. A) System overview with color coding indicating 1:1 (magenta), 2:1 (blue), 4:1 (green), and double angle slope parts (cyan), B) Single-angle slope parts consisting of lasercut aluminum beams and 3D printed end attachments to set angle and mount to lattice, C) Lasercut aluminum with folded aluminum tabs to describe double-angle slope surfaces, D) Diagram illustrating double-angle slope system with 90 degree tabs to mount to lattice (green) and custom tabs to set surface angle (magenta), E) mockup of a section of double slope system.
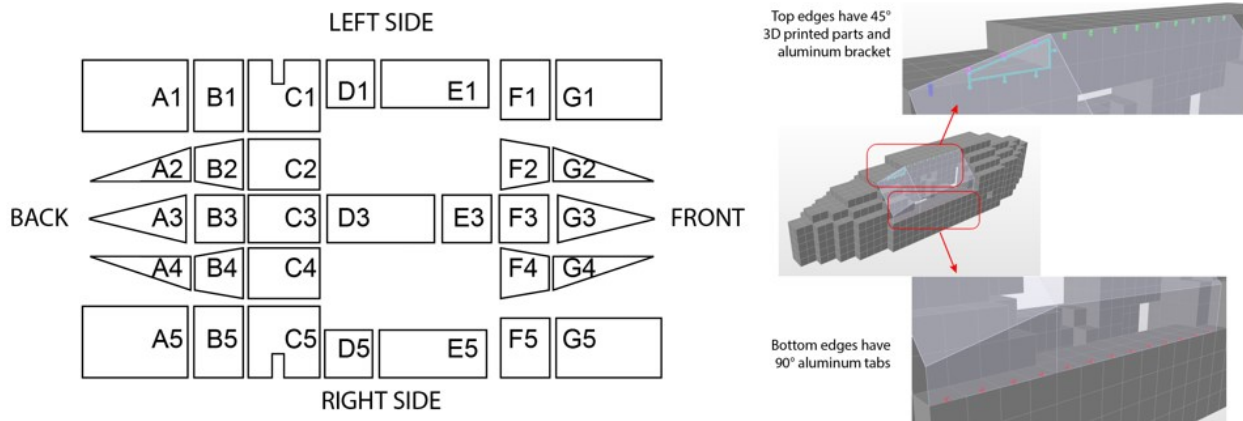
Figure 4-13: Skin and windows. (L) Skin was cut from 0.005in thick GFRP sheet, (R) Windows were cut from polycarbonate sheet and folded using a brake press.
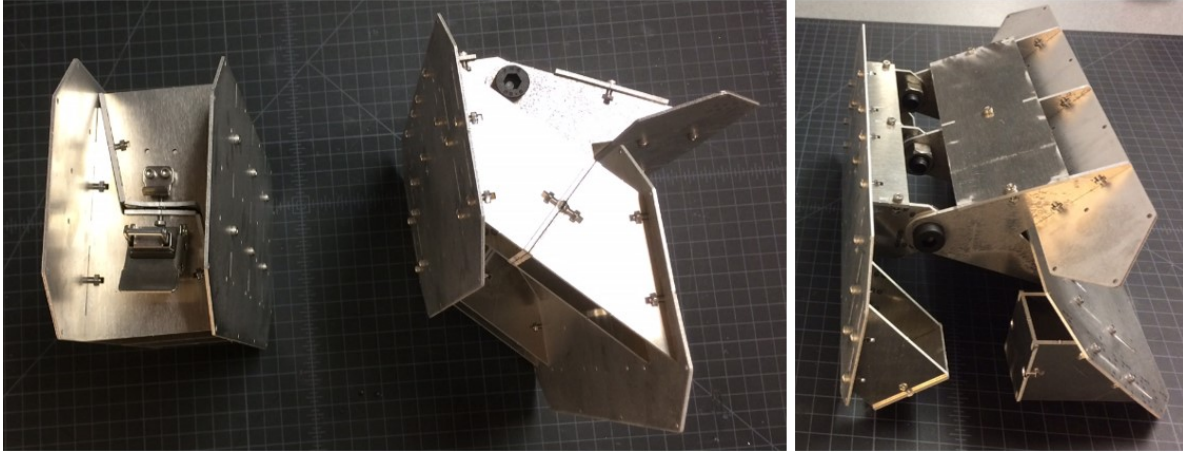
Figure 4-14: Roof opening hinge and latching mechanism. Waterjet aluminum with air-spring loaded piston and double-safety locking latch system.

Figure 4-15: Driver entrance and preliminary vehicle testing.

Performance

The completed vehicle is shown in Figure 4-16. There were two takeaways from the race. One is that the driver reported the car performing well, especially in its ability to dampen vibrations from the road. The mechanisms for this may be explained in looking at the second takeaway: the car collided head on with a padded barrier and was undamaged (driver was undamaged as well). In effect, this was an (unplanned) in situ dynamic impact test. This is not only a topic of active research within the metamaterial community [119][120], but it suggests some potential applications within the automotive industry, such as bumpers or protective regions around battery packs in electric vehicles.

Assuming the lattice shows continuum behavior, which we showed it does, then the current explanation is that the entire lattice vehicle deformed as a monolithic, elastically deformable solid. This means the front impact region was able to transfer the load which propogated through the vehicle, which likely would not be possible without continuum be-

havior. Given this, our next step is to perform a controlled impact test. We will instrument the vehicle as well as record video with high speed, in order to capture any phenomena with a very fast time scale. Further, static drop impact tests can be performed to compare the response of different metamaterial types, with a high likelihood that a new voxel type for energy absorption or energy return will be designed and tested.
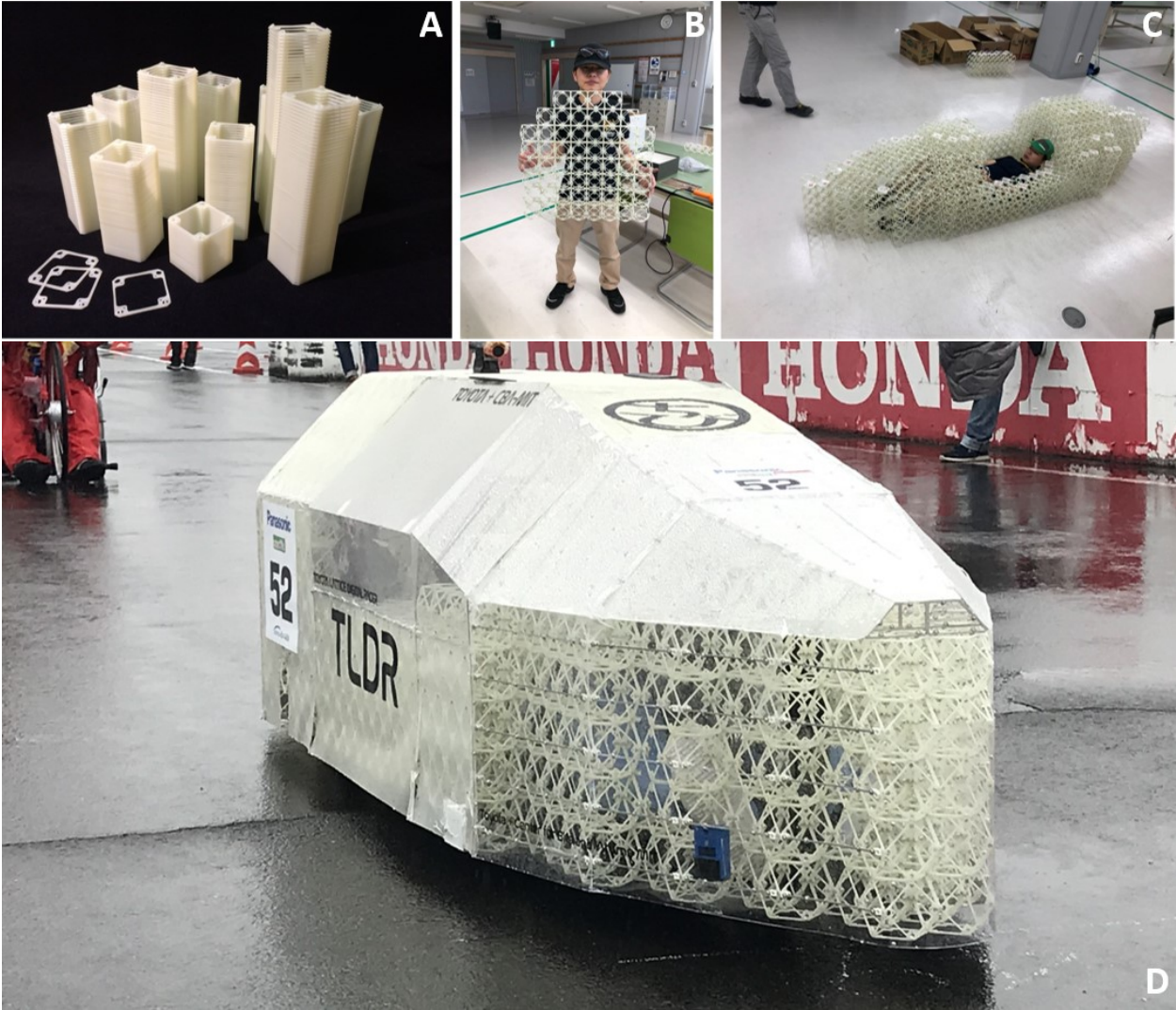
Figure 4-16: TLDR vehicle in testing and race conditions. Image credits: Toyota Automotive Society

4.3 Air Vehicles

Aircraft structures have been incrementally refined for decades, relying heavily on high performance metal alloys for performance and ease of construction. More composite material is being gradually integrated, while overcoming myriad cost and manufacturing challenges. Aircraft geometries stray very little from the "tube with wings" motif, primarily due to the heavy reliance on legacy as a basis for cost, safety, and performance risk reduction. However, the performance of non-traditional aircraft has been studied extensively. One such design, the blended wing body (BWB), has been shown to offer significant improvement in fuel efficiency over traditional aircraft [121]. Yet its geometry essentially makes it a non-starter, due to the cost-sensitive and risk-averse nature of the airline industry. Perhaps equally well studied is the use of morphing structures, which allow shape change to optimize performance [122]. To date, few designs have flown at scale [123].
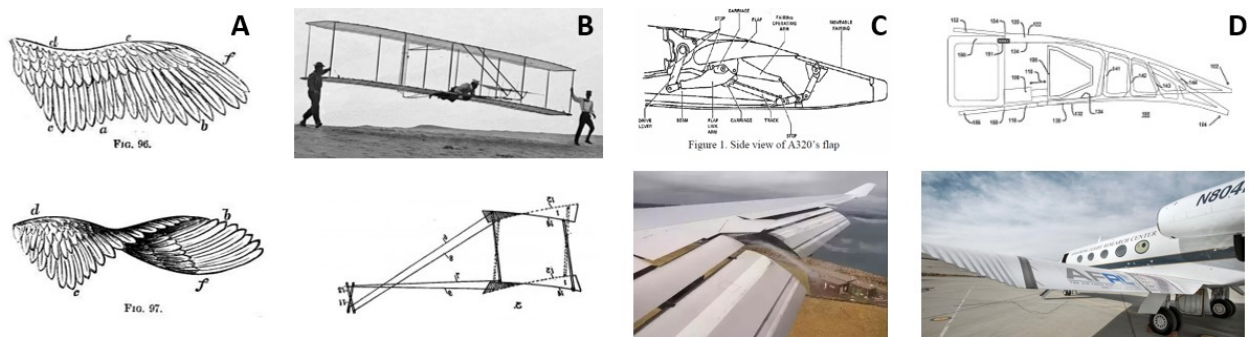
Figure 4-17: Morphing wings. A) A bird's wing demonstrating continuous deformation [166], B) The Wright brothers used tendons to achieve wing twist [166], C) Traditional rigid control flaps require heavy mechanisms [167], D) Flexsys technology uses internal flexures to control a morphing trailing edge [123].
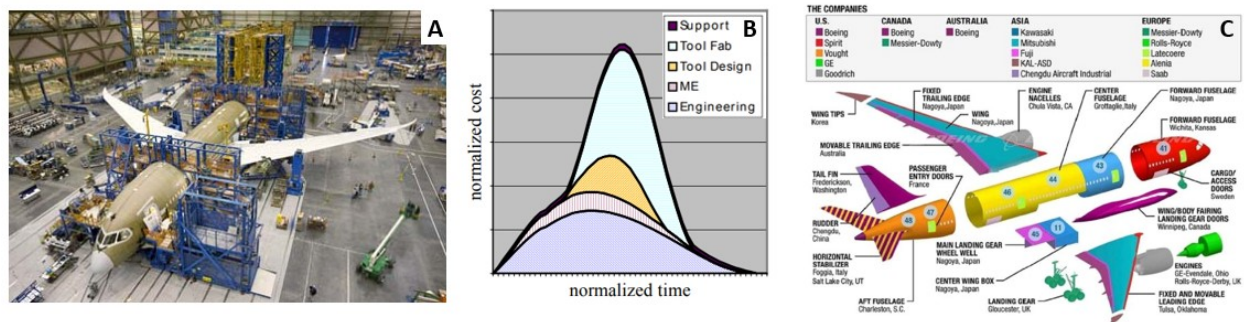
Figure 4-18: Aircraft manufacturing constraints. A-B) Fixed geometries [169] help amortize fixed up-front costs for tooling [124], C) Global supply chains have led to long lead times and bottlenecks [168].

MADCAT

The Mission Adaptive Digital Composite Aerostructure Technology (MADCAT) program was a collaboration between NASA, MIT, and several other institutions to investigate the application of discrete lattice materials to aircraft. The program resulted in two versions of aircraft, MADCAT v0 and v1.

Here, the application of discrete lattice assembly in aerostructures seeks to address two issues: adaptive performance and manufacturing constraints. The former leverages the spatial programmability of discrete lattice construction to achieve anisotropic behaviors for controllable shape morphing, the latter leverages best-practice manufacturing and "tooling free" assembly to realize user-defined aircraft geometries which would be considered prohibitively expensive to make using traditional manufacturing techniques.

MADCAT v0

Note: work shown in this section was completed in collaboration with Nicholas Cramer, Sam Calisch, Daniel Cellucci, Sean Swei, and Kenneth Cheung. It is published in [125].
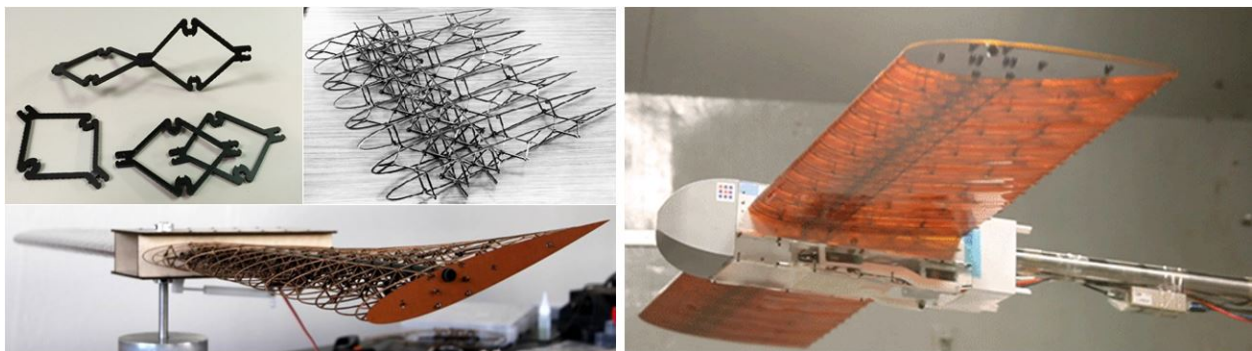
Figure 4-19: MADCAT v0 [125]. A) Waterjet CFRP lattice elements are connected to form lattice airfoils with anisotropic properties. B) The resulting morphing aircraft undergoing wind tunnel testing.

In [125], we presented a 1m scale discretely assembled aerostructure with programmed anisotropy for application as a morphing wing. Here, heterogeneous lattice geometries are combined to result in a structure that is stiff in bending but compliant in torsion, allowing tip twist actuation and global shape change for roll control with reduced drag. The NACA 0012 outer mold line was achieved using highly customized parts, reducing the utility of this particular system for other geometric configurations (Figure 4-19).

Parts are produced by abrasive waterjet cutting them out of 1.5mm thick CFRP quasi-isotropic laminate with elastic modulus E = 30 GPa. The resulting stretch and bending-dominated lattice geometries have effective moduli of 1 GPa and 0.02 GPa, respectively. Parts are joined with flexural snap fit features or are fixtured with zip ties. While this allowed rapid assembly (8 hr assembly time), these joints do not provide sufficient load capacity to be deemed fully structural, though this is not an issue due to the relatively small

loading experienced by the structure. Chordwise skin strips are able to slide relative to one another, which allows continuous deformation when a spanwise torque tube provides tip twist via a servo with a linkage to augment output torque, which is housed in the fuselage.

In wind tunnel testing, the morphing wing demonstrated the ability to generate roll and yaw moments through asymmetric twist and showed that a 6° twist generated a roll coefficient comparable to a 10° flaperon deflection. Afterwards the wings were mounted to a custom built fuselage and tail section with propeller and RC control. This aircraft was flown in an outdoor flight space and successfully demonstrated good control authority of twist for roll maneuvering in a real world environment [126].

MADCAT v1

Note: work shown in this section was completed in collaboration with Nicholas Cramer, Daniel Cellucci, Olivia Formoso, Christine Gregg, Joseph Kim, Martynas Lendraitis, Sean Swei, Greenfield Trinh, Khanh Trinh, and Kenneth Cheung, and it was published in [21]

Figure 4-20: MADCATv1 [21]. (A) Modular building block unit, (B) 4x4x4 unit cube during mechanical testing, (C) Single half-span wing structure composed of 2088 building block units, (D) Blended wing body aerostructure with skin, mounted to central load balance in the 14x22 subsonic wind tunnel at NASA Langley Research Center.

The aircraft is designed as a low speed BWB-style geometry [121]. Preliminary root bending moments informed overall scale as a function of lattice strength and linear elastic stiffness, and further iterations used wing sweep to augment pitch stability and dihedral to improve lateral stability. From a CAD model, two aerodynamic simulations (xFoil for airfoil pressure distribution and vortex lattice method for lift coefficients) provided loading for a FEA simulation performed in ABAQUS to verify deflection and stress factors of safety.

As shown in Figure 4-20, the lattice structure is made from the injection molded vertex connected octahedra. It is then decorated with skin interface parts and skin panels. The

lattice was assembled in a programmed manner, where rows and columns of voxels were pre-assembled then attached in layers moving away from the root, which is quite similar to rastering. The tooling for a high temperature GFRP resin was used for a lower temperature Nylon, which has a different shrink rate. This caused a discrepancy between these parts, but it was determined to be consistent, such that we could use the size difference as a pre-strain to program spatial anisotropy. In this case we applied inboard camber morphing, tip dihedral, and tip twist, all by making a specific checkerboard pattern with the two part types. Our designs were simulated to validate behavior before construction.

Wind tunnel testing of both wing versions took place in the NASA Langley 14'x22' wind tunnel. After running baseline tests with the homogeneous model, we tested the passive and active heterogeneous model, which showed several combined morphing modes, and improved L/D ratio over the baseline design.

VoxThor

VoxThor is an ongoing project looking at leveraging the previously described projects and combining their benefits to produce a fully morphing, lattice-based UAV (Figure 4-21).
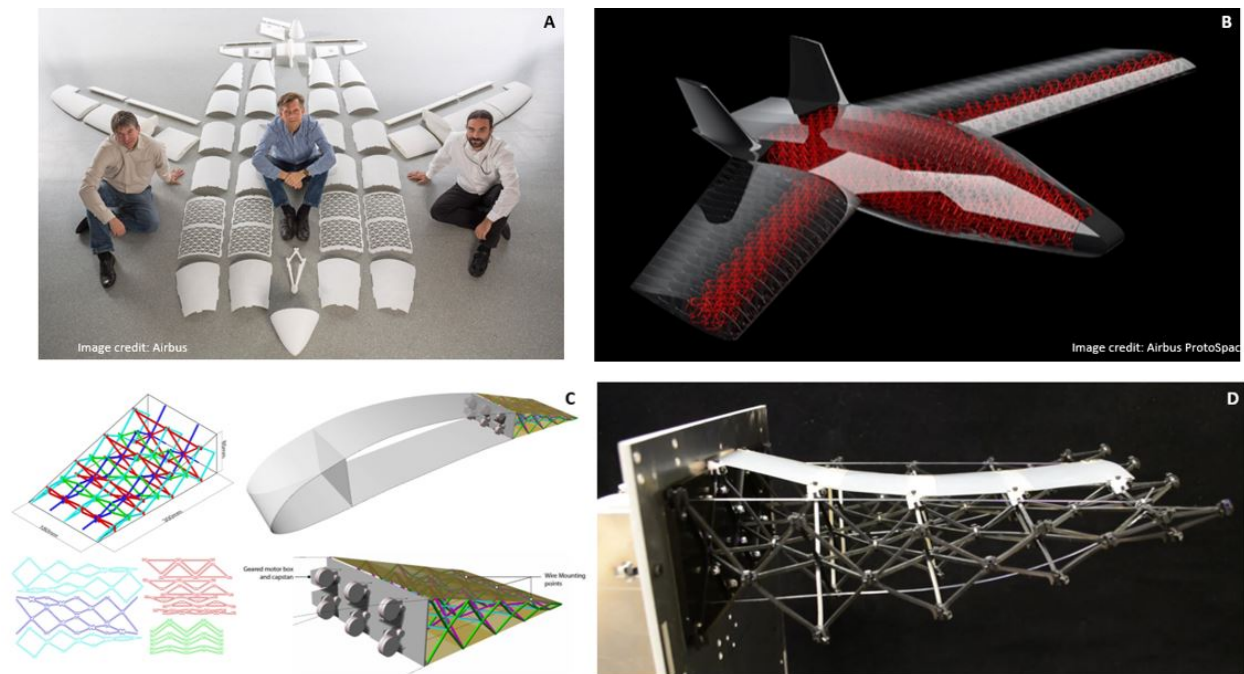
Figure 4-21: VoxThor A) Original THOR project with 3D printed components (image credit: Airbus), B) Concept image for VoxTHOR (image credit: Airbus Protospace Madrid), C) Morphing trailing edge and tail elevator CAD, and D) Functioning prototype.

Here I look at applying tailorable cellular materials to make morphing aerostructures for use in commercial aircraft control flaps. Chordwise airfoil morphing can be used to control trailing edge geometry for improving lift to drag ratio, or for roll control authority, with potential for improvement in fuel efficiency [127]. The trailing edge is a triangular

cross section, 300mm deep, 80mm high, and 8m long. Objectives for this project include a low-cost, scalable manufacturing method which can utilize high performance CFRP and comparing distributed and centralized actuation systems. The method employed here is similar to [125], where a uniform lattice geometry is modified to fit into an airfoil section, and then decomposed into intersecting planes (x, y, z), which are then waterjet cut from quasi-isotropic CFRP sheet. Press fit joints between members constrain 5 of 6 DoF, with the last degree being taken up by a zip tie.

The proposed skin system is discretized chordwise into strips that overlap slightly, from leading to trailing edge. These strips span a single lattice pitch in the chordwise direction and are fixed to the lattice with shoulder bolts which screw into custom threaded components that sit atop the lattice nodes. These bolts pass through chordwise slots in the trailing edge-side of each strip, constraining in the direction normal to the strip surface, but allowing it to slide relative to the bolt, thus allowing outer mold line chord length to change passively while maintaining a continuous aerodynamic surface. Morphing is achieved using a pair of cables that attach at one end to a lattice node at the trailing edge, and at the other end is fixed to a drum/spool mounted to a motor. Thus, with a single degree of actuation, the trailing edge tip can be deflected up or down through clockwise or counterclockwise rotation of the drum. This applies a tensile force in one of the cables, pulling the tip towards the leading edge, and slightly up/down, which, due to the lattice geometry, results in a global shape change of the lattice substructure, as shown below. A proof of concept prototype has been built using Delrin for the lattice material and high torque COTS servo motors for distributed actuation. The future work for this application includes fabricating a high-fidelity CFRP version and actuation selection.

4.4 Hydrostructures

Note: work shown in this section was completed in collaboration with Dixia Fan, Alfonso Rubio Parra, Chris Cameron, Jiri Zemanek, Filippos Tourlomousis, Megan Ochalek, and Michael Triantafyllou.

Background

Soft robots offer adaptability and resilience for manipulation and control through a balance between compliance and stiffness, with continuous deformations in contrast to rigid mechanical systems. Despite these benefits, soft robots have faced inherent challenges associated with their use of soft materials, including limits on the loads that they can support, issues with their scalability, difficulties in integrating heterogeneous system properties, a requirement for production tooling, and the need to actively maintain static configurations.

We present a novel method to construct cellular soft robots that can address these constraints by discretely assembling mechanical metamaterials. By combining two simple regular part types (rigid and compliant) we show that we can design high-performance anisotropic structures. Combining these with distributed actuation results in actively deformable robotic systems. We demonstrate the utility of this approach in a novel application as a continuously deformable cellular hydrodynamic soft robot based on bio-inspired swimming motions (Figure 4-22). We describe the design, fabrication, control, and testing of this 1.5m snake-like robot in a tow tank and show that traveling wave kinematics can be used to generate thrust while maintaining low drag through the continuous deformation of the cellular structure.
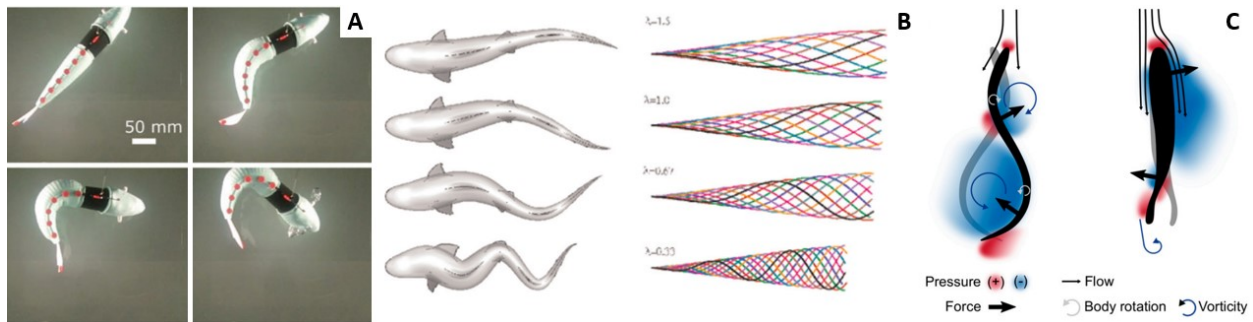
Figure 4-22: Bio-inspired motion for aquatic thrust generation. A) Soft robotic fish for escape maneuvers [132], spiny dogfish kinematic equations [133], airfoil-like mechanics generate thrust on the anterior body of swimming fishes [134].

Design

First, I present the construction system for our discrete lattice materials. Rigid (grey) and compliant (purple) parts are manufactured the same way—injection molding of GFRP. They are then assembled into voxels (Figure 4-23), and then into lattice. When assembled, these behave as continuum mechanical metamaterials with distinct properties (in this case, rigidity and compliance). Their application as stiff and soft areas on novel robotic platforms is shown conceptually in Figure 4-23D. Quadrupeds need joints connecting relatively stiff limbs. Flying requires low effective density, while maintaining sufficient stiffness to withstand aerodynamic loading while generating lift. Adding compliance enables dynamic shape change. Swimmers perhaps most of all benefit from globally deformable structural systems, where the entire body of a fish or eel contributes to both propulsion and drag reduction.

The lattices shown have the same lattice pitch p, are the same relative density, and are made from the same material, yet they have an order of magnitude difference between their effective moduli. The rigid lattice has an effective elastic modulus E* of 8 MPa, an effective Poisson's ratio of 0.15, and an effective density of 30 kg/m^3. The compliant lattice has an effective elastic modulus E* of 0.1 MPa, an effective Poisson's ratio of 0.1, and the same effective density. Using these two lattice materials together for controllable anisotropy through heterogeneous lattice design will enable large scale morphing structures to be built quickly. Because beams have the same geometry, specifically, length L, effective cross-sectional area A, and effective second moment of area I, I expect their structural behaviors to have a relationship governed by the effective moduli of their respective lattice types. To investigate this, I characterize their axial and bending stiffnesses.

I performed linear elastic compression tests to calculate the axial stiffnesses. The results are shown in Figure 4-24. The axial stiffnesses of the compliant and heterogeneous beams are 11% and 44% of the rigid beam, which demonstrates the effect of heterogeneity by producing a value between the two constituent homogeneous values. I then performed linear elastic tip deflection tests of the beams as horizontal cantilevers to calculate their bending stiffness. The results are shown in Figure 4-24. The bending stiffness of the compliant beam is 13% of the rigid beam. which indicates good correlation between effective stiffness E* governing the relationship. I test the heterogeneous beam in both compliant and rigid directions and find that the bending stiffnesses are 19% and 74%, respectively. So, while the axial stiffness is roughly centered between the two homogeneous values, the bending stiffness is strongly anisotropic as a result of the heterogeneity. This heterogeneous, anisotropic beam forms the basis for our discrete cellular soft robotic system, which will now be described.
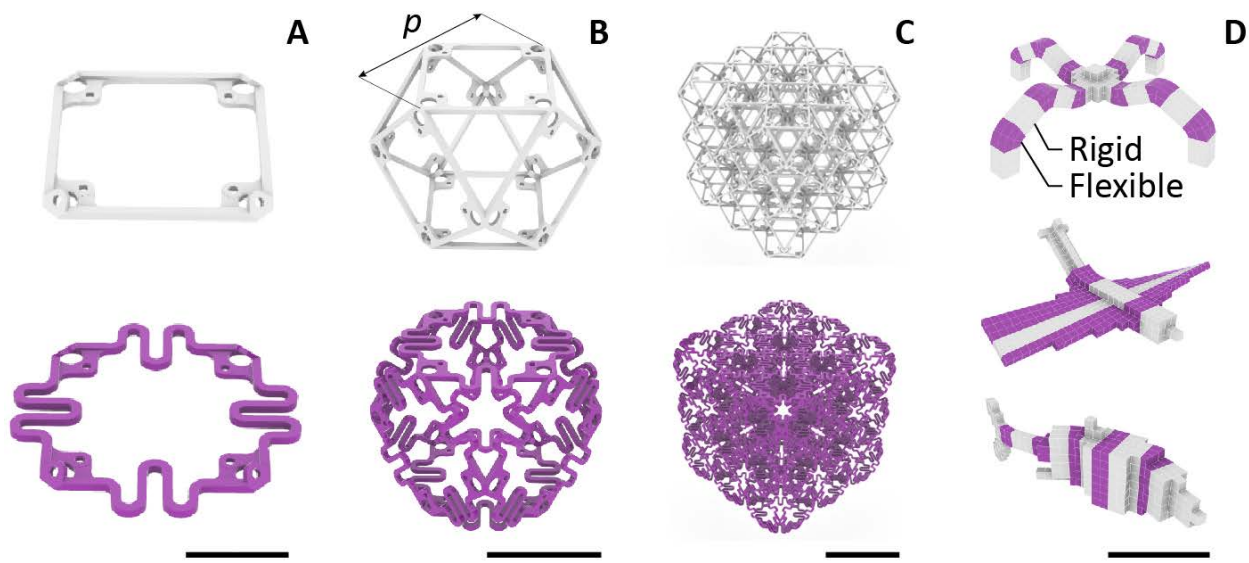
Figure 4-23: Heterogeneous discrete lattice material system. A) Rigid (grey) and compliant (purple) faces, B) rigid and compliant voxels with lattice pitch p = 75mm, C) Rigid and compliant 3x3x3 lattice cubes, D) Concept art of discrete cellular soft robots for walking, flying, and swimming. Scale bars: A) 25mm, B) 50mm, C) 100mm, D) 750mm
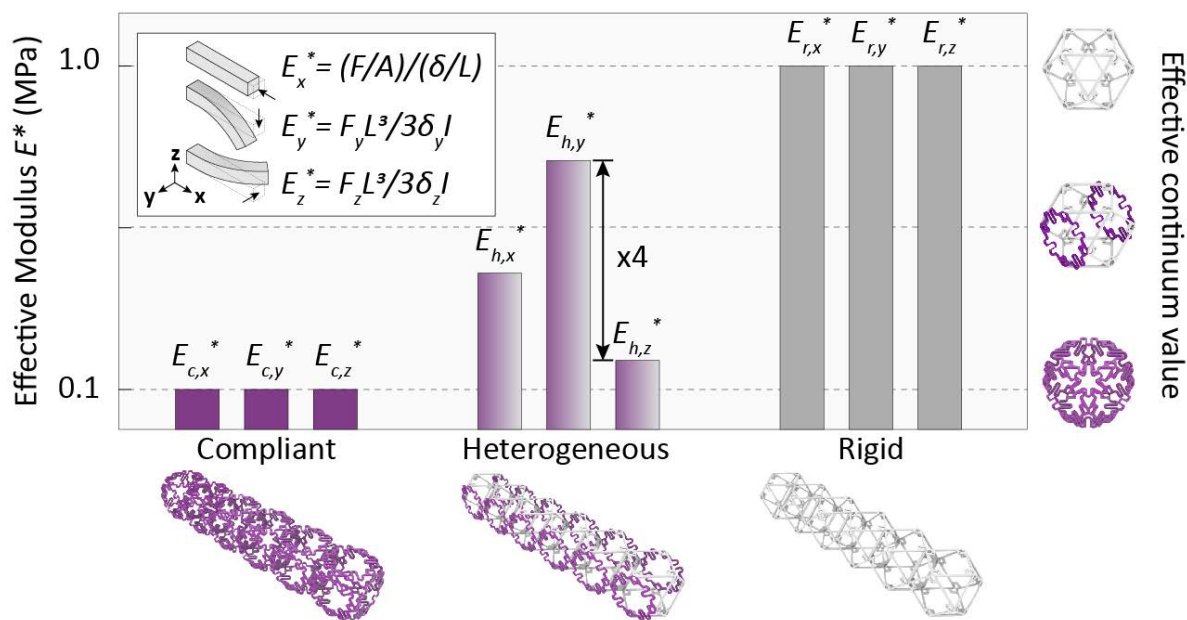
Figure 4-24: Comparison of effective axial (x) and bending (y, z) modulus for compliant, heterogeneous, and rigid beams, measured experimentally on 6x1 beams.

Performance

Following the design of anisotropic beams, we introduce actuation to control the deformed shape of the beam. The beam module consists of a rigid voxel followed by four heterogeneous voxels (Figure 4-25A). A servo is mounted inside the rigid voxel, with two cables extending to the end of the heterogeneous section. The servo is aligned such that rotating clockwise or counterclockwise will translate motor torque T into a tensile force Ft=T/r, where r is the radius of the servo horn, which in this case is 30mm. This tensile force will produce both a moment and an eccentric axial load at the tip, which, combined with the directional compliance of the beam, will cause the tip to deflect up or down as shown in Figure 4-25A. In Figure 4-25B and C, we show results from testing actuation force vs tip displacement and rotation. While it is possible to achieve nearly 180 degrees of tip rotation, this requires roughly 125N of force, which exceeds the torque capacity of the selected servomotor. The current design requires servos to fit within a voxel, which limits the torque capacity, which scales roughly with servo size. Therefore, our actuated deformation limit was around 35 degrees of rotation.

The servo can contract the string going along one side of the robot (and extend it on the other side). This contraction leads to the change of the angle between the following voxels. If all faces have the same compliance, the contraction of the string will be distributed evenly. Therefore, angles between the following voxels will be the same in one controlled segment. In other words, the curvature of the segment will be constant, which limits the shape that can be reached by the snake. The curvature is bounded by the string's maximal contraction divided by the segment length. The entire robot consists of four beam modules, resulting in a 1.5m long structure as shown in Figure 4-25D. Tabletop demonstration of shape control, with comparison to simulations, is shown in Figure 4-26.

Following tabletop demonstration, the snake robot was prepared for tow tank testing, with the main modification being the addition of a skin and rib system. Testing was performed in the MIT towing tank facility, which features a 33.3 m x 2.67 m x 1.33 m testing tank section and a belt-driven carriage able to achieve steady linear motion at speeds from U = 0.05 m/s to 2.3 m/s. The linear motion stage is instrumented with load cells such that it can [135]. Tests were completed Dixia Fan and Alfonso Rubio Parra.

Test results showed that the robot is generating thrust in excess of hydrodynamic drag and, in a freely swimming environment, has the potential to reach an average swimming velocity at least 0.1m/s. Also, flow visualization was used, and coherent vortical structure is observed with two pairs of vortices inducing a strong cross-flow jet and shedding into the wake in one period of vibration. Currently the robot is undergoing more tests, as it may need a profile with more of an aspect ratio, such as a 3x1 cross section or more, to generate greater net thrust. Regardless, this exercise showed the applicability of a heterogeneous beam, but more importantly, the efficacy of the voxel construction system. Design to assembly to tow tank testing took less than 1 month, which is a marked improvement over slow, expensive, and error-prone soft elastomer casting processes typically used for soft robots.
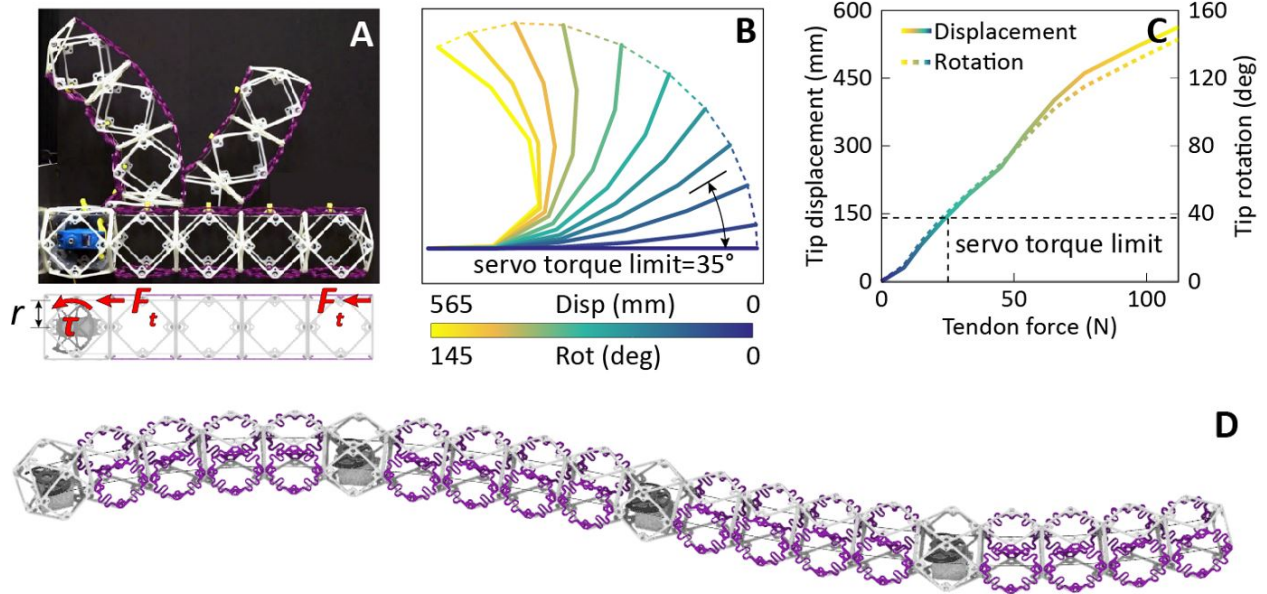
Figure 4-25: Active morphing heterogeneous beam. A) Morphing beam unit, with undeformed and deformed shape, B) Centerline positions from tendon-actuated force-displacement controlled testing, C) Force-displacement controlled testing results, with indication of waterproof servo limits, D) 1.5m discrete cellular soft robot consisting of four morphing beam units connected in series.
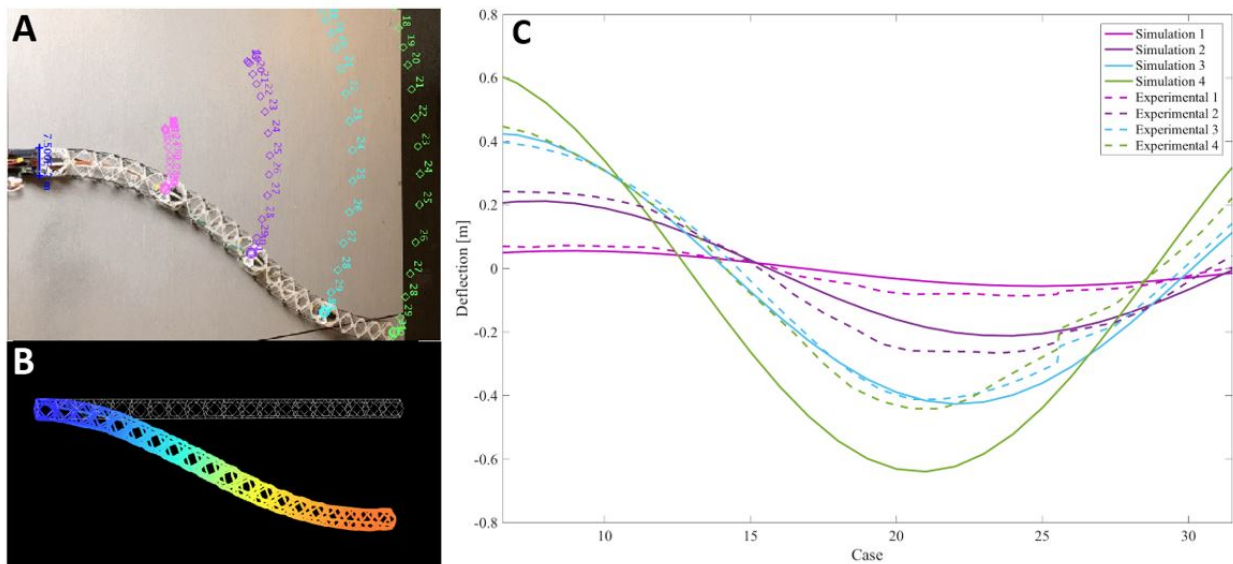
Figure 4-26: Demonstration of hydrosnake motion. A) Tabletop experiment with tracked points, B) Simulation with contours of deflection, C) Comparison between simulation and experimental results (image credit: Megan Ochalek).

4.5 Turbine blades

Background

Wind turbine blades are among the largest single structural elements made— the current largest wind turbine blade is the LM 107m blade on the GE Haliade-X 12MW turbine. Blades longer than 100m have been thoroughly investigated, but not many exist. This is not due to design or manufacturing problems—the issues are mainly logistical. Over around 60m, blade transport becomes problematic, in terms of getting blades from the production facility to the installation site. While solutions exist, they become expensive. On-site blade manufacturing bypasses this, but there is significant capital expenditures required, which is why there are so few examples [136]. Nonetheless, given the potential of increasing rotor diameter, models for 100m blades have been developed which can be used as reference for a lattice blade design [137].

By simply scaling up current blade designs, some important relationships emerge. Energy production scales as rotor diameter D^2, but blade mass and cost scale as D^3. Rotor cost per kilowatt capacity scales roughly linearly, but cost per energy capture scales sub-linearly. In total this means that larger rotors cost more to produce up front but produce more energy at lower cost while in operation [138]. There have been several proposed concepts to achieve extreme-scale wind turbines, such as downwind, pre-aligned blades to prevent tower strikes under large out of plane deflection. Arguably this keeps forces in the axial direction, as opposed to pure root bending, and this approach can also benefit from segmented and morphing blades [139][140]. Given the primarily structural requirements at the root and primarily aerodynamic requirements at the tip, it is conceivable that a lattice blade can accomplish both of these while also enabling tooling-free fabrication on-site, which can enable access to new, remote wind farm areas.
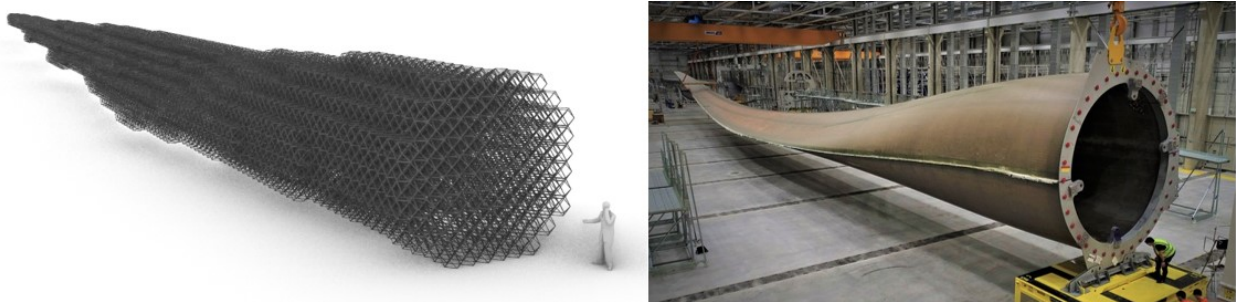
Figure 4-27: XL Turbine blades. (L) Sandia SNL-100 reference geometry filled with notional lattice material, (R) GE Haliade-X 107m blade [170].

Design

As an example of calculating structural efficiency, I use the reported SNL-100 [137] bending stiffness EI ($N*m^2$), linear mass (kg/m), second moment of area I (m^4), and cross sectional area A (m^2), to derive the blade's effective specific stiffness (E_B^*/ρ_B^*). Then, using the

Ashby-Gibson scaling law, we can calculate matching effective specific stiffness for the lattice, $E^*/E = a(\rho^*/\rho)^b$, where a and b are scaling values based on the lattice geometry. Using properties of a 50 percent long carbon fiber reinforced nylon LCF50 (E = 40 GPa, σ= 500 MPa, ρ = 1,370 kg/m^3), we can estimate the resulting mass of a lattice blade with matching stiffness, which we find to be 22 percent less than the baseline model. Cost of material (recurring) and injection mold tooling (non-recurring) can be compared directly as well, where this un-optimized version is more expensive, with anticipated cost optimizations to be determined throughout the project, and shown notionally in Figure 4-28.
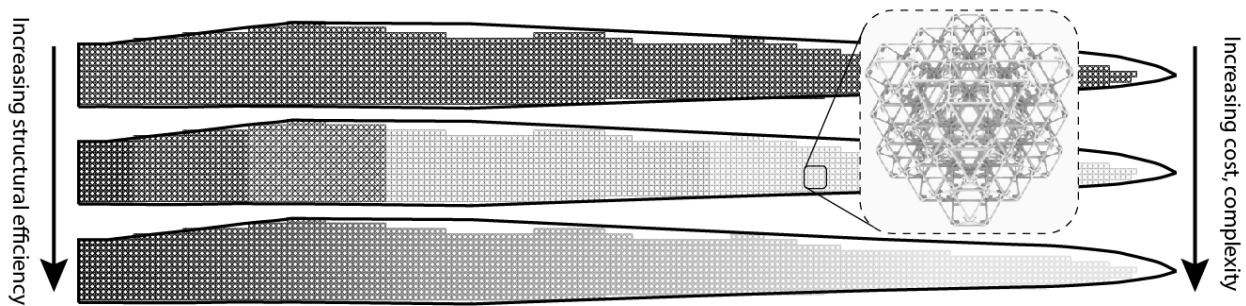
Figure 4-28: Discretely Assembled Turbine Blades. Tradeoffs exist between homogeneous (top), and heterogeneous with discrete (middle) and continuous (bottom) gradients, providing greater structural efficiency with additional cost and complexity.

Performance
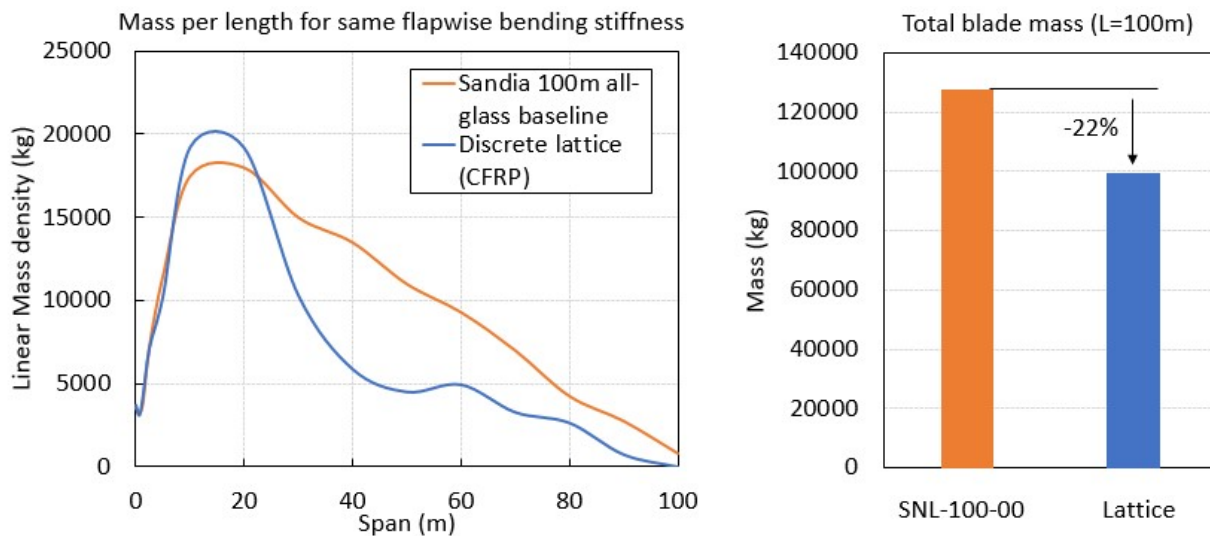
Figure 4-29: Lattice blade study results. (L) Span vs mass per length for glass baseline and lattice blade, (R) overall mass comparison.

4.6 Evaluation

I presented several projects describing their design, simulation, fabrication, and implementation. Given that I've shown these types of structures and systems are possible, and how they might perform, now I'm going to turn to why they might be useful or desirable compared to similar structures made with traditional approaches. Here I will look at three built case studies- bridges, cars, aircraft- and one unbuilt- wind turbine blades.

Bridge

Given the good mechanical properties and scalability, now we must evaluate how this material compares to traditional engineering materials. Ashby proposed a performance index for selecting material to make light, stiff beam. It is shown in [54] that, assuming same cross section, a beam with the highest value for M_b will be most efficient, mass-wise, where $M_b = \sqrt{E}/\rho$. Looking across some common materials, such as woods, metals, and reinforced concrete (a composite by definition), we can plot these beam performance values, and see that the lattice from both GFRP and CFRP outperforms aluminum and steel.
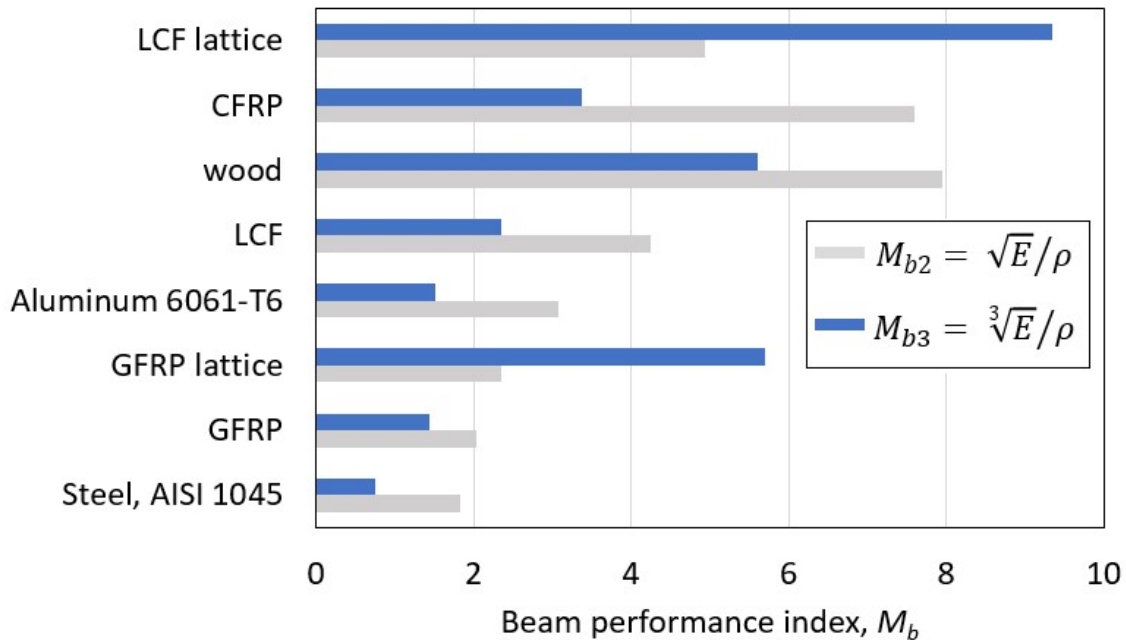
Figure 4-30: Beam performance indices comparing standard engineering materials and discrete lattice materials made of GFRP and CFRP.

Car

Continuing with the study of bending efficiency, in a study on minimization of fuel consumption through optimum material selection of a car frame [141], a car frame is treated as a simply supported beam with a point load in the center, with length L, cross section area A, second area of moment I, density p, modulus of elasticity E, and yield strength σy. For a constant frame stiffness (force/deflection) and dimensions (L, t), it can be shown that the weight of the car frame is dependent on $M_b = \sqrt[3]{E}/\rho$. When plotting these results (Figure 4-30), we see lattice begins to emerge as a very appealing choice.

Light weighting seeks to do more with less. By reducing mass, while still providing sufficient performance, lightweight structures can have life-cycle benefits beyond just the amount of energy and material used to manufacture them. For example, making a car body out of CFRP can reduce body weight by $25 - 40\%$ compared to traditional metal bodies. A car body is roughly 30% the total car weight, resulting in around 10% weight reduction, which results in $6 - 8\%$ less fuel consumed [142]. Less fuel consumed per trip means lower greenhouse gas emissions, and greater cost savings for the end user. Transportation accounts for 28% of US GHG emissions [143], and of this, roughly 60% comes from light-duty vehicles. If fuel consumption, and thus emissions, are reduced by 10% (an aggressive but achievable amount), that equals a 1.7% reduction in total US GHG emissions. While lightweighting alone is not enough to meet emission reduction requirements, this technology will be critical when switching to electric vehicles, whose batteries have limited range that benefits from mass reduction.

Economically, it becomes a bit more complex. The problem is that currently CFRP structures cost 5 times as much as their metal counterparts [144]. So, while the long term savings on fuel and emissions are promising, the upfront cost investment for switching to CFRP is a non-starter. This is typical of almost all industries considering the use of CFRP as a lightweighting technology, especially where economics play a significant factor (ie: not a niche, luxury product or market). Cars, trucks, buses, commercial aircraft, wind turbine blades—in increasingly large applications, the benefits of CFRP are outweighed by the economics, and as a result, the reduction of material and energy usage remains unaddressed.

There are several key drivers when looking at lightweighting across industries in the immediate and long term. The annual forecasted demand for carbon fiber is expected to increase by 50% over the next 5 years [145]. Within automotive, there is a push towards electrification, which will also drive up mass and thus the need for lightweighting to gain efficiency [144]. Further, there is a general agreement that with the advancement of AI over the coming decade or sooner, that OEMs will need to rethink their business model to include Mobility as a Service [146]. This will likely affect the form and function of automobiles, which will be autonomously driven in fleets more, and owned privately by individuals less [147]. Automobiles are projected to become the leading industry for lightweight material usage, making this a key market

From a material perspective, automotive-quality CF is $25/kg, which increases to $100/kg with shaping [145]. If the car frame weighs 15kg, that would be $1,500/frame. Raw material cost for an injection molded CFRP (LCF30) is $22/kg. Injection molding adds value, and

current, sub-optimal molding gives an estimate of $250/kg, which can be reduced to sub-$100/kg targets with favorable cost-scaling of mass production. Let's say then, we want some variations. Tooling and labor from the traditional approach for composite manufacturing make up nearly 50% of the total cost [148]. This could be reduced substantially through automation, which could provide on-demand versatility with no additional cost. Here, cost-savings over traditional approaches could be on the order of $10 - 25\%$. Several studies have shown that the reduction in powertrain and associated mass expenditures can offset potential cost penalties from the use of composites [149].

Aircraft

For aircraft, I showed several projects which addressed morphing for control, ultralight wing construction, and non-standard geometries using tooling free assembly. Here, I will look at what the potential benefits are applied to commercial aircraft.
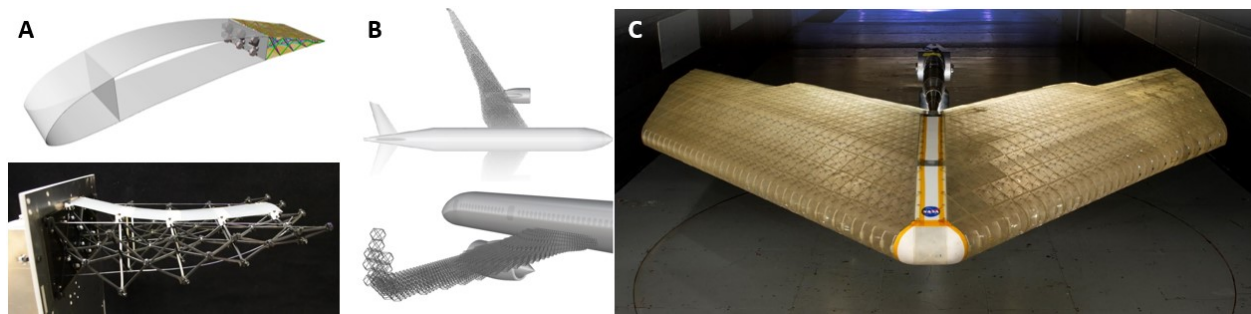
Figure 4-31: Discrete lattice aircraft technology applications. A) Morphing trailing edge, B) Ultralight lattice wing, C) Non-standard BWB outer mold line aircraft [21].

Morphing wing

Studies estimate that the performance benefits of an adaptive trailing edge can offer up to 5.5% fuel savings for a medium sized aircraft [150], noting that while COTS electromechanical actuators can provide sufficient force for morphing, an actuated locking device will prevent overuse [151]. It lists a 3 hour flight range, which equals roughly 1,500 miles or 2,400 km. The entire US air fleet consists of over 7,000 aircraft, the top ten models are made up primarily of 737s and A320s, accounting for at least 90% of this fleet, so we will use this as a baseline. Morphing trailing edges have already been flight tested on small personal aircraft, with promising results [152].

Aircraft lightweighting

A reduction in initial aircraft weight means that the same flight distance can be travelled using less fuel. The primary effect of a weight change is a change in the induced drag and induced power required at any given speed. For a given payload a lighter airframe generates lower drag, owing to a reduced lift requirement, and the attributed drag induced by this lift. This also produces positive feedback: reduction in airframe weight enables the use of smaller, lighter engines, and thus a lighter fuel load. Given this, it is reasonable to look

into using lattice as a stiff and lightweight material to construct parts of aircraft such as the wings and fuselage, which make up nearly 50% of the operating empty weight fraction for a typical commercial aircraft.

A study was undertaken looking at replacing a wing of the Generic Transport Model (GTM) with discrete lattice material [153]. For reference, this is comparable to a A320 or 737 aircraft. The results of the study were as follows: 40% mass reduction (from 13,500 to 8,000 lbs), 200% wing tip displacement increase under typical aero loading (2 to 4in), 23% reduction in first natural frequency (1.375 to 1.05 Hz). Wings make up 23% of typical aircraft weight [154]. If lattice wings have reduced mass ranging from $10-40\%$, that results in a total aircraft mass reduction of 2.3 to 9.2%. For typical operating conditions, a 10% reduction in operational empty mass will lower the fuel burn for any aircraft by about 7% [155]. Therefore, a 9.2% reduction in weight corresponds to a 6.2% reduction in fuel consumption, without taking into account the positive feedback I just described.

Novel geometries

Several studies have looked at the benefits of a BWB-style aircraft, which has significant aerodynamic benefits from increased L/D for a given angle of attack. Liebeck's original study found potential fuel savings of 27.5%. A larger study was performed over a range of aircraft sizes, from regional jets to single and twin aisles (ERJ190, 737, 767, 777, 747). The fuel savings here were estimated to be up to 45%. Airline fuel is roughly $2/gal, and the entire US airline industry consumes about 18 billion gallons of fuel per year, for a total of $36 billion. Therefore, trailing edge modifications can save up to $1.7B, wing lightweighting can save up to $2B, and novel geometries can save from $9.9B to $16B. As nice as those numbers are, it's important to consider the risk/reward factor, as well as the airline industry's reticence to adopt new technologies. Therefore, in the table below, we summarize these findings with opinions about adoption and timeline.

Table 8: Summary of Discrete lattice aircraft application benefits

	Morphing trailing edge	Ultralight lattice wing	Non-standard BWB outer mold line
Potential savings/yr	$1.9B	$2B	$9-16B
% of aircraft structure	5-10% (inboard +outboard)	50%	100%
Estimated time to adoption by industry	3-5 years	5-10 years	15-30 years

Wind

To begin, we can look at the output from the initial study, comparing the SNL-100 and the lattice blade (Table 9). We can see that while there is a mass reduction, it's at double the cost (owing to using CFRP, and the added value of injection molding). What is more challenging to quantify is a) how much this gap can be closed, and b) what other potential cost savings there are from on-site robotic construction of lattice blades. These questions will be left for future research, but in lieu of those answers, we can still look at some potential impacts if this technology were to prove a) successful and b) economic.

For turbine blades I proposed initially matching the bending stiffness of state of the art reference blade designs and showed that there was a potential mass reduction of over 20% using a discretely graded lattice with decreasing density from root to tip. Assuming it's possible to make lattice blades, why should we? To better understand this, we can leverage the abundant models and resources supplied by NREL, Sandia, and other national labs who have been looking at wind energy and turbine performance for existing and proposed designs. There are many useful scaling trends that can be used for studying the effects of scale on turbine design, cost, and implementation (from [138]):

-Energy production $\propto D^{2.22}$
-Blade mass $\propto D^{2.87}$
-Blade cost $\propto D^{3.03}$
-Rotor cost per kW capacity ($/kW) $\propto D^{1.04}$
-Rotor cost per energy capture ($/MWh/yr) $\propto D^{0.82}$

Looking at more fine grained details like cost breakdown for blades, we find that at smaller scales (40m), the blade cost is fairly evenly split between labor (41%) and material (52%). This changes drastically for 100m blades, where material is the majority of the cost (72%) and labor and equipment are each (14%) [156]. Further, large blades are far more affected by gravity loads, whereas smaller blades are governed by aerodynamic loading. All this argues for building blades that are a) lighter, and b) bigger, and hopefully c) cheaper. Looking at the Sandia SNL-100 baseline model is 100m long, it weighs 127k kg, and it costs around $550k to produce, $327k of which is material.

Table 9: Sandia 100m baseline vs. lattice blade preliminary estimates

Design	Total Mass (kg)	Direct cost ($)	Volume throughput (m³/hr)
SNL-100-00	127,510	550,000	27
CFRP Lattice	100,540	1,000,000	7.5

Using this as a baseline for cost and performance, we then wish to incentivize the large scale production of these blades by looking at the enormous potential in contiguous wind farms for cheap, renewable energy. Current fossil fuel energy (coal and gas) accounts for roughly 2/3 the entire US energy supply, while wind and other renewables are around 7%. According to a 2019 study [157], the levelized cost of energy (LCOE) of gas, coal, and wind are 175, 109, and 41 $/MWh. While already a cheaper alternative, increasing the annual

generation by an order of magnitude will require substantial investment in turbines, and as we have seen, the rotor cost per energy capture scales as rotor diameter D0.82, so there is economic incentive to use cheap wind energy provided by large turbines, assuming there is a viable way to produce them at scale, on-demand, and in remote locations where wind energy potential is highest.

Annual domestic energy demand is around 3.9 million GWh/year, but this is easily covered by the total US land wind energy potential of 39 million GWh/year. The Haliade X is currently the world's largest turbine with a diameter of 220m and can generate up to 67 GWh/year. Therefore, we would need roughly 60,000 Haliade X's to cover the demand, resulting in 180,000 of the 100m length blades. Now let's look at how fast and cheap production could be for making these out of lattice.

If we assume a 10cm voxel pitch on a 100m blade that is roughly 1000 m^3 in volume (based on CAD model), that is 1 million voxels per blade. If we set up robots to build in planes parallel to the blade axis, it might look something like Figure 4-32, where the maximum robot density is one per voxel, resulting in 1,000 robots on either side. Let's split that and say 1,000 total for 500 on either side. At roughly $1,000 per robot, that's $1M upfront for robots. How fast can 1,000 robots assemble 1 million voxels? Given half the width is 4m (40 voxels) and height of 5m (50 voxels) we can generalize and say that it will build a row of 40 voxels 50 times. Using our analysis performed earlier, we know that 40 voxels will take $t = n^2 + n$ timesteps, and we find that t = 1,640 timesteps, then x50 = 82,000 timesteps. We assume all of these timesteps happen in parallel, so the entire blade build takes this much time. Based on lab experiments, we can estimate a single time step to take roughly 5 seconds. So we get 114 hours total, or roughly 4.75 days. This puts us in the same order of magnitude for traditional blade manufacturing. Given this promising first pass, more detailed budget and time estimations will be performed for future research.
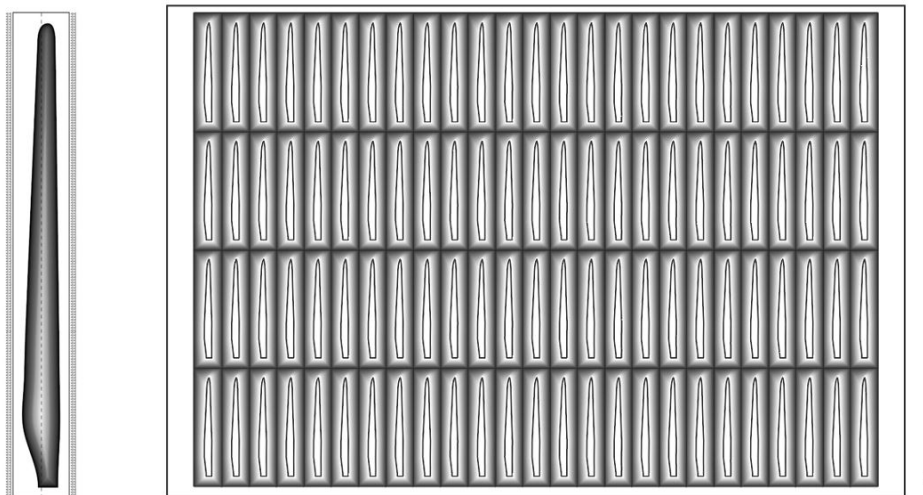
Figure 4-32: Notional lattice blade factory. (L) Blade assembly with robots lined up along length of blade, (R) Boeing Everett production facility repurposed as a blade factory. The building's dimensions are 750x500m, bottom right is a Miata for scale.

Chapter 5

Conclusions

I started this thesis by illustrating about how humans are prolific builders, in spite of the challenges of scaling up. But prolific may not necessarily imply efficient. The Technosphere [158]- comprised of all human-made materials, structures, and systems- is nearly 100 times more massive than all of earth's biomass [159] ($2.7x10^{16}$ kg vs. $5.5x10^{14}$ kg, respectively), and while humans have certainly been prolific, we have also been wasteful. Unsustainable practices of resource consumption, and waste production, imperil the future our species, as well as all of life on earth, owing mainly to the impending consequences of global warming, not to mention pervasive humanitarian issues related to exactly these engineering structures are supposed to solve- infrastructure, transportation, and energy. Clearly, we can do better.

In this thesis, I introduced new materials, methods to automate their assembly, and applications which can offer benefits relevant to these issues of efficiency and sustainability. I argued that by discretizing materials, we can enable the construction of larger, functional structures with properties not achievable using traditional methods. Further, automated assembly methods can be designed in tandem, as a new kind of material-robot system, which avoids issues of cost and complexity increasing proportional to the scale of constructed object. Finally, the structures and systems achievable through discrete assembly offer scalability, versatility, and reliability which I believe will be needed to address global issues facing our species, and planet, in the decades to come.

Aspirationally, this type of material and construction looks to match up with natural systems, with the intention of combining form and function and demonstrating resource efficiency. However, nearly every part I showed was made with some kind of fossil fuel based petrochemical. While upcycled resins make a difference in terms of carbon footprint, my structures would already have an initial offset to make up for owing to their base material. Therefore, coming up with a truly sustainable voxel and lattice construction system is a clear next step. Compostable resins with natural fiber reinforcement are currently being prototypes, and 2D sheets of plywood can be cut into planar face elements, assuming a slightly different corner joint. For further sustainability, resources should be produced locally, then processed into ie: flat sheet stock which can be milled or laser cut for a closed loop ecosystem of voxel construction.

Just as important as the materials is the automation, which arguably should scale with the size of the lattice system. But simply increasing motor size will inevitably run into limits (both practical and theoretical), so a distributed actuation system is likely a more scalable solution. This is comparable to the way muscles work [17], with parallelized, hierarchical arrangement of motor proteins. While a discrete construction scheme can certainly incorporate a distributed actuation layer, the routing, control, and computation is something entirely new, and an exciting direction for future research.

Lastly, what we build in the future plays such an important role in not only resource consumption, but resource allocation and distribution. While this research started in aerospace, it is now branching out into far more broad areas such as infrastructure, transportation, and energy. Assuming a universal construction system, with benefits of digital embedded in the material, the dispersion of an open-source voxel kit is an obvious way to get the technology in more people's hands to put it to use in real-world applications. While commercializing lattice production may also be forthcoming, there's certainly a strong argument for putting discrete mechanical metamaterials out in the world to help fulfill the promise of additive manufacturing by turning things into data and data into things.

Bibliography

[1] R. Hooke, Micrographia: or, some physiological descriptions of minute bodies made by magnifying glasses. 1665.

[2] R. Feynman, "Conclusion: ' Plenty of Room at the Bottom ,'" in Engineering and Science, 1959.

[3] C. E. Shannon, "Communication in the Presence of Noise," Proc. IRE, 1949, doi: 10.1109/JRPROC.1949.232969.

[4] J. T. Schwartz, J. von Neumann, and A. W. Burks, "Theory of Self-Reproducing Automata," Math. Comput., 1967, doi: 10.2307/2005041.

[5] W. Pease, "An Automatic Machine Tool," Sci. Am., 2010

[6] "innofill." http://www.khs.com/en/products/single-machines/filling/glass/beer/with-probe-up-to-75000-bph/innofill-glass-drs-bottle-filler.html.

[7] P. G. Ranky, "Automotive robotics," Industrial Robot. 2004

[8] P. R. Wurman, R. D'Andrea, and M. Mountz, "Coordinating hundreds of cooperative, autonomous vehicles in warehouses," in AI Magazine, 2008.

[9] D. M. Geum, M. S. Park, J. Y. Lim, H. D. Yang, J. D. Song, C. Z. Kim, E. Yoon, S. H. Kim, and W. J. Choi, "Ultra-high-throughput Production of III-V/Si Wafer for Electronic and Photonic Applications," Sci. Rep., 2016

[10] V. Hahn, P. Kiefer, T. Frenzel, J. Qu, E. Blasco, C. Barner-Kowollik, and M. Wegener, "Rapid Assembly of Small Materials Building Blocks (Voxels) into Large Functional 3D Metamaterials," Adv. Funct. Mater., 2020

[11] Nanoscribe GmbH, "Nanoscribe Technology," nanoscribe.de/en/technology/, 2017.

[12] "Masterprint." https://en.machinetools.camozzi.com/products/additive-manufacturing/all-products/masterprint.kl (accessed Jan. 03, 2020).

[13] M. R. Talagani, S. Dormohammadi, R. Dutton, C. Godines, H. Baid, F. Abdi, V. Kunc, B. Compton, S. Simunovic, C. Duty, et al., "Numerical simulation of big area additive manufacturing (3D printing) of a full size car," SAMPE J., 2015.

[14] L. Gardner, P. Kyvelou, G. Herbert, and C. Buchanan, "Testing and initial verification of the world's first metal 3D printed bridge," J. Constr. Steel Res., vol. 172, 2020, [Online].

[15] U. Maine, "3D printed boat." https://umaine.edu/news/blog/2019/10/10/umaine-composites-center-receives-three-guinness-world-records-related-to-largest-3d-printer/ (accessed Jan. 07, 2020).

[16] S. H. Ghaffar, J. Corker, and M. Fan, "Additive manufacturing technology and its implementation in construction as an eco-innovative solution," Automation in Construction. 2018,

[17] R. Milo and R. Phillips, Cell Biology by the Numbers. 2016.

[18] W. Langford, "Discrete Robotic Construction," Massachusetts Institute of Technology, 2019.

[19] T. A. Schaedler and W. B. Carter, "Architected Cellular Materials," Annu. Rev. Mater. Res., vol. 46, no. 1, pp. 187–210, 2016

[20] J. C. Maxwell, " L. On the calculation of the equilibrium and stiffness of frames ," London, Edinburgh, Dublin Philos. Mag. J. Sci., 1864

[21] N. Cramer, D. Cellucci, O. Formoso, C. Gregg, B. Jenett, J. Kim, M. Lendraitis, S. S. Swei, K. Trinh, G. Trinh, et al., "Elastic Shape Morphing of Ultralight Structures by Programmable Assembly," Smart Mater. Struct., 2019

[22] L. J. Gibson, "The hierarchical structure and mechanics of plant materials," Journal of the Royal Society Interface. 2012

[23] R. Lakes, "Foam structures with a negative poisson's ratio," Science (80-.)., 1987

[24] L. J. Gibson, M. F. Ashby, G. S. Schajer, and C. I. Robertson, "The mechanics of two-dimensional cellular materials," Proc. R. Soc. Lond. B., 1982.

[25] L. J. Gibson and M. F. Ashby, "The Mechanics of Three-Dimensional Cellular Materials," Proc. R. Soc. A Math. Phys. Eng. Sci., 2006

[26] M. F. Ashby, "The properties of foams and lattices.," Philos. Trans. A. Math. Phys. Eng. Sci., vol. 364, no. 1838, pp. 15–30, 2006

[27] V. S. Deshpande, M. F. Ashby, and N. a. Fleck, "Foam topology: Bending versus stretching dominated architectures," Acta Mater., vol. 49, no. 6, pp. 1035–1040, 2001

[28] T. A. Schaedler, A. J. Jacobsen, A. Torrents, A. E. Sorensen, J. Lian, J. R. Greer, L. Valdevit, and W. B. Carter, "Ultralight metallic microlattices," Science (80-.)., vol. 334, no. 6058, pp. 962–965, 2011

[29] V. G. Veselago, "THE ELECTRODYNAMICS OF SUBSTANCES WITH SIMULTANEOUSLY NEGATIVE VALUES OF ϵ AND μ, $]Sov.Phys.Uspekhi$, 1968

[30] X. Zhang and Y. Wu, "Effective medium theory for anisotropic metamaterials," Sci. Rep., 2015

[31] V. M. Shalaev, W. Cai, U. K. Chettiar, H.-K. Yuan, A. K. Sarychev, V. P. Drachev, and A. V. Kildishev, "Negative index of refraction in optical metamaterials," Opt. Lett., 2005

[32] C. P. Scarborough, Z. H. Jiang, D. H. Werner, C. Rivero-Baleine, and C. Drake, "Experimental demonstration of an isotropic metamaterial super lens with negative unity permeability at 8.5 MHz," Appl. Phys. Lett., 2012

[33] X. Zheng, H. Lee, T. H. Weisgraber, M. Shusteff, J. DeOtte, E. B. Duoss, J. D. Kuntz, M. M. Biener, Q. Ge, J. a Jackson, et al., "Ultralight, ultrastiff mechanical metamaterials.," Science, vol. 344, no. 6190, pp. 1373–7, 2014

[34] X. Zheng, W. Smith, J. Jackson, B. Moran, H. Cui, D. Chen, J. Ye, N. Fang, N. Rodriguez, T. Weisgraber, et al., "Multiscale metallic metamaterials," Nat. Mater., 2016

[35] L. R. Meza, S. Das, and J. R. Greer, "Strong , Lightweight and Recoverable Three - Dimensional Ceramic Nanolattices," Submitted, vol. 345, no. 6202, pp. 1322–1326, 2014

[36] J. B. Berger, H. N. G. Wadley, and R. M. McMeeking, "Mechanical metamaterials at the theoretical limit of isotropic elastic stiffness," Nature, vol. 543, no. 7646, pp. 533–537, 2017

[37] L. A. Shaw, F. Sun, C. M. Portela, R. I. Barranco, J. R. Greer, and J. B. Hopkins,

"Computationally efficient design of directionally compliant metamaterials," Nat. Commun., 2019

[38] Y. Jiang and Q. Wang, "Highly-stretchable 3D-architected Mechanical Metamaterials," Sci. Rep., 2016

[39] X. Ren, R. Das, P. Tran, T. D. Ngo, and Y. M. Xie, "Auxetic metamaterials and structures: A review," Smart Materials and Structures. 2018

[40] F. Wang, "Systematic design of 3D auxetic lattice materials with programmable Poisson's ratio for finite strains," J. Mech. Phys. Solids, 2018

[41] T. Frenzel, M. Kadic, and M. Wegener, "Three-dimensional mechanical metamaterials with a twist," Science (80-.)., 2017

[42] B. Zhu, M. Skouras, D. Chen, and W. Matusik, "Two-scale topology optimization with microstructures," ACM Trans. Graph., 2017 . [43] D. Chen, M. Skouras, B. Zhu, and W. Matusik, "Computational discovery of extremal microstructure families," Sci. Adv., 2018

[44] C. Coulais, E. Teomy, K. De Reus, Y. Shokef, and M. Van Hecke, "Combinatorial design of textured mechanical metamaterials," Nature, 2016

[45] X. Yu, J. Zhou, H. Liang, Z. Jiang, and L. Wu, "Mechanical metamaterials associated with stiffness, rigidity and compressibility: A brief review," Progress in Materials Science, vol. 94. pp. 114–173, 2018

[46] R. a Shelby, D. R. Smith, and S. Schultz, "Experimental verification of a negative index of refraction.," Science, 2001

[47] Tie Jun Cui, Metamaterials: Theory, Design, and Applications. 2010.

[48] G. A. Popescu, T. Mahale, and Gershenfeld Neil A, "Digital materials for digital printing," in International Conference on Digital Fabrication Technologies, 2006.

[49] J. Hiller and H. Lipson, "Design and analysis of digital materials for physical 3D voxel printing," Rapid Prototyp. J., 2009

[50] W. Langford, A. Ghassaei, and N. Gershenfeld, "Automated Assembly of Electronic Digital Materials," in ASME MSEC, 2016.

[51] W. Langford and N. Gershenfeld, "A Discretely Assembled Walking Motor," in International Conference on Manipulation, Automation and Robotics at Small Scales, 2019.

[52] K. C. Cheung and N. Gershenfeld, "Reversibly assembled cellular composite materials.," Science, vol. 341, no. 6151, pp. 1219–21, 2013

[53] C. Gregg, J. Kim, and K. Cheung, "Ultra-Light and Scalable Composite Lattice Materials," Adv. Eng. Mater., 2018

[54] M. Ashby, Materials selection in mechanical design: Fourth edition. 2010.

[55] W. Chen, S. Watts, J. A. Jackson, W. L. Smith, D. A. Tortorelli, and C. M. Spadaccini, "Stiff isotropic lattices beyond the Maxwell criterion," Sci. Adv., 2019

[56] W. C. Young and R. G. Budynas, "Roark's Formulas for Stress and Strain," Library (Lond)., vol. 7, no. 7th Edition, p. 832, 2002

[57] B. Jenett, N. Gershenfeld, and P. Guerrier, "Building Block-Based Assembly of Scalable Metallic Lattices," in ASME MSEC, 2018

[58] O. Formoso, C. Gregg, G. Trinh, A. Rogg, and K. Cheung, "Androgynous Fasteners for Robotic Structural Assembly," in IEEE Aerospace Conference Proceedings, 2020.

[59] L. Dong and H. Wadley, "Mechanical properties of carbon fiber composite octet-truss lattice structures," Compos. Sci. Technol., 2015

[60] N. Wang, Z. Zhang, and X. Zhang, "Stiffness analysis of corrugated flexure beam using stiffness matrix method," Proc. Inst. Mech. Eng. Part C J. Mech. Eng. Sci., 2019

[61] A. Clausen, F. Wang, J. S. Jensen, O. Sigmund, and J. A. Lewis, "Topology Optimized Architectures with Programmable Poisson's Ratio over Large Deformations," Adv. Mater., vol. 27, no. 37, pp. 5523–5527, 2015

[62] T. Li, X. Hu, Y. Chen, and L. Wang, "Harnessing out-of-plane deformation to design 3D architected lattice metamaterials with tunable Poisson's ratio," Sci. Rep., 2017

[63] C. Wales, R. Cheung, and J. E. Cooper, "Chiral morphing wing tip design and test," in 23nd AIAA/AHS Adaptive Structures Conference, 2015

[64] V. Goga, "New phenomenological model for solid foams," in Computational Methods in Applied Sciences, 2011

[65] L. L. Howell, S. P. Magleby, and B. M. Olsen, Handbook of Compliant Mechanisms. 2013.

[66] P. Ziemke, T. Frenzel, M. Wegener, and P. Gumbsch, "Tailoring the characteristic length scale of 3D chiral mechanical metamaterials," Extrem. Mech. Lett., 2019

[67] W. Chen and X. Huang, "Topological design of 3D chiral metamaterials based on couple-stress homogenization," J. Mech. Phys. Solids, 2019

[68] S. Hengsbach and A. D. Lantada, "Direct laser writing of auxetic structures: Present capabilities and challenges," Smart Mater. Struct.

[69] "Micropep." http://micropep.com/ (accessed Jan. 07, 2020). [70] G. W. Milton and A. V. Cherkaev, "Which elasticity tensors are realizable?," J. Eng. Mater. Technol. Trans. ASME, 1995

[71] "SLM." https://www.slm-solutions.com/ (accessed Jan. 07, 2020).

[72] J. Go, S. N. Schiffres, A. G. Stevens, and A. J. Hart, "Rate limits of additive manufacturing by fused filament fabrication and guidelines for high-throughput system design," Addit. Manuf., 2017

[73] L. L. N. Laboratories, "Large-Area Projection MicroStereolithography." https://ipo.llnl.gov/content/assets/docs/award-archive/lapusl.pdf

[74] A. R. Torrado and D. A. Roberson, "Failure Analysis and Anisotropy Evaluation of 3D-Printed Tensile Test Specimens of Different Geometries and Print Raster Patterns," J. Fail. Anal. Prev., 2016

[75] S. I. Park, D. W. Rosen, S. kyum Choi, and C. E. Duty, "Effective mechanical properties of lattice material fabricated by material extrusion additive manufacturing," Addit. Manuf., 2014

[76] D. Lévesque, C. Bescond, M. Lord, X. Cao, P. Wanjara, and J. P. Monchalin, "Inspection of additive manufactured parts using laser ultrasonics," in AIP Conference Proceedings, 2016,

[77] L. Bochmann, C. Bayley, M. Helu, R. Transchel, K. Wegener, and D. Dornfeld, "Understanding error generation in fused deposition modeling," Surf. Topogr. Metrol. Prop., 2015

[78] L. Liu, P. Kamm, F. García-Moreno, J. Banhart, and D. Pasini, "Elastic and failure response of imperfect three-dimensional metallic lattices: the role of geometric defects induced by Selective Laser Melting," J. Mech. Phys. Solids, 2017

[79] X. Zhang and et al, "Large-scale 3D printing by a team of mobile robots," Autom. Constr., 2018.

[80] S. J. Keating, J. C. Leland, L. Cai, and N. Oxman, "Toward site-specific and self-sufficient robotic fabrication on architectural scales," Sci. Robot., 2017

[81] X. Zheng and et al, "Multiscale metallic metamaterials," Nat. Mater., 2016.

[82] L. C. Montemayor, L. R. Meza, and J. R. Greer, "Design and fabrication of hollow rigid nanolattices via two-photon lithography," Adv. Eng. Mater., 2014

[83] C. E. Duty, V. Kunc, B. Compton, B. Post, D. Erdman, R. Smith, R. Lind, P. Lloyd, and L. Love, "Structure and mechanical behavior of Big Area Additive Manufacturing (BAAM) materials," Rapid Prototyp. J., vol. 23, no. 1, pp. 181–189, 2017

[84] S. J. Keating, J. C. Leland, L. Cai, and N. Oxman, "Toward site-specific and self-sufficient robotic fabrication on architectural scales," Sci. Robot., vol. 2, no. 5, 2017

[85] J. Werfel, K. Petersen, and R. Nagpal, "Designing collective behavior in a termite-inspired robot construction team," Science (80-.)., 2014

[86] Y. Terada and S. Murata, "Automatic Modular Assembly System and its Distributed Control," Int. J. Rob. Res., vol. 27, no. 3–4, pp. 445–462, 2008

[87] F. Augugliaro, S. Lupashin, M. Hamer, C. Male, M. Hehn, M. W. Mueller, J. S. Willmann, F. Gramazio, M. Kohler, and R. D'Andrea, "The flight assembled architecture installation: Cooperative contruction with flying machines," IEEE Control Syst., vol. 34, no. 4, pp. 46–64, 2014

[88] K. Dörfler, T. Sandy, M. Giftthaler, F. Gramazio, M. Kohler, and J. Buchli, "Mobile Robotic Brickwork: Automation of a Discrete Robotic Fabrication Process Using an Autonomous Mobile Robot," in Robotic Fabrication in Architecture, Art and Design 2016, 2016

[89] Q. Lindsey, D. Mellinger, and V. Kumar, "Construction with quadrotor teams," Auton. Robots, 2012

[90] S. Karumanchi, "Payload-centric autonomy for in-space robotic assembly of modular space structures," J. Feild Robot., 2018.

[91] J. D. Hiller and H. Lipson, "Fully Recyclable Multi-Material Printing," Solid Free. Fabr. Symp., 2009.

[92] M. S. Lake, W. L. Heard, J. J. Watson, and T. J. Collins, "Evaluation of Hardware and Procedures for Astronaut Assembly and Repair of Large Precision Reflectors," Langley Research Center, NASA /TP-2000-210317, 2000.

[93] M. D. Rhodes, R. W. Will, and C. Quach, "Baseline Tests of an Autonomous Telerobotic System for Assembly of Space Truss Structures," Langley, 1994.

[94] G. Trinh, G. Copplestone, M. O'Connor, S. Hu, S. Nowak, K. Cheung, B. Jenett, and D. Cellucci, "Robotically assembled aerospace structures: Digital material assembly using a gantry-type assembler," in IEEE Aerospace Conference Proceedings, 2017

[95] F. Nigl, S. Li, J. E. Blum, and H. Lipson, "Structure-reconfiguring robots: Au-

tonomous truss reconfiguration and manipulation," IEEE Robot. Autom. Mag., vol. 20, no. 3, pp. 60–71, 2013

[96] Y. Yoon and D. Rus, "Shady3D: A Robot that Climbs 3D Trusses," in IEEE International Conference on Robotics and Automation, 2007.

[97] V. Helm, S. Ercan, F. Gramazio, and M. Kohler, "Mobile robotic fabrication on construction sites: DimRob," in IEEE International Conference on Intelligent Robots and Systems, 2012, pp. 4335–4341

[98] J. Werfel, K. Petersen, and R. Nagpal, "Designing Collective Behavior in a Termite-Inspired Robot Construction Team," Science (80-.)., vol. 343, no. 6172, pp. 754–758, 2014

[99] B. Jenett and D. Cellucci, "A mobile robot for locomotion through a 3D periodic lattice environment," in Proceedings - IEEE International Conference on Robotics and Automation, 2017

[100] B. Jenett and K. Cheung, "BILL-E: Robotic platform for locomotion and manipulation of lightweight space structures," in 25th AIAA/AHS Adaptive Structures Conference, 2017, 2017.

[101] K. D. Kotay and D. Rus, "The Inchworm Robot: A Multi-Functional System," in Autonomous Robots 8, Kluwer Academic Publishers, 2000, pp. 53–69.

[102] S. M. Felton, M. T. Tolley, C. D. Onal, D. Rus, and R. J. Wood, "Robot self-assembly by folding: A printed inchworm robot," in Proceedings - IEEE International Conference on Robotics and Automation, 2013, pp. 277–282

[103] M. Minor, H. Dulimarta, G. Danghi, R. Mukherjee, R. L. Tummala, and D. Aslam, "Design, implementation, and evaluation of an under-actuated miniature biped climbing robot," IEEE Int. Conf. Intell. Robot. Syst., vol. 3, pp. 1999–2005, 2000

[104] M. Ochalek, G. Trinh, O. Formoso, B. Jenett, C. Gregg, and K. Cheung, "Geometry and Joint Systems for Lattice-Based Reconfigurable Space Structures," in IEEE Aerospace Conference Proceedings, 2019.

[105] B. Jenett, A. Abdel-Rahman, K. C. Cheung, and N. Gershenfeld, "Material-Robot System for Assembly of Discrete Cellular Structures," IEEE Robot. Autom. Lett., 2019,

[106] Y. Terada and S. Murata, "Modular Structure Assembly Using Blackboard Path Planning System," in International Symposium on Automation and Robotics in Construction., 2006.

[107] Y. Deng, Y. Hua, N. Napp, and K. Petersen, "A Compiler for Scalable Construction by the TERMES Robot Collective," Rob. Auton. Syst.

[108] A. Abdel-Rahman, A. T. Becker, D. E. Biediger, K. C. Cheung, S. P. Fekete, N. A. Gershenfeld, S. Hugo, B. Jenett, P. Keldenich, E. Niehs, et al., "Space ants: Constructing and reconfiguring large-scale structures with finite automata," in Leibniz International Proceedings in Informatics, LIPIcs, 2020

[109] M. Rubenstein, C. Ahler, and R. Nagpal, "Kilobot: A low cost scalable robot system for collective behaviors," in Proceedings - IEEE International Conference on Robotics and Automation, 2012

[110] "Infrastructure Report Card." https://www.infrastructurereportcard.org/.

[111] H. J. Dagher, D. J. Bannon, W. G. Davids, R. A. Lopez-Anido, E. Nagy, and K. Goslin, "Bending behavior of concrete-filled tubular FRP arches for bridge structures," Constr. Build. Mater., 2012

[112] B. R. Russell and A. P. Thrall, "Portable and rapidly deployable bridges: Historical perspective and recent technology developments," J. Bridg. Eng., 2013

[113] W. Xu, Y. Gao, C. Sun, and Z. Wang, "FABRICATION AND APPLICATION OF 3D-PRINTED CONCRETE STRUCTURAL COMPONENTS IN THE BAOSHAN PEDESTRIAN BRIDGE PROJECT," in Fabricate 2020, 2020.

[114] B. Jenett, D. Cellucci, C. Gregg, and K. C. Cheung, "Meso-scale digital materials: modular, reconfigurable, lattice-based structures," in Proceedings of the 2016 Manufacturing Science and Engineering Conference, 2016.

[115] C. Gregg, K. Cheung, and B. Jenett, "Assembled Composite Lattice Structures: Towards Ideal Performance in Large-Scale Applications," in IUTAM Symposium on Architectured Material Mechanics, 2018.

[116] L. Gagnon, M. Richard, G. Beardsell, and M. Boudreau, "The Process of Making an Aerodynamically Efficient Car Body for the SAE Supermileage Competition," in SAE Technical Paper Series, 2012

[117] N. Uddin, Blast protection of civil infrastructures and vehicles using composites. 2010.

[118] "Cal Poly Supermileage." http://cpsmv.blogspot.com/2006/06/ (accessed Jan. 07, 2020).

[119] J. Mueller, K. H. Matlack, K. Shea, and C. Daraio, "Energy Absorption Properties of Periodic and Stochastic 3D Lattice Materials," Adv. Theory Simulations, 2019

[120] T. Tancogne-Dejean, A. B. Spierings, and D. Mohr, "Additively-manufactured metallic micro-lattice materials for high specific energy absorption under static and dynamic loading," Acta Mater., 2016

[121] R. H. Liebeck, "Design of the Blended Wing Body Subsonic Transport," J. Aircr., 2008

[122] S. Barbarino, O. Bilgen, R. M. Ajaj, M. I. Friswell, and D. J. Inman, "A Review of Morphing Aircraft," J. Intell. Mater. Syst. Struct., vol. 22, no. 9, pp. 823–877, 2011

[123] S. Kota, R. Osborn, G. Ervin, D. Maric, P. Flick, and D. Paul, "Mission Adaptive Compliant Wing – Design , Fabrication and Flight Test Mission Adaptive Compliant Wing –," Test, 2006.

[124] J. Markish and K. Willcox, "Multidisciplinary Techniques for Commercial Aircraft System Design," in 9th AIAA/ISSMO Symposium on Multidisciplinary Analysis and Optimization, 4-6 September 2002, Atlanta, Georgia, 2002, no. September, pp. 1–9.

[125] B. Jenett, S. Calisch, D. Cellucci, N. Cramer, N. Gershenfeld, S. Swei, and K. C. Cheung, "Digital Morphing Wing: Active Wing Shaping Concept Using Composite Lattice-Based Cellular Structures," Soft Robot., vol. 4, no. 1, 2017

[126] K. Cheung, D. Cellucci, G. Copplestone, N. Cramer, J. Fusco, B. Jenett, J. Kim, A. Langford, A. Mazhari, G. Trinh, et al., "Development of mission adaptive digital composite aerostructure technologies (MADCAT)," in 17th AIAA Aviation Technology, Integration,

and Operations Conference, 2017, 2017.

[127] R. Pecora, F. Amoroso, M. Arena, M. C. Noviello, and F. Rea, "Experimental validation of a true-scale morphing flap for large civil aircraft applications," in Industrial and Commercial Applications of Smart Structures Technologies 2017

[128] V. A. Tucker, "The energetic cost of moving about," Am. Sci., 1975.

[129] G. Bledt, M. J. Powell, B. Katz, J. Di Carlo, P. M. Wensing, and S. Kim, "MIT Cheetah 3: Design and Control of a Robust, Dynamic Quadruped Robot," in IEEE International Conference on Intelligent Robots and Systems

[130] M. S. Triantafyllou and G. S. Triantafyllou, "An efficient swimming machine," Sci. Am., 1995

[131] G. D. Bousquet, M. S. Triantafyllou, and J. J. E. Slotine, "Optimal dynamic soaring consists of successive shallow arcs," J. R. Soc. Interface, 2017

[132] A. D. Marchese, C. D. Onal, and D. Rus, "Autonomous Soft Robotic Fish Capable of Escape Maneuvers Using Fluidic Elastomer Actuators," Soft Robot., vol. 1, no. 1, pp. 75–87, 2014

[133] M. Ebrahimi and M. Abbaspoor, "Imitation of the body/caudal fin undulatory swimming of a spiny dogfish (Squalus acanthias): The kinematic equation," Proc. Inst. Mech. Eng. Part M J. Eng. Marit. Environ., 2014

[134] K. N. Lucas, G. V. Lauder, and E. D. Tytell, "Airfoil-like mechanics generate thrust on the anterior body of swimming fishes," Proc. Natl. Acad. Sci. U. S. A., 2020

[135] D. Fan, G. Jodin, T. R. Consi, L. Bonfiglio, Y. Ma, L. R. Keyes, G. E. Karniadakis, and M. S. Triantafyllou, "A robotic intelligent towing tank for learning complex fluid-structure dynamics," Sci. Robot., 2019

[136] D. a Griffin, "Blade System Design Studies Volume I: Composite Technologies for Large Wind Turbine Blades," Energy, 2002.

[137] D. T. Griffith and T. D. Ashwill, "The Sandia 100-meter All-glass Baseline Wind Turbine Blade: SNL100-00," Baseline, 2011

[138] D. a Griffin, "WindPACT Turbine Design Scaling Studies Technical Area 1 - Composite Blades for 80-to 120-Meter Rotor.," Natl. Renew. Energy Lab. NREL/SR-500 . . . , 2001

[139] E. Loth, A. Steele, B. Ichter, M. Selig, and P. Moriarty, "Segmented ultralight pre-aligned rotor for extreme-scale wind turbines," in 50th AIAA Aerospace Sciences Meeting Including the New Horizons Forum and Aerospace Exposition, 2012.

[140] C. (Chris) Qin, E. Loth, D. S. Zalkind, L. Y. Pao, S. Yao, D. T. Griffith, M. S. Selig, and R. Damiani, "Downwind coning concept rotor for a 25 MW offshore wind turbine," Renew. Energy, 2020

[141] R. Eleni and A. Panagiotis, "Minimization of fuel consumption through optimum material selection of a car frame production company," WIT Trans. Ecol. Environ., 2006

[142] F. Stodolsky, A. Vyas, and R. Cuenca, "Lightweight materials in the light-duty passenger vehicle market: Their market penetration potential and impacts," in 2nd World Car Conference, 1995.

[143] "EPA." https://www.epa.gov/ghgemissions/sources-greenhouse-gas-emissions, (ac-

cessed May 01, 2018).

[144] R. Heuss, N. Müller, W. van Sintern, A. Starke, A. Tschiesner, W. Van Sintern, A. Starke, A. Tschiesner, W. van Sintern, A. Starke, et al., "Lightweight, heavy impact," McKinsey co, 2012,

[145] S. Das, J. Warren, D. West, and S. M. Schexnayder, "Global Carbon Fiber Composites Supply Chain Competitiveness Analysis," Oak Ridge Natl. Lab., 2016.

[146] J. Arbib and T. Seba, "Rethinking Transportation 2020-2030," RethinkX, 2017

[147] W. Goodall, J. Bornstein, T. D. Fishman, and B. Bonthron, "The rise of mobility as a service," Deloitte Rev., 2017.

[148] E. Shehab, W. Ma, and A. Wasim, "Manufacturing cost modelling for aerospace composite applications," in Advanced Concurrent Engineering, 2013

[149] A. B. Lovins, "Reframing Automotive Fuel Efficiency," SAE Int. J. Sustain. Transp. Energy, Environ. Policy, 2020

[150] G. Diodati, A. Concilio, S. Ricci, A. De Gaspari, F. Huvelin, A. Dumont, and J.-L. Godard, "Estimated performance of an adaptive trailing-edge device aimed at reducing fuel consumption on a medium-size aircraft," in Industrial and Commercial Applications of Smart Structures Technologies 2013, 2013

[151] G. Diodati and A. Concilio, "Actuation needs for an adaptive trailing edge device aimed at reducing fuel consumption on a regional aircraft," in Industrial and Commercial Applications of Smart Structures Technologies 2013, 2013

[152] S. Kota, P. Flick, and F. Collier, "Flight testing of the FlexFloilTM adaptive compliant trailing edge," in 54th AIAA Aerospace Sciences Meeting, 2016.

[153] N. Cramer, J. Kim, B. Jenett, K. C. Cheung, and S. Swei, "Simulated Scalability of Discrete Lattice Materials Substructures to Commercial Scale Aircraft," in AIAA Aviation Forum, 2020.

[154] J. Markish, "Valuation Techniques for Commercial Aircraft Program Design," Massachusetts Institute of Technology, 2002.

[155] D. I. A. Poll, "On the application of light weight materials to improve aircraft fuel burn - Reduce weight or improve aerodynamic efficiency?," Aeronaut. J., 2014

[156] P. Bortolotti, D. Berry, R. Murray, E. Gaertner, J. Dale, R. Damiani, G. Barter, and K. Dykes, "A detailed wind turbine blade cost model," Nrel, 2019.

[157] "Lazard." https://www.lazard.com/perspective/lcoe2019/ (accessed Jan. 07, 2020).

[158] J. Zalasiewicz, M. Williams, C. N. Waters, A. D. Barnosky, J. Palmesino, A.-S. Rönnskog, M. Edgeworth, C. Neal, A. Cearreta, E. C. Ellis, et al., "Scale and diversity of the physical technosphere: A geological perspective," Anthr. Rev., 2017

[159] Y. M. Bar-On, R. Phillips, and R. Milo, "The biomass distribution on Earth," Proc. Natl. Acad. Sci., 2018

[160] "The Lego Club Plus" online: http://www.thelegoclub.com/the-lego-club-plus/, accessed 07/01/20

[161] J. B. Pendry, Negative refraction makes a perfect lens. Phys. Rev. Lett. (2000)

[162] D. R. Smith, N. Kroll, Negative refractive index in left-handed materials. Phys. Rev. Lett. (2000)

[163] R. A. Shelby, D. R. Smith, S. Schultz, Experimental verification of a negative index of refraction. Science (80-.). (2001)

[164] Enrique Perrella, "This is the @BoeingAirplanes Everett Factory's layout, where the Boeing 767, 777, 747 and 787 programs are brought to life!", December 2, 20116, 10:10am https://twitter.com/Enrique77W/ status/804749719289270273/photo/1, accessed 07/01/20

[165] Gabe Perez, "Kiva Systems Automation", November 21, 2013, https:// youtu.be /1Cv7qaz63nQ, accessed 07/01/20

[166] Wright brothers, web page. http://www.wright-brothers.org, accessed 07/01/20

[167] D. Vechtel, B. Hauber, G. Looye, Analysis of a multi-functional high-lift system driven by an active differential gear box. CEAS Aeronaut. J. (2014)

[168] S. Celo, J. Nebus, I. K. Wang, The Role of Internal and External Complexity in Global Factory Performance: An NKC Application. J. Int. Manag. (2018),

[169] "Boeing's Dreamliner - Waking from the Nightmare"? July 22,2009. Webpage: https://www.airport-technology.com/features/feature59453/, accessed 07/01/20

[170] "GE Unveils world's largest wind turbine blade", April 23, 2019. Webpage: https: //www. businessgreen.com/ news/3074442/ge-unveils- worlds-largest-wind-turbine-blade, accessed 07/01/20